SCUOLA DI DOTTORATO
UNIVERSITÀ DEGLI STUDI DI MILANO-BICOCCA

Department of

Biotechnology and Bioscience

PhD program in Material Science and Nanotechnology Cycle XXXº

Dynamics of Nanoparticle-Protein Corona: Formation, Evolution and insight on Protein Structure

Vitali Michele

Registration number 758278

Tutor: Prof. Rita Grandori

Co-tutor: Prof. Victor Puntes

Coordinator: Prof. Marco Bernasconi

ACADEMIC YEAR 2016/2017

Abstract

In complex physiological media proteins form transient complexes with nanoparticles (NPs), mediated by competitive binding between proteins and NP surfaces, leading to the formation of a stable (hard) protein corona (HPC). Understanding the formation and the dynamics of this interaction is crucial for designing NP-based therapies, since HPC determines the biological identity of the NPs in vivo. The strong affinity between NPs surfaces and proteins can compensate the destabilization forces that colloidal NPs experience in high ionic strength media, stabilizing them. This interaction is immediate (soft -non stable –PC) and evolves with time (HPC).

Nowadays, different studies regarding HPC composition show contradictory results. The complexity of serum composition, being NP size in the same range of proteins, and lack of reliable methods to determine composition of HPC, are behind these controversies. Several underestimated parameters regarding the response of NPs in physiological media (aggregation, dissolution) are critical determinants to be carefully addressed to better understand the formation of the HPC. In this context, it is necessary to develop simple but efficient and reliable protocols to study these processes.

In this work, consequences of NP-PC formation providing a simple and reliable approach for determining both composition and physicochemical characterization of the HPC, and the implication for protein structures, is shown.

In the first part, the hardening of the PC on 20 nm AuNPs, as a model case of metallic NP widely used in medicine, was monitored over time by UV-Vis spectroscopy, Dynamic Light Scattering and Z-Potential. Results of the process of HPC formation with only albumin or IgG were compared to results of HPC formation in serum. Time evolution of the

NP-PC when conjugated with one protein can be understood as a fingerprint of the adsorption of that specific protein. Thus, the study of the PC evolution in serum provided information about the final composition of the HPC. Results showed similar pattern as when incubated when only albumin. Proteomic analysis confirmed the results. In addition, experiments mimicking the natural metabolic degradations of bioconjugates using etching agents (NaCN and HNO3), indicated that HPC exert protective effect on the NP core. Finally, limited proteolysis experiments indicated an altered metabolization of the protein inside the HPC, which can be related to a protein altered conformation in this adsorbed state.

In the second part, HPC was studied on 50 nm SiO_2 NPs, as a model case of metal oxide NP widely used in nanomedicine, by using either globular and intrinsically disordered proteins (IDPs), with the aim to investigate conformational changes induced by the interaction with NPs. IDPs exist in solution as conformational ensembles, whose features in the presence of NPs are still unknown. Thre IDPs, a-casein, Sic1 and a-synuclein, were analyzed compared to lysozyme and transferrin (globular proteins model), describing conformational properties inside the HPC by circular dichroism and Fourier-transform infrared spectroscopy. Results indicated that IDPs maintain structural disorder inside HPC, experiencing minor, protein-specific, induced folding and stabilization against further conformational transitions. Oppositely, the analyzed globular proteins displayed the tendency to lose their ordered structure. Finally, the Transferrin-Tb complex, was also used in the HPC formation. The detection of the fluorescent properties of Tb upon HPC preparation is reported. By electrophoresis it was observed all the proteins forming the HPC and electron microscopy showed an HPC of a single layer of protein molecules. This latter part of work opens broad perspectives on the use of NP as agents that mimic macromolecular partners, allowing the comprehension of the effect of different factors affecting the interaction by rational design of NP surfaces.

Contents

List of Figures **vii**

List of Tables **xix**

List of Abbreviations **xxi**

1 General introduction **1**

1.1 Nanoparticles 1

1.2 Interaction between inorganic NPs and biological system 3

1.3 Methods for protein corona investigation 7

2 Time evolution of the protein corona **13**

2.1 Introduction 13

2.1.1 Goals and strategy 17

2.1.2 Scientific relevance of the selected materials . . . 21

Gold nanoparticles 21

Proteins 23

2.2 Materials and methods 25

2.2.1 Synthesis of gold NPs 25

2.2.2 Proteins 29

2.2.3 Bioconjugation protocol 29

2.2.4 Characterization techniques 33

2.2.5 Digestion of protein constituting the hard corona 38

2.3 Results and discussion 41

2.3.1 Hardening of the nanoparticle protein corona . . 41

Hardening of the HS protein corona 42
Hardening of the HSA protein corona 46
Hardening of the IgG protein corona 50
Discussion 52
2.3.2 Altered digestion of proteins constituting the hard protein corona 59
2.3.3 Parameters affecting the hard corona formation . 67
NP-IgG conjugation in 100% DMEM physiological media 78

3 Conformational properties of the hard corona 83
3.1 Introduction 83
3.1.1 Goals and strategy 86
3.1.2 Scientific relevance of the selected materials . . . 88
Silica NPs 88
Intrinsically disordered proteins 88
Globular proteins 92
3.2 Materials and methods 97
3.2.1 Synthesis of silica NPs 97
3.2.2 Proteins 99
3.2.3 Hard corona preparation 103
3.2.4 Characterization techniques 104
3.3 Results and discussion 109
3.3.1 Hard Corona preparation 109
3.3.2 Secondary structure by CD 121
3.3.3 Secondary structure by FTIR Spectroscopy 124
3.3.4 Effect of NPs on α-synuclein aggregation 129
3.3.5 Spectroscopic properties of transferrin hard corona 131

4 General Conclusion 135

A Raw data from far-UV CD 139

B List of publications **141**

Bibliography **143**

List of Figures

1.1 Factors that regulate the formation of the protein corona [27]). 5
1.2 CD signal of lysozyme and silica NP. 10

2.1 *Dynamic in-solution equilibrium between hard and soft corona [80].* Fast exchanging proteins with low affinity are characterized by high $k_{adsorption}$ and $k_{desorption}$). 15
2.2 *Hardening of the NP-protein corona.* As exposition time increase, proteins tightly adsorb to NP surface, gradually forming the hard protein corona, represented by red proteins. Blue protein represent the slightly attached proteins, mostly constituting the soft corona. 16
2.3 Composition of the serum proteome derived from Mass Spectrometry-Based Proteome Analysis [90]. 18
2.4 Colors of various sized monodispersed gold NPs. 22
2.5 *Optical properties of gold NPs.* a) collective oscillations of free electrons in gold when interacting with light; b)UV-Vis absorption spectra of gold NPs showing the change in the SPR intensity and peak position due to absorption of analytes. 23
2.6 *NP synthesis by the Turkevich method.* In the Turkevich-Frens method, the actual gold NP stabilizer is dicarboxy acetone resulting from the oxidation of citrate, rather than citrate itself [122]. 26

2.7 Strategy used for the synthesis of 20 nm gold NPs [118]. . 27

2.8 Size distribution of the NPs used for the experiments derived from Transmission Electron Microscopy. 27

2.9 TEM images of 20 nm gold NPs. 28

2.10 Absorbance spectrum of the 20 nm NPs: SPR exhibit the peak at $\sim$ 522 nm. 28

2.11 *Physicochemical characteristic of the synthesized gold NPs.* a) DLS measurement by intensity; b) DLS measurement by number, c) Z-Potential. 29

2.12 Schematic representation of the model used for the determination of the maximum number of bound proteins molecules. 30

2.13 Protocol for the protein corona formation. 32

2.14 Representation of TEM grids. Images from `http://www.tedpella.com/`. 34

2.15 Formulations for the preparation of the basic reagents. . 35

2.16 *Formulations for stacking and running gels.* The red square indicate the percentage of acrylamide used for the digestion experiments. 36

2.17 Purification effect on the the absorbance spectra of HS corona. 41

2.18 *Absorbance of the HS bioconjugated for all the measured samples.* a) absorbance spectra of the HS corona samples measured at different incubation time; b) absorbance spectra of the HS corona after 24 hours of incubation time ($\Delta\lambda = 8.5nm$, $\Delta I = 0.14$); c)absorbance spectra of the HS corona samples purified at different incubation time; d) absorbance spectra of the HS corona purified after 24 hours of incubation time ($\Delta\lambda = 8nm$, $\Delta I = 0.07$). 43

2.19 Time evolution of a) SPR peak position , b) Z-Potential and c) intensity of SPR peak for both purified and non-purified HS corona. 45

2.20 Time evolution of the intensity peak of the DLS for the non-purified and the purified HS corona. 46

2.21 *Absorbance of the HSA bioconjugated for all the measured samples*. a) absorbance spectra of the HSA corona samples measured at different incubation time; b) absorbance spectra of the HSA corona after 24 hours of incubation time ($\Delta\lambda = 5.5nm$, $\Delta I = 0.07$); c)absorbance spectra of the HSA corona samples purified at different incubation time; d) absorbance spectra of the HS corona purified after 24 hours of incubation time ($\Delta\lambda = 8nm$, $\Delta I = 0.07$). 47

2.22 Time evolution of a) SPR peak position , b) Z-Potential and c) intensity of SPR peak for the purified and the non-purified HSA corona. 49

2.23 Time evolution of the intensity peak of the DLS for the non-purified and purified HSA corona. 50

2.24 *Absorbance of the human IgG bioconjugated for all the measured samples*. a) absorbance spectra of the human IgG corona samples measured at different incubation time; b) absorbance spectra of the human IgG corona samples purified at different incubation time; c)time evolution of the Z-Potential for both the IgG corona. 51

2.25 Time evolution of the intensity peak of the DLS for the non-purified and purified human IgG. 51

2.26 *Effect of centrifugation and re-suspension in protein-free medium*. After short incubation time, loosely bound proteins immediately detach from NP surface inducing irreversible NP aggregation in the saline physiological medium. After long incubation time, proteins rigidly bound to NP, protecting them from aggregation induced by centrifugation and re-suspension. 53

2.27 *Results of the NP conjugation with HS and HSA.* a) time evolution of the SPR peak position, b) time evolution of the Z-Potential, c) time evolution of the intensity of the SPR peak. 54
2.28 *DLS time evolution of the hydrodynamic diameter towards stability measured by intensity for a) HS and b) HSA.* Measurements have been performed in triplicate and each colour correspond to a single DLS measurement on the analysed sample. 55
2.29 *Schematic representation of the kinetic of hard corona formation.* Purification of IgG samples always lead to agglomeration of the complexes: red-coloured part. Purification of HS corona and HSA corona lead to aggregation in the very first part of the kinetic: red-coloured part. Time stabilization effect of the NP surface associated to the protein adsorption, i.e. hardening of the protein corona, is represented by the red-to-yellow coloured part. Fully formed hard corona: green coloured part. 56
2.30 Mass spectroscopy measurement after tryptic digestion of the HS-hard corona by MALDI-TOF confirming the presence of albumin inside the HS hard corona together with some trace of a region of the IgG. 58
2.31 Schematic picture of the rationale of the protein metabolization of free proteins or hard corona proteins. Red protein: free protein generating digestion products; blue proteins: different fragment as a consequence of the digestion. 60
2.32 *Properties of the digested NP-hard corona.* a) Normalized SPR absorbance of HS hard corona b) Normalized SPR absorbance HSA hard corona. The blue line represents the purified NPs control. c) Z-Potential of the HS and HSA hard corona. 61

2.33 *Sample purification of the hard corona samples before the digestion protocol.* a) purification of the HS hard corona. Loading order: 1. Protein Marker; 2. Trypsin; 3. Supernatant of the first wash; 4. supernatant of the second wash; 5. supernatant of the third wash; b) purification of the HSA hard corona. Loading order: 1. Protein Marker; 2. HSA reference; 3. Supernatant of the first wash; 4. supernatant of the second wash; 5. supernatant of the third wash. 62
2.34 *Samples digestion and relative control.* Lane 1: protein marker; lane 2: free HS proteins; lane 3: digested free HS protein; lane 4: free HSA; lane 5: digested free HSA; lane 6: HS hard corona; lane 7: digested HS hard corona; lane 8: HSA hard corona; lane 9: digested HSA hard corona. 64
2.35 *Profile plot of digested sample.* a) profile plot of Lane 3 and 7 of the gel in Figure 2.34, b) profile plot of Lane 3 and 7 of the gel in Figure 2.34. 64
2.36 Absorbance spectra of the purified sample at different incubation time for: a) 4°C, b) RT. 68
2.37 Effect of temperature on the formation kinetic of HSA corona: a) time evolution of the SPR peak, b) time evolution of the Z-Potential, c) time evolution of the hydrodynamic radius. 69
2.38 Absorbance spectra of the purified HS corona sample: a) conjugation without stirring, b) conjugation under stirring conditions. 70
2.39 Effect of stirring conditions on the formation kinetic of HS corona: a) time evolution of the SPR peak, b) time evolution of the Z-Potential, c) time evolution of the hydrodynamic radius. 71

2.40 Absorbance spectra of the purified human albumin corona sample: a) conjugation with HSA from Sigma Aldrich (A-9511) with a degree of purity of > 97%, b) conjugation with HSA from EMD Millipor (12668-10GM) with a degree of purity of > 95%,. 72
2.41 Effect of the presence of impurity on formation kinetic of the human albumin corona: a) time evolution of the SPR peak, b) time evolution of the Z-Potential, c) time evolution of the hydrodynamic radius. 73
2.42 Conjugation of NP with BSA in SC 2.2 mM buffer: a) SPR absorbance spectra of the purified samples, b) time evolution of the SPR peak position, c) time evolution of the Z-Potential, d)time evolution of the hydrodynamic radius. 76
2.43 *Conjugation of NP with BSA in DMEM 100%*. a) absorbance spectra of the purified samples, b) time evolution of the Z-Potential. 76
2.44 *NP incubation in SC 2.2 mM buffer supplemented by HS*. a) SPR absorbance spectra of the purified samples, b) time evolution of the SPR peak position, c) time evolution of the Z-Potential, d)time evolution of the hydrodynamic radius. 77
2.45 *NP incubation in DMEM 100% supplemented by HS*. a) SPR absorbance spectra of the purified samples, b) time evolution of the SPR peak position, c) time evolution of the Z-Potential, d)time evolution of the hydrodynamic radius. 78
2.46 Protocol for the formation of the IgG corona in DMEM 100%. 79

2.47 Conjugation of NP with Imunoglobulin G in DMEM buffer: a) absorbance spectra of the purified samples, b) time evolution of the SPR peak position, c) time evolution of the Z-Potential, d)time evolution of the average hydrodynamic radius. 80
2.48 Time evolution of the DLS by intensity of the IgG-conjugated NPs. 81

3.1 *Stober synthesis*. Mono-dispersed spherical silica NPs synthesized following the Stöber-Fink-Bohn method, starting from tetraethyl orthosilicate (TEOS), water, ammonia, and absolute ethanol, as precursor. 89
3.2 Schematic diagram showing the nucleation-dependent polymerization model of amyloid fibril formation [193]. . 90
3.3 Structural prediction of p27 and Sic1. In red the inhibitory domain is indicated. 92
3.4 Lysozyme structural prediction. 93
3.5 *Tf binding* Fe^{3+}. a) Stereo Cα plot of holo-ovotransferrin. N1 and N2 represent domains N1 and N2, while C1 and C2 domains C1 and C2 respectively. Wite balls are Fe^{3+}. The figure was produced using cristallographic data [206]. b) For Fe^{3+} the co-ordination sites are octahedral, with four ligands supplied by the protein, i.e. two from tyrosinate residues, one from an aspartate residue and one from a histidine residue, plus two ligands supplied by an exogenous, bidentate carbonat [173]. 95
3.6 *Cellular uptake of iron through the Tf system via receptor-mediated endocytosis.* 96
3.7 Representative DLS by intensity results of the synthesis of 50 nm SiO_2 NPs 98
3.8 Representative size distribution of synthesized 50 nm SiO_2 NPs extrapolated from TEM images. 98

3.9 Representative TEM images of synthesized 50 nm SiO_2 NPs 99
3.10 *Immobilized-metal affinity chromatography IMAC*. a) Representation of the Ni^{2+} resin; b) Representation of the IMAC procedure. 101
3.11 *SDS-PAGE analysis of* $Sic1^{\Delta 214}$*-*His_6 *purification*. The loading order of the lanes is: lane 1 protein-marker, lane 2 total fraction of expressed protein; lane 3 not soluble fraction of expressed protein; lane 4 flow-through fraction of expressed protein; lane 5 soluble fraction of expressed protein; lane 6 first washed fraction; lane 7 second washed fraction; lane 8 Eluate 1; lane 9 Eluate 2. Lane 8 and lane 9 correspond to the eluate with higher purified protein concentration. 102
3.12 Circular dichroism of the PD-10-purified $Sic1^{\Delta 214}$-His_6. . 102
3.13 Protocol for hard corona preparation. 103
3.14 *FTIR spectra*: representative subtraction procedure for lysozyme hard corona. 106
3.15 Protein concentration in the supernatant of each centrifugation step in the presence (red line) or absence (black line) of NPs. α-Cas, α-casein; α-Syn, α-synuclein; Lyz, lysozyme; Sic1, $Sic1^{\Delta 214}$-His_6; Holo-Tf, holotransferrin; Apo-Tf, apotransferrin. 110
3.16 *SDS PAGE*. Lane 1, molecular-weight markers; lane 2, supernatant of the first centrifugation step (protein only); lane 3, supernatant of the first centrifugation step (protein + NPs); lane 4, pellet of the fourth centrifugation step (protein only); lane 5, pellet of the fourth centrifugation step (NPs only); lane 6, pellet of the fourth centrifugation step (protein+ NPs). α-Cas, α-casein; α-Syn, α-synuclein; Lyz, lysozyme; Sic1, $Sic1^{\Delta 214}$-His_6, Holo-Tf, holotransferrin; Apo-Tf, apotransferrin. 111

3.17 *Distributions of the hydrodynamic diameter measured by DLS*. A representative profile is reported for each hard corona sample, for the naked original NPs (called Fresh NPs), and for naked NPs treated by the same steps as the hard corona samples (called Control NPs). α-Cas, α-casein; α-Syn, α-synuclein; Lyz, lysozyme; Sic1, Sic1$^{\Delta 214}$-His$_6$; Holo-Tf, holotransferrin; Apo-Tf, apotransferrin. 114
3.18 Core–shell model with proteins surrounding NPs for the estimation of the protein layer thickness. NP radius of NP;$\Delta/2$ radius of protein, NP_{HC}=NP + $\Delta/2$ 116
3.19 *TEM analysis*. A representative TEM image is reported for each hard corona sample, for the naked, as synthesized NPs (Fresh NPs), and for NPs treated by the same steps as the hard corona samples (Control NPs). Scale bars for 100 and 50 nm are given. α-Cas, α-casein; α-Syn, α-synuclein; Lyz, lysozyme; Sic1, Sic1$^{\Delta 214}$-His$_6$; Holo-Tf, holotransferrin; Apo-Tf, apotransferrin. 117
3.20 *Size distribution*. Size distributions derived from 200 randomly picked NPs from each sample. α-Cas, α-casein; α-Syn, α-synuclein; Lyz, lysozyme; Sic1, Sic1$^{\Delta 214}$-His$_6$; Holo-Tf, holotransferrin; Apo-Tf, apotransferrin. 118
3.21 *Far-UV CD spectra*. Representative, normalized by maximal intensity, results reported for each hard corona sample (red), in comparison to the original protein solution (black) and the negative control (blue), in which the protein has been subjected to the same steps as the hard corona sample, in the absence of NPs. The insets show the difference spectra (hard corona minus free protein). α-Cas, α-casein; α-Syn, α-synuclein; Lyz, lysozyme; Sic1, Sic1$^{\Delta 214}$-His$_6$. 122

3.22 *FTIR spectra in the Amide I band.* Representative results are shown for each hard corona sample (red line), in comparison to the original protein solution (black line). The absorption spectra of the dehydrated protein film (left panel) and the absorption and second-derivate spectra of the D_2O-rehydrated protein film (middle and right panels) are shown. Absorption spectra have been normalized at the Amide-I band area. The peak position of selected spectral components is indicated. α-Cas, α-casein; α-Syn, α-synuclein; Lyz, lysozyme; Sic1, Sic1$^{\Delta 214}$-His$_6$; Holo-Tf, holotransferrin; Apo-Tf, apotransferrin. This figure is reproduced with kind permission of Antonino Natalello. 126

3.23 *Effect of NPs on the aggregation kinetics of α-synuclein.* ThT fluorescence signal is reported as a function of incubation time, for 0.5 mg/mL α-synuclein samples in the presence of increasing concentrations of NPs (black, 0 mg/mL; red, 2.5 mg/ml; green, 1 mg/mL; purple, 0.5 mg/mL; blue, 0.25 mg/mL). Each curve represents the mean of four replicates. 130

3.24 *Fluorescence emission spectra of the analysed samples.* a) 25 μM apo-Tf, excitation wavelength 295 nm; b) 10 mM $TbCl_3$ excitation wavelength 350 nm; c) Tb-Tf complex, excitation wavelength 295 nm; d) comparison of apo-Tf in presence and absence of Tb (red and black respectively). 132

3.25 *Fluorescent emission spectra of the analysed sample after excitation at 295 nm.* a) Black line: Tb-free Apo-Tf hard corona (Apo-Tf hard corona); red line: hard corona with the already formed Tb-Tf complexes (Tb-Tf hard corona); blue line: Apo-Tf hard corona + Tb(III); b) NPs fluorescent emission spectra; c) Difference spectra between the Tb-Tf hard corona and the Apo-Tf hard corona (red line minus blue line). 133

A.1 *Far-UV CD spectra-raw data.* Representative results are reported for each hard corona sample (red), in comparison to the original protein solution (black) and the negative control (blue), in which the protein has been subjected to the same steps as the hard corona sample, in the absence of NPs. The spectra have been normalized by the protein concentration and protein length (mean residue ellipticity). α-Cas, α-casein; α-Syn, α-synuclein; Lyz, lysozyme; Sic1, Sic1$^{\Delta214}$-His$_6$. Consistent with aggregation and scattering phenomena, the effect of loss of signal intensity is more pronounced for the two proteins that aggregate the most, lysozyme and Sic1$^{\Delta214}$-His$_6$, based on DLS consideration. 139

List of Tables

2.1 Calculation of the maximum number of bound proteins per NP, assuming just one layer of bounded protein per NP. 31
2.2 Calculation of the maximum number of bound proteins per NPtaking into account the hard spheres factor. 31
2.3 NP to protein ratio. 31
2.4 Excess of proteins *per* NP 32
2.5 Loading order of the gel in Figure 2.34 and sample preparation for the digestion. The numbers in the column "Sample" correspond to the loading order. 63
2.6 Effect of tested buffer on protein corona formation. 75

3.1 Calculated yeld of protein adsorption inside the hard corona for all the analysed protein. The experimental error in the calculation of the protein concentration of supernatants here has been derived from triplicates measurements, while for the protein concentration inside the hard corona an estimated experimental error of 30% has been used. 113
3.2 DLS measure of all the hard corona, compared to the NP control. 115

3.3 *Calculation of the hard corona thickness*. Diameter values are obtained by TEM analysis for the hard corona samples (NP_{HC}) and the control sample of naked NPs (NP). Half the difference ($\Delta/2$) is compared to the diameter of the free protein in solution derived by the relation to chain length (N) for globular proteins or IDPs depending on the type of protein. DLS measurements are also reported. The value are expressed in nm 120

List of Abbreviations

Apo-Tf	Apotransferrin
BSA	Bovine Serum Albumin
CD	Circular Dichroism
DLS	Dynamic Light Scattering
FTIR	Fourier-Transform Infrared
H/D	Hydrogen/Deuterium
Holo-Tf	Holotransferrin
HS	Human Serum
HSA	Human Serum Albumin
IDP	Intrinsically Disordered Protein
IgG	Immunoglobulin G
IMAC	Immobilized-Metal Affinity Chromatography
MS	Mass Spectrometry
NP	Nanoparticle
NMR	Nuclear Magnetic Resonance
PBS	Phosphate Buffer Saline
PB	Phosphate Buffer
SANS	Small Angle Neutron Scattering
SC	Sodium Citrate
SDS PAGE	Sodium Dodecyl Sulphate PolyAcrylamide Gel Electrophoresis
SiO_2	Silica
Tb-Tf	Terbium-transferrin complex
TEM	Transmission Electron Microscopy
Tf	Transferrin
ThT	Thioflavin T
UV-Vis	UV-Visible absorption spectroscopy

Chapter 1

General introduction

1.1 Nanoparticles

Nanoparticles (NPs) can be considered as small particles with size at the nanometric scale, which present properties that differ from the bulk material. A bulk material usually exhibit physical properties which are not size-dependent. Oppositely, at the nano-scale, the material properties can change depending on the percentage of atoms at the surface of the nanomaterial, which is strictly connected to the size of the nanomaterial itself. Various features arise from these size-dependent properties, including quantum confinement in semiconductor NPs, surface plasmon resonance in some metallic NPs and super-paramagnetism in magnetic materials. The limit size at which materials start displaying size-related properties with respect to the bulk material is material-dependent and has been proposed to be 100 nm [1, 2]. Obviously, this definition is quite generic and there is no strict boundary. Additionally, it includes different nano-sized object (nanocluster, nanopowder, nanocrystal) as well as particulate matter.

Thus, in order to distinguish NPs from general particulate matter, monodispersity becomes crucial. Among the number of ways to define the monodispersity, some of them are based on the value of the standard deviation with respect to the value of the mean size of a NPs solution. In this work, NPs are arbitrarily defined monodispersed when a predominately homogeneous NP population with >90% uniformity in size can be detected.

Therefore, despite their structural dispersion, NP can be considered as molecular entities, as they exhibit some similarity with macromolecules, such as Brownian motion, multiple reactive sites, three-dimensional structure and a high surface energy, which, in turn, can favour aggregation, a common issue in NPs and proteins [2].

In this sense, NPs assume an important scientific interest as they are effectively a bridge between bulk and atomic or molecular structures and can interact with this structure in a unique manner [1, 3]. In this context, NPs can be used as a tool to study different interaction at the nanoscale level. For example, the development of the rational design of surfaces depending on the application [4, 5] or the development of NP-based biomimetics, where NPs are used as potential replacements for the native biomolecule [6].

Due to their instability, generally naked NPs are not stable in water [1]. Consequently, their fate is to aggregate, change nature or disintegrate into atomic and molecular species [7–9]. All of this processes will result in deactivation of the NP and the aggregates or the released species can be toxic [8, 9]. In order to prevent NPs aggregation their surface engineering it is generally required to provide the NP with the repulsion forces and prevent aggregation. This can be done either by electrostatic repulsion, for example designing a double electrical layer of inorganic ions around the NP surface, or by steric repulsion, by conjugation of organic or biological molecules. Despite the crucial role of this stabilization layer, most studies focus only on the metal core of the nanostructure, overlooking the surface stabilization shell. NP has to be understood not only as a group of atoms that display some size-dependent properties which differs from the bulk form of the same material, but together with the stabilization layer that prevents the agglomeration or aggregation.

1.2 Interaction between inorganic NPs and biological system

The exponential increase in the use and production of engineered inorganic NPs with enhanced stability elicits the needing to evaluate their impact on human health and on the environment [10]. In nanomedicine, where NPs are emerging as a novel potential teragnostic tool [11, 12], a deeper understanding of the behaviour of inorganic NPs in biological media is needed, either to fully control and develop the potential of these materials, and to increase knowledge of the physical chemistry of inorganic materials when their morphology approaches that of molecular entities [2, 13].

NPs are characterized by an higher percentage of surface atoms and by the colloidal nature. Due to this characteristics once into contact with a physiological medium, NPs experience processes that transform them towards more stable thermodynamic states, which includes aggregation, corrosion, dissolution and interaction with proteins dispersed in the media. NPs interact with the environment by their surface. When the salinity of a medium is increased, the electrostatic repulsion which generally stabilized NPs is screened by adsorbed salt ions, causing fast homo-aggregation between NPs [14]. On the other side, once entered in a biological environment, NPs will inevitably come into contact with a huge variety of biomolecules, including proteins and lipids [15]. Due to the high NP surface reactivity, these biomolecules immediately coat the NPs surface forming the so-called 'protein corona' [11, 14–25], providing a stabilizing electro-steric effect upon adsorption [14]. The protein corona define the biological identity of the NP in the biological environment [26]. At the same time, the identity, properties and lifetime of these proteins on the NPS surface can affect the way cells interact with, recognize and process the NPs, and this has important implications for safety considerations and effectiveness [27]. The 'nano–bio' interface is define as the interface between the NP and the biomolecules. It comprises the dynamic physicochemical interactions, kinetics and thermodynamic exchanges between nanomaterial surfaces and the biomolecules surface. It has been stated that the nano-bio interface is composed by three dynamically interacting components [27]:

- the NP surface, which is determined by its physicochemical properties;
- the solid–liquid interface between the particle and the surrounding medium,
- the solid–liquid interface with biological substrates

In an interesting work, Nygren and Alleadine [28] showed that proteins do not distribute on NP surface randomly. Instead, once the first proteins are attached, an initial cluster of proteins assembles around, stabilizing them through a crowding effect and this mechanism is repeated until the entire surface is filled [14, 28]. The mechanism by which proteins adsorb to surfaces is mediated by different interactions, involving hydrophobic forces, Van der Waals, electrostatic and electrosteric interactions [27](figure 1.1).

The association with proteins can enhance the biocompatibility of the NPs [29]. On the other hand, some undesired collateral effects could arise from the depletion of proteins from the physiological media, or from the possible alteration of the protein structure and function and/or exposure of different epitopes. If depletion of proteins is not expected (mainly because of the low concentration of NPs), induced conformational changes of the adsorbed proteins is more realistic. In this work,

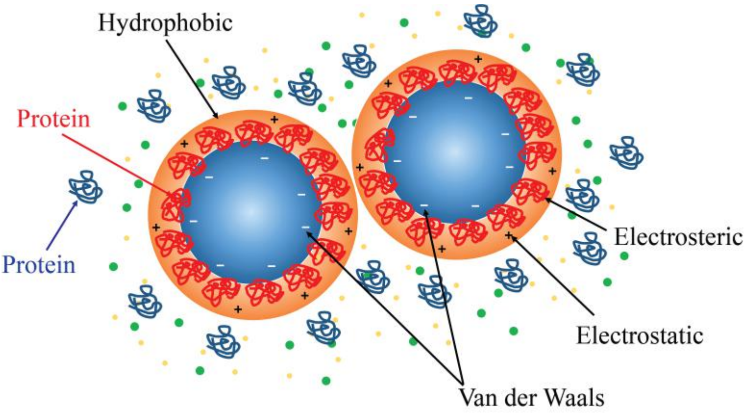

Figure 1.1: Factors that regulate the formation of the protein corona [27]).

this latter aspect is strongly investigated. A brief introduction on the protein structure is therefore needed at this point of the dissertation. Each protein has its own unique shape, which is finally determined by the interaction between the elements constituting the polypeptide chain and between the polypeptide chain and the environment [30]. From a structural point of view, a protein can exist in a well-defined globular structure characterized by four levels of structural organization:

- The primary structure of a protein refers to the specific amino acid sequence of the protein.
- The secondary structure refers to locally folded structures which form within a polypeptide due to the interactions between atoms of the backbone. The most common types of ordered secondary structures are the α-helix and the β-sheet. Both structures are held in shape by hydrogen bonds. Although the hydrogen bonds are always between the carboxilic and the amino groups, the pattern is radically different in an α-helix and a β-sheet structure. Many proteins contain both α-helices and β-sheets, however some contain just one type of secondary structure.
- The tertiary structure of a native conformation is the networked

long-range interactions stabilizing the overall three-dimensional structure of the polypeptide. The tertiary structure is primarily due to hydrogen bonding, ionic bonding and hydrophobic interactions. The disulfide bond can contribute to tertiary structure.

- The quaternary structure refers to the organization of multiple polypeptide chains in a multi-subunit protein.

On the other hand, intrinsically disordered proteins (IDPs) lack stable tertiary and/or secondary structures under physiological conditions [31, 32]. They are highly abundant in nature and their activity complements the functions of ordered globular proteins [31, 33]. IDPs exist as dynamic ensembles of interconverting structures [31]. Despite being highly flexible and intrinsically disordered, IDPs are biologically active and they are crucial in biological functions, in contrast with the classic concept that proteins require a structural order to be functional. Nonetheless, interaction with other proteins, nucleic acids, membranes, small molecules or changes in the environmental conditions can induce total or partial folding of these proteins [34, 35].

Therefore, changes in the physicochemical conditions of a protein's environment, exposition to chemicals or interactions with surfaces or interactor, can alter the interactions which define the conformation of the proteins, causing denaturation [36], in the case of globular proteins, or induced folding, in the case of IDPs [32].
Alteration of protein structure usually affect its functionality, resulting in an altered protein biological activity [27]. Moreover, changes in protein structure and function can lead to potential molecular mechanisms of injury that could contribute to disease pathogenesis.

Summarizing, NPs released in a biological environments absorb proteins onto their surfaces, forming the protein corona with possible implications for both components: proteins can suffer changes in their structure and functionality, and the formed protein corona will define the biological identity of the NP-protein complex and thus the consequent biological response in the biological environment[13–15, 37–40].

1.3 Methods for protein corona investigation

The study of interaction of proteins with NPs in biological fluids is usually complex due to the coexistence of a large number of protein in solution (more than 3,700 proteins in different concentrations) and due to the resulting competition for binding to the surface of the NP [15]. The study of protein interaction with NPs implies the investigation of numerous parameters, such as binding rates, affinities, activity of adsorbed proteins etc. Thus, the protein corona is normally identified by different parameters such as thickness, protein identity, protein quantity, protein affinity, protein arrangement and protein conformation.

A conventional approach to study the protein corona involves NPs incubation with proteins for a certain time, either complex mixtures of proteins or single protein, and centrifugation washes to isolate the protein corona from the unbound protein. After protein corona isolation, the conjugated samples are characterized by different techniques [41, 42]. Some of these techniques, namely UV–Visible spectroscopy (UV-Vis), Dynamic Light Scattering (DLS), Circular Dichroism (CD) and Fourier-Transform InfraRed (FTIR) spectroscopy are more suitable for the investigation of a single NP-protein interaction, while other techniques, such as Sodium Dodecyl Sulfate PolyAcrylamide Gel Electrophoresis (SDS PAGE), Mass Spectrometry (MS), Surface Plasmon Resonance (SPR) spectroscopy allows the investigation of the interaction of many proteins with NPs [41].

The characterization techniques used in this work are classified based on their application in NP–protein studies.

- The thickness of the protein corona influences the hydrodynamic size of the nanomaterial. DLS is a qualitative method to determine the hydrodynamic radii and the size distribution of the colloidal NP-protein corona solution. DLS has been employed to investigates the thickness of the protein corona, as well as the aggregation state of the colloidal dispersion [43]. Anyway, for the quantitative determination of the real dimension it should be combined with Transmission Electron Microscopy (TEM).

- The visualization of the protein constituting the biocorona can be achieved by SDS PAGE. This technique is also useful for the separation and qualitatively protein identification in the case of NP incubation in a complex protein mixtures, as well as the analysis of the protein segments deriving from limited proteolysis, which supply information on protein arrangement on the NP surface [39]. SDS PAGE require special protein treatment by reducing agents and anionic detergents. This treatment causes protein repulsion and thus detachment from the NP surface. The proteins resolved in the gel can be stained, and densitometry analysis based on the intensity of the stained band can be used to quantify protein abundance. SDS-PAGE is an extremely quick and cheap technique. On the other hand, protein separation in a protein complex mixture can result in co-migration in the same gel bands of several proteins. Additionally, SDS PAGE is a qualitative methods based on comparison with a reference, therefore deduce quantitative data is tricky.

- UV–Vis spectroscopy is a fast and simple technique which does not require sophisticated sample preparation. This technique can be used for the evaluation of the protein content in the protein corona, or, in the case of some metallic NP, to monitor the evolution of the protein adsorption on the surface of NPs through the evolution of the plasmonic peak (SPR) [38, 44, 45]. The plasmonic peak is highly sensitive to the surface and the environmental conditions of the NPs [46]. In particular, the adsorption of protein on the surface on NPs induces some changes on the SPR spectrum, such as broadening or shift of the absorption peak [38, 45].

- CD has been widely used for monitoring conformational changes induced by NP-protein interactions [5, 47, 48]. Although it cannot be applied on complex mixtures, CD investigation of the protein corona can provide useful information on a single protein structure adsorbed on NP surfaces by comparison of the protein corona spectra with the free protein spectra.
  Protein secondary structure posses characteristic CD signal in the the far-UV spectral region of the CD spectra (far-UV CD, 190-250 nm). This region is generally indicative of the secondary structure content of the protein because it is dominated by contributions from the amide chromophore, which are determined by the backbone conformation. Thus, different structural elements exhibit a characteristic CD spectra. For example, in the region between 200 nm and 260 nm, α-helical proteins have negative bands at 222 nm and 208 nm. Proteins with β-pleated sheets (β-sheet) have negative bands at 215 nm, while disordered proteins have very strong CD signal at 200 nm [49]. As a useful example, figure 1.2 show the secondary structure of lysozyme, which is a globular protein mainly constituted by α/β structure. Thus, its characteristic spectra arise from the contribution of the characteristics peak at 208 nm, 222 nm and 215 nm. NPs (black line in figure 1.2) are not chiral, so they do not contribute to the CD spectra.
  Finally, the CD spectrum of a protein in the near-UV region (250–350 nm) can be sensitive to some features of tertiary structure, e.g. aromatic amino acids and disulfide bonds [49, 50]. The main limitation of this technique arises from the fact the CD signal reflects an average of the entire molecular population. Thus, while CD

can determine the predominant structural content in a protein, it can not locally determine the residues involved in the specific structural portion.

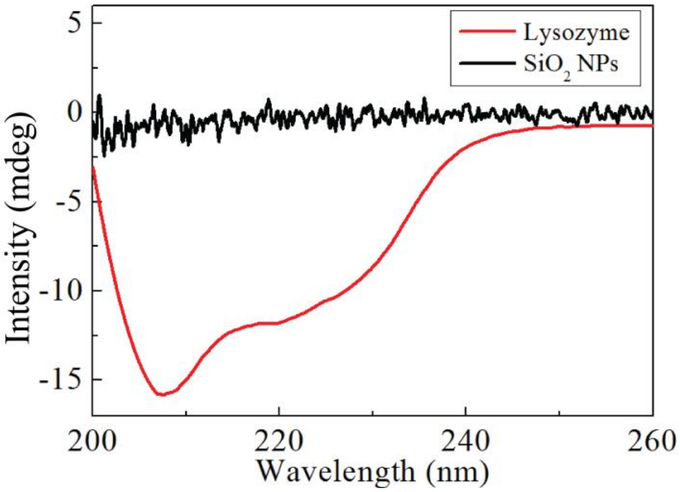

Figure 1.2: CD signal of lysozyme and silica NP.

- A more detailed and sensitive analysis of the NP-bound protein structure can be obtained by FTIR [47, 51, 52]. By this technique, the protein secondary structures are estimated based on the absorption of amide bonds in the 1600-1700 cm^{-1} region (Amide I region). The amide I band position and profile is determined by the backbone of the protein and by the hydrogen bonding pattern. Every change in the FTIR absorbance spectra of the NP-bound proteins with respect to the free protein absorbance spectra reflects a change in the protein structure. The isotopic exchange allows the identification of local unfolding o refolding with increase precision and sensibility [53, 54].

The main goal of this thesis dissertation is to study the conformational effects of protein corona formation. In the first part, UV-Vis and DLS were used to monitor the time evolution of the protein corona formation in physiological medium. In the second part, principally CD and

FTIR were used to characterize the secondary structure and the conformational rearrangement of proteins deriving from the interaction with inorganic NPs. As argued above, alteration of protein structure will affect their biological function, resulting in a contribution to disease pathogenesis.

Chapter 2

Time evolution of the protein corona

2.1 Introduction

In physiologically relevant buffers, NPs have the tendency to aggregate, mainly because of the presence of high salt concentration which shield surface charges [14, 55]. The presence of a large varieties of proteins in biological fluid can either stabilize NP dispersion or can induce aggregation [56]. Thus, the interaction with proteins influence NP fate in a physiological media [14, 16–25]. Understanding the consequences of this interaction is of crucial importance in order to evaluate their safety and toxicology. These parameters will ultimately determine their therapeutic potential [57].

The formation of the protein corona depends on multiple factors, such as the composition of the NP, its size, shape, surface state and exposure time, the nature of the media and the NP-to-protein ratio. Furthermore, the presence of ions and other interacting species can affect the interaction between proteins and NPs [14, 19, 21, 24, 25, 38, 40, 44, 58–60]. Cukalevski et al. [56] reported that the NPs fate depends also on which protein interacts with the NP surface, suggesting that isolated proteins can either induce aggregation or not. In this context, no aggregation has been observed using SiO_2 NPs with human carbonic anhydrase, cytochrome C, or ribonuclease A [61–63]. Same considerations are valid for transferrin or albumin and sulfonated polystyrene NP [64, 65]. Moreover, gold NPs seems to be stabilized by serum albumin and cytochrome C [66–69]. Oppositely, lysozyme can induce strong aggregation of silica, polystyrene, and gold NPs [65, 70–73]. Incubation of polystyrene and silica NPs with fibrinogen induce NP aggregation [74], while fibrinogen induces aggregation of poly(acrylic acid)-conjugated gold NPs in a protein-concentration dependent manner [75]. TiO_2 NPs can form large, micrometer-sized aggregates in medium containing proteins [17], while Fe_2O_3, ZnO, and surface functionalized Fe_3O_4, which are other metal oxides, are stabilized by serum proteins [76–78]. Finally, polystyrene and gold NPs can induce the formation of nanometre-sized complexes, probably consisting of proteins and multiple particles [18, 19, 21, 40, 56].

Time plays a critical role for the NP stabilization by protein corona formation [14, 38]. Alaeddine et al. [28] suggested that the formation of the corona is a dynamic process in which proteins do not adsorb on surfaces randomly. In complex protein mixture, the protein corona changes over time depending on the surrounding protein concentration and their affinities for the NP surface [14]. Once the first proteins are attached, unbound proteins stabilize the surface through crowding effects [14]. This mechanism is repeated until the entire surface is occupied. Thus, the initial attachment of a protein to a surface is followed by a set of re-organizational arrangements, which make this attachment more stable and, finally, irreversible. Therefore, not only affinities but also time-dependent related mechanisms such as molecular relaxation and/or structural rearrangements have been identified as crucial factors in making the adsorption irreversible [14, 38].

Irreversible adsorption of proteins through these time-dependent stabilization mechanisms has important implications in the case of complex mixtures of proteins such as blood serum, plasma, etc. According to the Vroman Effect [79], which define the rapid exchange of plasma proteins at liquid-solid interfaces reflecting the competitive adsorption of plasma proteins for a limited number of surface sites, fast exchanging proteins with low affinity do not generate strong attachment to the surface (Figure 2.1).

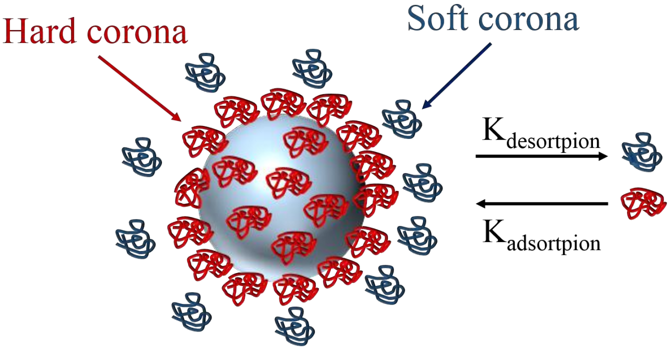

Figure 2.1: *Dynamic in-solution equilibrium between hard and soft corona [80].* Fast exchanging proteins with low affinity are characterized by high $k_{adsorption}$ and $k_{desorption}$).

Therefore, the protein corona is not a fix layer, and its composition is determined by the kinetic rate of adsorption and desorption of each protein [81]. In the case of complex mixture of proteins, initially the "Soft" corona is formed by the more abundant and mobile proteins which coats the NP surface by weak and dynamic interactions, setting an equilibrium between bound and unbound proteins and stabilizing the colloid in the physiological medium. As exposition time become longer the adsorption equilibrium shifts towards the adsorption of proteins with higher surface affinities, altering the initial corona composition (Figure 2.2). At the same time, the bound proteins are stabilized by an ensemble of stabilization mechanisms, i.e. conformational rearrangements of adsorbed proteins and crowding effects. The exposition time, via such stabilization mechanisms, hardens the proteins layer bringing it to a steady, practically irreversibly bound state: the so-called "Hard" corona

[14, 82].

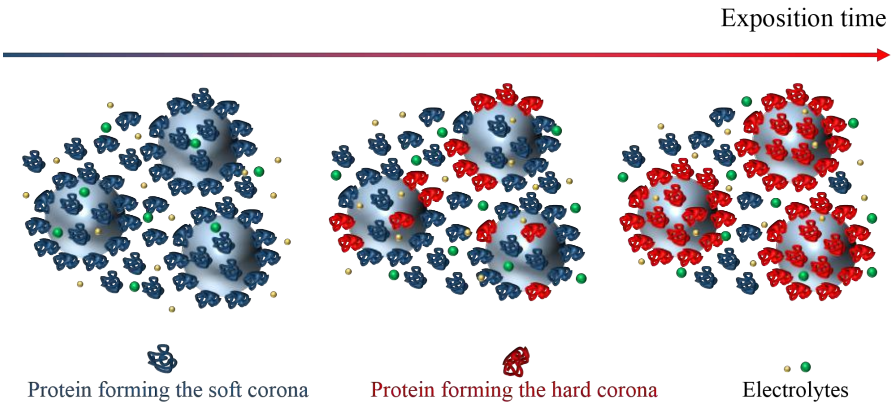
Exposition time
Protein forming the soft corona
Protein forming the hard corona
Electrolytes

Figure 2.2: *Hardening of the NP-protein corona.* As exposition time increase, proteins tightly adsorb to NP surface, gradually forming the hard protein corona, represented by red proteins. Blue protein represent the slightly attached proteins, mostly constituting the soft corona.

Therefore, incubation time plays a fundamental role in the formation of the hard protein corona, the colloidal stability of NP-protein conjugates and to the final composition of the resulting hard protein corona. The comprehension of this process is of paramount importance considering the long in-vivo circulation time of NPs [83] .

In a recent work, Karmali and Simberg [84] reviewed the identification of plasma proteins adsorbed to different NPs. The emerging picture suggests a strong correlation between the surface chemistry and the resulting composition of the biocorona. Polymeric and liposome NPs exhibit enhanced affinity for apolipoproteins with respect to inorganic NPs. Gessner et al. [85] reported that the hydrophobicity of the polymeric NP influences the adsorption of ApoA-I, ApoA-IV, ApoC-III, and ApoJ, which gradually disappear with decreasing hydrophobicity of the NPs surface. Polymeric NPs and NPs with hydrophobic surface component or hydrophilic inorganic NPs preferably adsorbs transferrin, haptoglobin, fetuin A (alpha-2-HS-glycoprotein), kininogen, histidine-rich glycoprotein, while albumin shows affinity for hydrophobic surfaces and polyanions.

In many works, it has been proposed that most abundant proteins (e.g., albumin and fibrinogen) are adsorbed first but then displaced by proteins with higher surface affinity [22, 23, 86–88].

However, a recent report using proteomic analysis showed that the corona deriving from incubation in plasma is qualitatively established within minutes and its composition (i.e., the ratio of the different proteins) does not change in time for several types of NPs (negatively or positively charged polystyrene NPs and silica NPs of various sizes, charge and surface modifications) [25]. Oppositely, Dobrovolskaia et al. [21], reported that the proteins that bind polymeric, iron oxide and gold NPs, and liposomes and carbon nanotubes, are mainly albumin, apolipoprotein, immunoglobulins, complement, and fibrinogen, which are the most abundantly species in plasma. Casals et al. [38] studied the time evolution of the NP-protein corona on citrate stabilized gold NPs in complete Cell Culture Media (DMEM + Fetal Bovine Serum) revealing that albumin is the most abundant component in the hard corona.

2.1.1 Goals and strategy

The poor knowledge of the nanomaterials responses and evolution inside biological media is recognized as one of the key points underpinning the mentioned controversies on protein corona composition [89]. The develop of a reliable and efficient protocol (low-cost, no time-consuming) and a deeply understanding of the factors affecting the NP-protein conjugation is strongly needed.

In this part of the thesis dissertation is reported the study of the time evolution of the protein corona arising from the incubation of 20 nm citrate-stabilized gold NPs with human serum (HS), human serum albumin (HSA) and Immunuglobulin G (IgG). The protein corona has been prepared in a physiological medium, namely Phosphate Buffer (PB) 10 mM pH 7.4. The evolution towards the formation of the hard protein corona is the so-called hardening of the NP-protein corona.

Here, the time evolution of the NP-protein corona in the case of the conjugation with only one specific protein, i.e NPs incubated with only HSA or only IgG, has to be understood as a fingerprint of the adsorbtion of that specific protein. Thus, the study of the evolution of the protein corona resulting from the incubation of NP in HS can supply information about the composition of the hard protein corona. The determination of the final composition is deduced from the comparison between the time evolution of the HS corona and the time evolution of the protein corona resulting from the incubation with only HSA and only IgG, which are the main components of the HS.

Albumin and the immunoglobulins account for approximately 75% of the total protein weight in HS. In particular, HSA represents about the 55% of the total protein weight. Some additional protein species constitute most of the remaining weight (about 20 species). Low abundant proteins correspond to only approximately 1% of the protein weight in serum [90]. Figure 2.3 summarizes the composition of the serum proteome derived from Mass Spectrometry-Based Proteome Analysis.

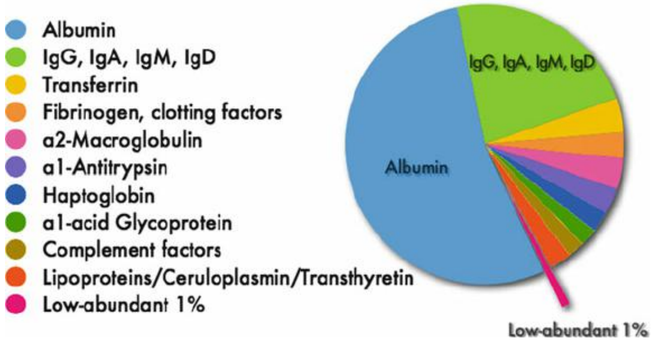

Figure 2.3: Composition of the serum proteome derived from Mass Spectrometry-Based Proteome Analysis [90].

In this work, the time evolution of the protein corona arising from the NPs incubation with HS is compared with the evolution of the protein corona arising from NPs incubation with only HSA and only IgG (the main components of the HS).

The process of the hardening of protein corona has been followed over time studying the time evolution of the physicochemical properties of colloid by the UV-Visible (UV-Vis) Absorption Spectroscopy and by measurements of hydrodynamic radii and aggregation state by DLS and surface charge by Z-Potential.

Purification of the NP-bound from the unbound proteins at different incubation time has been used as a tool to determine the hardening process of the protein corona in PB 10 mM pH 7.4. Purification consisted in cycles of sample centrifugation and re-suspension in a protein-free medium. Experimental results show that at the initial incubation stage, loosely bound proteins forming the soft corona detach from the surface as effect of the purification and NPs aggregate due to the scarce surface protection. Gradually, the hardening of the protein corona take place and the adsorbed proteins protect the NP surface from aggregation induced by the centrifugation.

In many studies, HSA is found to be the most abundant component of the resulting hard corona deriving from the incubation with serum proteins [21, 38]. According to these studies, the results show that the kinetic of the evolution of the protein corona deriving from incubation in HS recall the physicochemical dominance of HSA with some minor difference probably connected to the presence of minor compounds inside the HS hard corona.

Once formed, the hard corona has been further characterized by investigating its stability against protein desorption with time. The results show that the fully formed hard corona consistently maintains its properties with time, until three days. Thus, when compared with many biological and physiological phenomena, the hard corona lifetime is long enough to define the biological identity of the NPs [40].

The study of the level of packing of the protein inside the hard corona provide informations about the protection of the surface against the degradation of the bioconjugates and help to understand the effect of their possible natural metabolic degradation in biological environment [44]. Physicochemical features of the NP-protein complexes are important factors that are strictly related to the NPs biodistribution, which is critical for understanding their potential toxicity, e.g. in-vivo release of toxic ion deriving from NP dissolution The degree of packing of the protein constituting the protein corona has been tested by investigating the hard corona ability to protect the NPs against the strongly etching effect of sodium cyanide (NaCN) [91, 92] and against Nitric Acid (HNO_3) induced aggregation. When CN anions directly interact with the inorganic core, they form complexes with the gold atoms, progressively etching the NP surface. This converts the reddish NP sample into a colorless solution of $Au(CN)_2^-$ ions [93]. On the other side, the addition of HNO_3 on citrate-stabilized NP solution induces the protonation of the citrate. NPs lose their stability and aggregate as a consequence of the buffer protonation. In addition, the resulting spectra indicate that NPs aggregation is accompanied by NPs dissolution.

Proteins forming the hard corona can undergo structural rearrangements in the adsorbed state [41, 94]. In this work, limited proteolysis experiments have been employed to probe the conformational state of proteins. Generally, the sites of limited proteolysis along the polypeptide chain of a protein are characterized by enhanced backbone flexibility, implying that proteolytic probes can detect sites of local structural rearrangements in the protein chain [95].

In this work, protein digestion by trypsin was used as a simple biochemical method which can supply information regarding conformational changes of adsorbed proteins. Results show a decrease of regions exposed to trypsin digestion of proteins constituting the conjugates, probably due to a more static protein conformation in the adsorbed state together with a NP shielding effect.

Finally, in the last part of this chapter the effect of some experimental parameters on the protein corona hardening kinetics have been investigated. In particular, the effect of temperature, stirring conditions, purity of protein powder and the type of buffer have been tested on the hard corona formation kinetics. Some of these parameters strongly affect the hardening evolution of the protein corona.

2.1.2 Scientific relevance of the selected materials

In this subsection, a brief, general description of the selected materials and their biological importance is supplied for a better understanding of the following sections.

Gold nanoparticles

Colloidal gold NPs possess useful size- and shape-related optoelectronic properties [96], large surface-to-volume ratio and multiple surface functionalities, which make them extremely attractive in a variety of application, such as photovoltaic, sensory probes, therapeutic agents, drug delivery in biological and medical applications, electronic conductors and catalysis [97–103]. In bionanotechnology, thanks to the enhanced biocompatibility and low toxicity [104], together with the easy surface functionalization, gold NPs provides a versatile platform for nanobiological assemblies with, for example, oligonucleotides [105–107], antibodies [108, 109], and proteins [110, 111]. Biomolecules conjugated-gold NPs are becoming promising instruments for adressing challenges faced by the investigation of biological systems [112].

Spherical gold NPs exhibit a range of colors (from red to clear purple) in aqueous solutions as the NP size increases from 2 to 100 nm. Figure 2.4 shows the change in color from red to purple due to increasing NP size from ∼15 nm to ∼60 nm. Additionally, gold NPs show a size-relative absorption peak from 500 to 550 nm [113]. This absorption band arises from the collective oscillation of the conduction electrons due to the resonant excitation by the incident photons, which is called "surface plasmon band" (SPR), and is influenced by size, shape, solvent, surface ligand, temperature and it is also sensitive to the proximity of other NPs [46, 114] (Figure 2.5 a). The binding between analytes and gold NP can alter the SPR absorbance band, leading to a detectable response [115, 116]. Thus, the SPR is very sensitive to any surface adsorption of compounds and to the physicochemical characteristic of the medium. In detail, adsorption of proteins lead to a small increase of the intensity of the SPR absorbance peak and a read shift of the peak position, as exemplify by the red line in Figure 2.5 b).

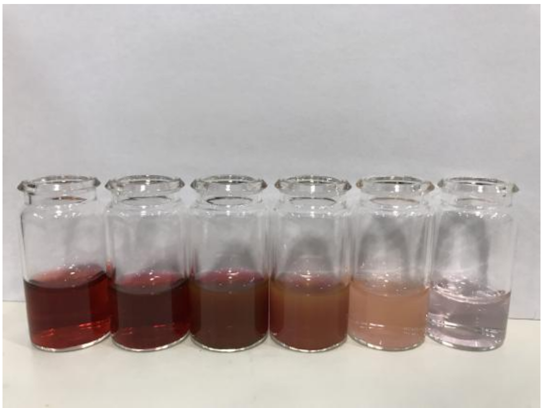

Figure 2.4: Colors of various sized monodispersed gold NPs.

Physiologically relevant buffer usually contain a relevant amounts of salts. When an excess of salt is added to the gold NP solution, the surface charge of the NP becomes neutral, causing aggregation of NPs. The aggregation of NPs results in the significant red-shifting of SPR frequency, the broadening of surface plasmon band and changing the solution color from red to blue due to the interparticle plasmon coupling [117].

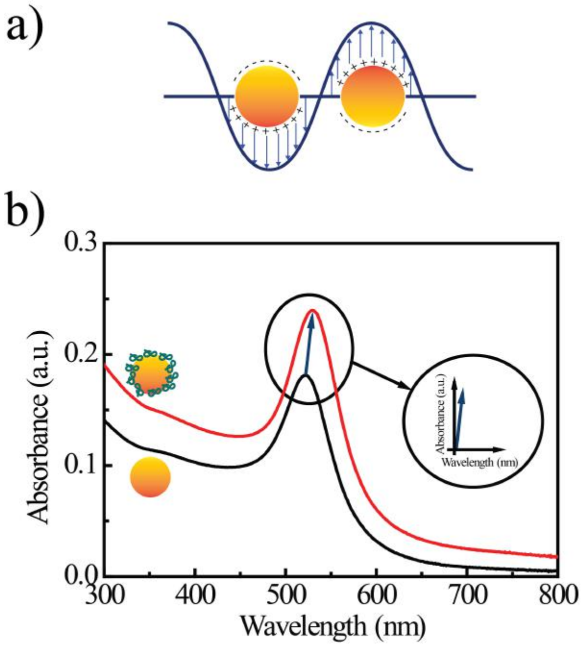

Figure 2.5: *Optical properties of gold NPs.* a) collective oscillations of free electrons in gold when interacting with light; b)UV-Vis absorption spectra of gold NPs showing the change in the SPR intensity and peak position due to absorption of analytes.

In this work, gold NPs were synthesized according to the method developed by Bastús et al. [118]. This method is based on the classical Turkevich/Frens reaction system [119], by reduction of chloroauric acid ($HAuCl_4$) with sodium citrate.

Proteins

IgG and HSA proteins have been used for bioconjugation, as they represent the majority of the protein molecules in serum. The consequence of the adsorption regarding the functionality of these proteins has not been investigated. Thus, just a brief explanation of their role in human body is presented for completeness.

Immunoglobulin G

Immunoglobulins (Ig) are heterodimeric proteins composed of two heavy (H) and two light (L) chains [120]. They can be separated functionally into variable (V) domains, that binds antigens, and constant (C) domains, that specify effector functions (for example activation of complement). There are five main classes of heavy chain C domains. Each class defines the IgM, IgG, IgA, IgD, and IgE isotypes. IgG can be split into four subclasses, IgG1, IgG2, IgG3, and IgG4, each with its own biologic properties [120]. IgG is the predominant isotype found in the body. It has the longest serum half-life of all immunoglobulin isotypes and contribute directly to an immune response including neutralization of toxins and viruses [120].

Human serum albumin

Human serum albumin (HSA) is the most abundant protein in human serum with a molecular weight of 66.437 Da. Albumin functions primarily as a carrier protein for steroids, fatty acids, and thyroid hormones and plays a role in stabilizing extracellular fluid volume.

Human serum

Human serum is generally obtained from blood plasma after fibrinogen and other clotting factors have been removed. It is an aqueous solutions (about 95% water) containing a variety of substances including proteins and peptides (such as albumins, globulins, lipoproteins, enzymes and hormones), nutrients (such as carbohydrates, lipids and amino acids), electrolytes, and variety of other small organic molecules [121]. In this complex mixture of proteins and electrolytes, albumin and immunoglobulins account for approximately 75% of the total protein weight [90].

2.2 Materials and methods

2.2.1 Synthesis of gold NPs

In this work, gold NPs were synthesized according to the method developed by Bastús et al. [118], which is a seeded growth strategy for the synthesis of size- and shape-controlled large citrate-stabilized gold NPs based on the classical Turkevich/Frens reaction system [119].

Reagents

Gold(III) chloride trihydrate $HAuCl_4 \cdot 3\,H_2O$ (Sigma 520918) and sodium citrate tribasic dihydrate (S-4641) were purchased from Sigma Aldrich (St. Louis, MO). Deionised water with resistivity $\sim$ 18.2 MΩ has been used in all the experiments. All glasswares were firstly immersed in acidic bath, then abundantly rinsed in deionised water, and successively immersed in basic bath overnight. Before the use glasswares were abundantly rinsed in deionised water.

Synthesis and characterization of gold NPs

This strategy is focused on the inhibition of secondary nucleation during the homogeneous growth process, allowing the enlargement of presynthesized gold NPs via the surface-catalyzed reduction of Au^{3+} by sodium citrate [118].

The initial step of this multiple-step process is the oxidation of citrate, that yields dicarboxy acetone. Thus, an aqueous solution of 150 ml volume of sodium citrate 2.2 mM were boiled under reflux and under vigorous stirring for 15 min. Then, 1 ml of a 25 mM Gold(III) chloride hydrate ($HAuCl_4$) solution was rapidly added by a syringe into the boiling solution. In this step, auric salt is reduced to aurous salt and Au_0, and the aurous salt is assembled on the Au_0 atoms to form the AuNP (Figure 2.6).

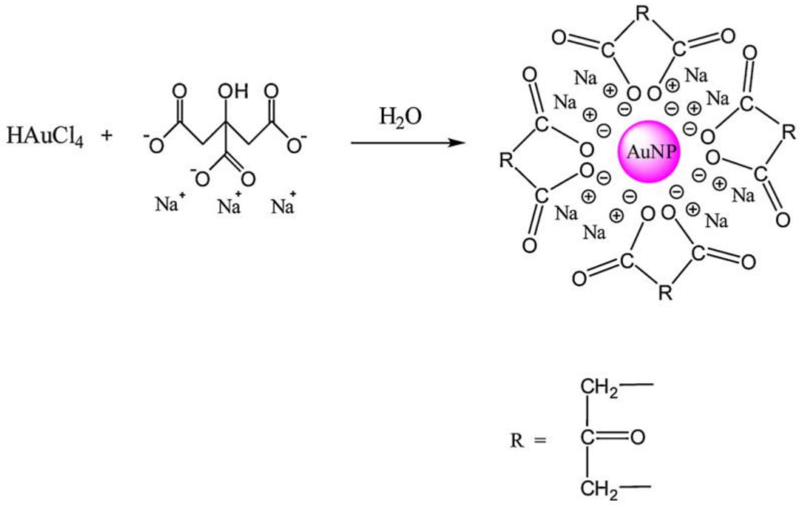

Figure 2.6: *NP synthesis by the Turkevich method.* In the Turkevich-Frens method, the actual gold NP stabilizer is dicarboxy acetone resulting from the oxidation of citrate, rather than citrate itself [122].

The color of the solution rapidly changed from transparent to dark gray and then to red in 2 minutes. The resulting NPs size is ∽ 10 nm and the concentration is $\sim 3 \times 10^{12}$ NPs/mL. The NPs are coated with negatively charged citrate ions and hence are stable in H_2O (Figure 2.6). After 5 min the solution was cooled down until 90 °C. Then 1 ml of 60 mM sodium citrate and 1 ml of 25 mM $HAuCl_4$ were sequentially injected. To avoid the second nucleation, the ratio between seeds and gold monomer should be kept into a certain value. Thus, before any precursor addition, a dilution is performed. The NP size and concentration is controlled by the number of precursor addition. 20 nm gold NPs at a concentration of $\sim 3 \times 10^{12}$ NP/ml have been used. The desired size has been obtained by two precursor injections into the 90°C solution. Figure 2.7 summarizes the strategy of the synthesis.

Figure 2.8 represents the size distribution of the NPs used for the experiment, extrapolated from TEM images represented in Figure 2.9.

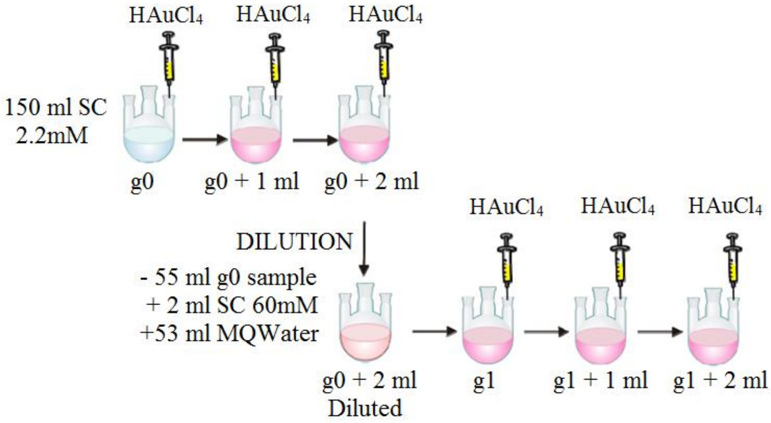
HAuCl4
HAuCl4
HAuCl4
150 ml SC
2.2mM
g0
g0 + 1 ml
g0 + 2 ml
DILUTION
- 55 ml g0 sample
+ 2 ml SC 60mM
+53 ml MQWater
HAuCl4
HAuCl4
HAuCl4
g0 + 2 ml
Diluted
g1
g1 + 1 ml
g1 + 2 ml

Figure 2.7: Strategy used for the synthesis of 20 nm gold NPs [118].

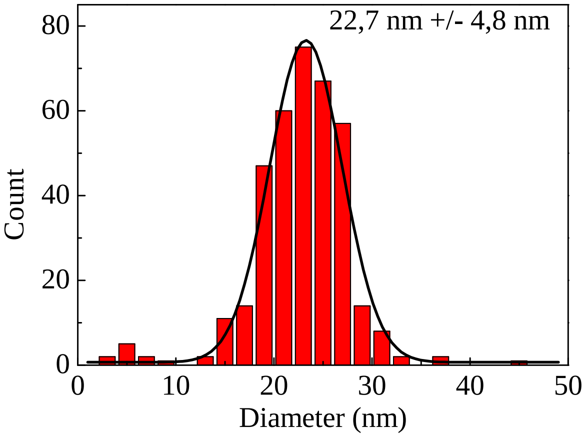

Figure 2.8: Size distribution of the NPs used for the experiments derived from Transmission Electron Microscopy.

Figure 2.10 shows the absorbance spectra of the 20 nm NPs used for the experiments. The SPR is characterized by the presence of the SPR peak at $\sim$ 522 nm, corresponding to a $\sim$ 20 nm gold NP, according to the size distribution derived from TEM images.

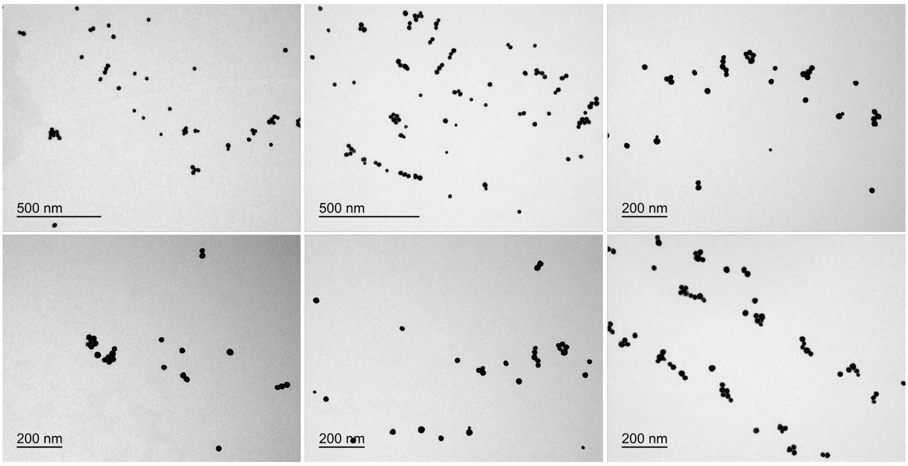
500 nm
500 nm
200 nm
200 nm
200 nm
200 nm

Figure 2.9: TEM images of 20 nm gold NPs.

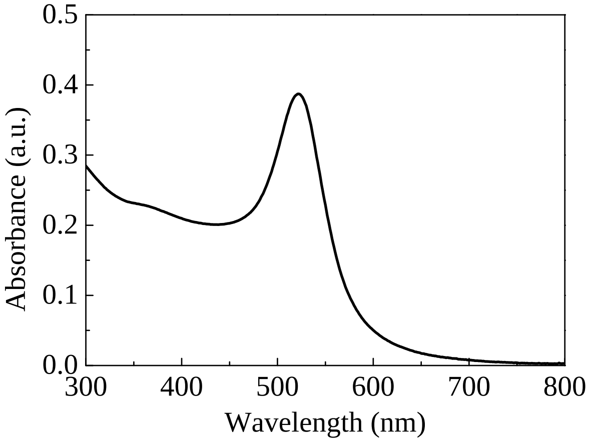

Figure 2.10: Absorbance spectrum of the 20 nm NPs: SPR exhibit the peak at ∼ 522 nm.

Figure 2.11 represent the physicochemical characteristic of the 20 nm citrate-stibilized gold NPs synthesized by this method.

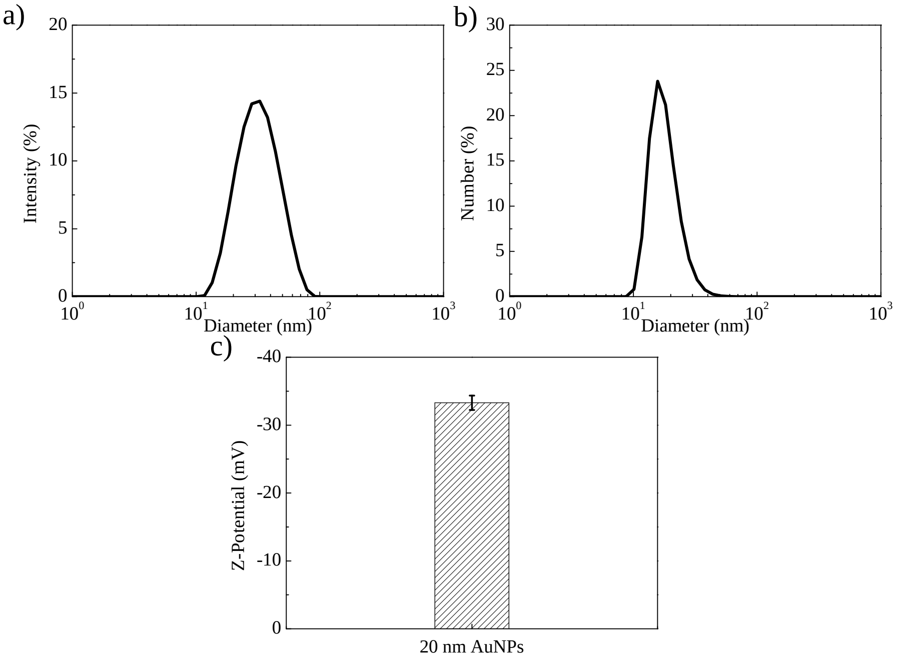

Figure 2.11: *Physicochemical characteristic of the synthesized gold NPs.* a) DLS measurement by intensity; b) DLS measurement by number, c) Z-Potential.

2.2.2 Proteins

Human serum (HS) from human male AB plasma(H-4522), albumin (HSA) from human serum (A-9511) and IgG from human serum (I-4506) were purchased from Sigma Aldrich (St. Louis, MO). All the proteins and NP stock solutions were prepared in 10 mM Phosphate Buffer, pH 7.4. Sodium phosphate dibasic (S-5136) and Sodium phosphate monobasic (71496) were also purchased from Sigma Aldrich.

2.2.3 Bioconjugation protocol

The calculation of the dependence of the hydrodynamic radius on the number of protein molecules bound to a spherical NP has been done assuming that the protein-coated NP can be approximated by a sphere.

The hydrodynamic radius of the NPs-protein complexes, R_H, is derived from equation 2.1.

$$\frac{4}{3}\pi R_H^3 = V_{NP} + N_{MAX} V_{PROT} \tag{2.1}$$

Where V_{NP} is the volume of the NP, N_{MAX} is the maximum number of bound proteins and V_{PROT} is the molecular volume of the protein molecules [68, 123–125]. Figure 2.12 represents the model used for the determination of the maximum number of bound protein molecules.

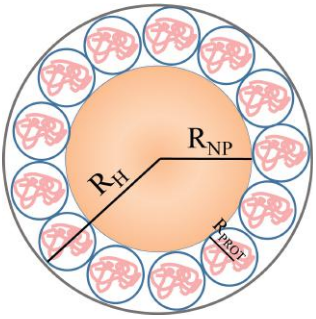

Figure 2.12: Schematic representation of the model used for the determination of the maximum number of bound proteins molecules.

A typical density of the protein solution of about 1.35 mg/ml has been assumed [126]. Protein size has been estimated by bioinformatic tool from protein molecular weight [127]. The calculation estimates the molecular weight as 120 g/mol per amino acid residue, and diameter from empirical results of several model proteins. For the HS, the protein size is an average value of all the proteins present [128]. Table 2.1 reports the maximum number of bound proteins per NP, assuming just one layer of bounded protein per NP.

This calculation doesn't take into account the hard spheres factor, which refers to the occupancy of a sphere taking as a model a random close packing system. The hard spheres factor can be estimated as 0.65. The

Protein	R_{PROT} (nm)	R_{NP} (nm)	N_{MAX}
HSA	3	10	114
HS	3,2	10	102
IgG	4	10	75

Table 2.1: Calculation of the maximum number of bound proteins per NP, assuming just one layer of bounded protein per NP.

calculation of the maximum number of bound proteins *per* NP taking into account the hard spheres factor is reported in table 2.2.

Protein	R_{PROT} (nm)	R_{NP} (nm)	N_{MAX}
HSA	3	10	74
HS	3,2	10	66
IgG	4	10	49

Table 2.2: Calculation of the maximum number of bound proteins per NPtaking into account the hard spheres factor.

table 2.3 reports the NP to protein ratio used in the experiment. The protein final concentration is 5 µM for all the samples, and corresponds to 3×10^{15} molecule/ml.

Protein	[Proteins] (molec/ml)	[NPs] (NP/ml)	Prot/NPs
HSA	3×10^{15}	3×10^{11}	1×10^{4}
HS	3×10^{15}	3×10^{11}	1×10^{4}
IgG	3×10^{15}	3×10^{11}	1×10^{4}

Table 2.3: NP to protein ratio.

The bioconjugates were obtained by adding a 100× excess of proteins to ensure a complete surface coverage, as indicated in Table 2.4.

The protocol used for the bioconjugation is illustrated in Figure 2.13.

The centrifugation parameters for the purification has been determined according to Stokes law reported in equation 2.2 which govern the

Protein	N_{MAX}	Prot/NPs	Excess of protein
HSA	74	1×10^4	135
HS	66	1×10^4	151
IgG	49	1×10^4	204

Table 2.4: Excess of proteins *per* NP

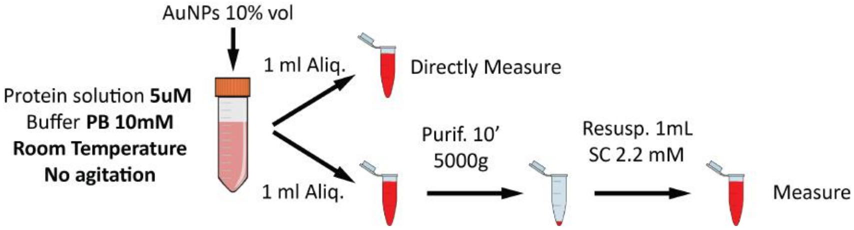
AuNPs 10% vol
Protein solution **5uM**
Buffer **PB 10mM**
Room Temperature
No agitation
1 ml Aliq.
Directly Measure
1 ml Aliq.
Purif. 10'
5000g
Resusp. 1mL
SC 2.2 mM
Measure

Figure 2.13: Protocol for the protein corona formation.

sedimentation process of colloidal particles.

$$v = \frac{2}{9}\frac{\rho_v - \rho_f}{\mu} g R^2 \tag{2.2}$$

In the equation 2.2, ρ_v is the density of the particles material, ρ_f is the density of the fluid, g is the gravitational acceleration, R is the radius of the spherical particle and μ the dynamic viscosity. According to Stokes law, the sedimentation velocity of a colloidal particle which undergoes the gravitational force g can be calculated knowing the diameter of the particle, the density of the particle, the fluid density and the fluid viscosity. Defining a reasonable multiplication factor for g, the sedimentation time can be calculated from the calculated sedimentation velocity. At different time point, an aliquot of the sample is purified to remove the unbound protein excess and then resuspended in sodium citrate (SC) 2.2 mM and measured. The buffer conductivity is 0.8 mS/cm, which provide a reliable value of the Z-Potential electrophoretic mobility. The purification control is performed to verify the effectiveness of the washing cycle and consisted in the direct measurement of the NP-protein complexes without purification.

2.2.4 Characterization techniques

UV-Visible Spectroscopy

UV-Vis spectra were acquired on a Agilent Cary 60 UV-Vis Spectrophotometer. A total volume of 1 ml of the analysed sample was placed in a plastic cell and the spectral analysis was performed between 300 nm and 800 nm at room temperature. Cary WinUV software by Agilent has been used to collect the spectrophotometer output.

DLS and Z-Potential measurements

The hydrodynamic diameter and the surface charge of the colloids were measured by Dynamic Light Scattering (DLS) and Z-Potential on a Malvern Zetasizer Nano ZS90 which incorporates a Z-potential analyser (Malvern Instruments Ltd, Worcestershire, UK). The samples were prepared at an average concentration of $\sim 3 \times 10^{11}$ NPs/mL in SC 2.2 mM (pH 7.8) and were allowed to equilibrate at 25 °C for 30 seconds before the analysis.

Transmission electron microscopy

Gold NPs were visualized using a 80-keV transmission electron microscope JEOL 1010 equipped with a Orius (Gatan) CCD Camera. TEM grids are represented in Figure 2.14 and consist on a ultrathin-formvar coated 200 mesh copper grid covered with a layer of carbon (ted-pella, Monocomp, Madrid, Spain). The heat and electrical conducting properties of carbon help stabilizing the Formvar films when exposed to the electron beam.

The TEM grids were prepared by the dipping procedure, which consists in the direct immersion of the grids in the NP solution an letting them dry in open atmosphere overnight.

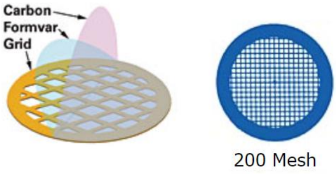

Figure 2.14: Representation of TEM grids. Images from `http://www.tedpella.com/`.

Gel Electrophoresis

Sodium dodecyl sulphate polyacrylamide gel electrophoresis (SDS-PAGE) at 16% acrylamide concentration was used to visualize the proteins recovered from hard corona samples. Proteins were detached from the NP surface by boiling 5 min in SDS sample buffer (2% w/v SDS) [129]. The electrophoresis was performed according to SDS-PAGE original protocol, on a Mini-PROTEAN Tetra cell for 1-D vertical gel electrophoresis apparatus for Bio-Rad minigels. Molecular-weight standards consisting in a mixture of ten blue-stained recombinant proteins (10–250 kD). Finally, gels were stained in Coomassie blue.

Reagents and buffer formulation

Sodium dodecyl sulphate (L-3771), 2-Mercaptoethanol (M-7154), trizma base (T-1503), glycerol (G-5516), bromophenol blue sodium salt (B-8026), ammonium persulfate (A-3678) and hydrochloric acid (30721-M) were purchased from Sigma Aldrich (St. Louis, MO).
40% acrylamide/bis-acrylamide solution, 37.5:1 (161-0148), Coomassie blue (BIO-RAD 161-0786) and molecular-weight standards (161-0373) were purchased from BIO-RAD.

The buffers were prepared by following the formulation reported in Figure 2.16.

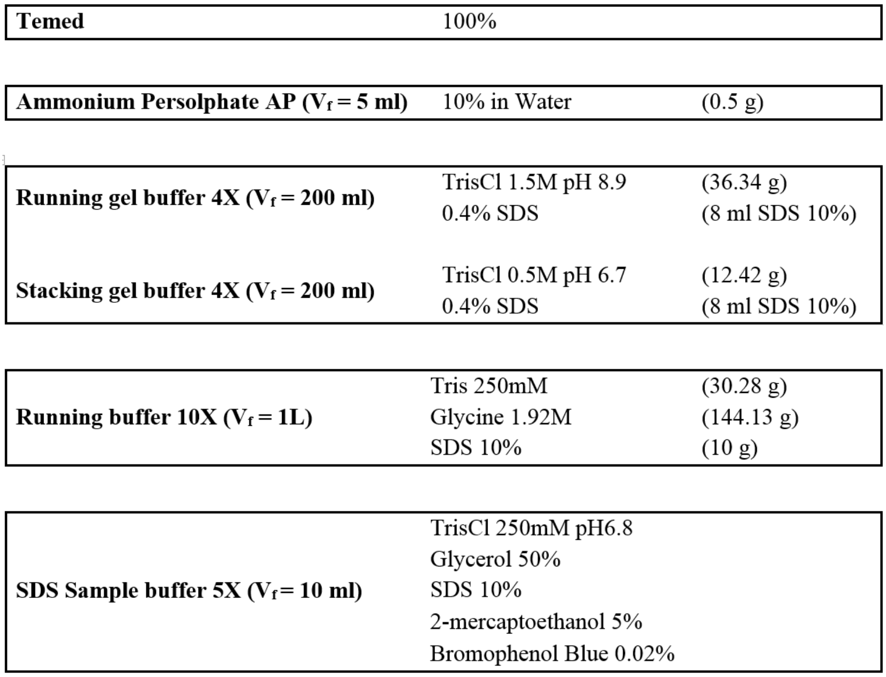

Temed	100%	

Ammonium Persolphate AP (V_f = 5 ml)	10% in Water	(0.5 g)

Running gel buffer 4X (V_f = 200 ml)	TrisCl 1.5M pH 8.9 0.4% SDS	(36.34 g) (8 ml SDS 10%)
Stacking gel buffer 4X (V_f = 200 ml)	TrisCl 0.5M pH 6.7 0.4% SDS	(12.42 g) (8 ml SDS 10%)

Running buffer 10X (V_f = 1L)	Tris 250mM Glycine 1.92M SDS 10%	(30.28 g) (144.13 g) (10 g)

SDS Sample buffer 5X (V_f= 10 ml)	TrisCl 250mM pH6.8 Glycerol 50% SDS 10% 2-mercaptoethanol 5% Bromophenol Blue 0.02%

Figure 2.15: Formulations for the preparation of the basic reagents.

In the preparetion of polyacrylamide gels, the ammonium persulfate (AP) and N,N,N′,N′-tetramethylethylenediamine (TEMED) form the free radicals needed for polymerization. TEMED accelerates the decomposition of persulfate molecules into sulfate free radicals and these in turn initiate the polymerization.

Gels for electrophoresis are composed of two part, which differs in the acrylamide percentage. The lower part of the gel is called running gel, where separation by molecular mass takes place. The upper part is the stacking gel. Samples initially are loaded on the gel trough the pockets created in the stacking gel. Formulations for the stacking gel and the running gel are reported in Figure 2.16. The concentrations of acrylamide determines the pore size of the polymer, which consequently affects the migration rate of the proteins. Small size pores slow down the migration rate. Slowing down the migration rate is useful in case of small proteins or when better separation/resolution is needed (for example the case of complex mixtures of proteins).

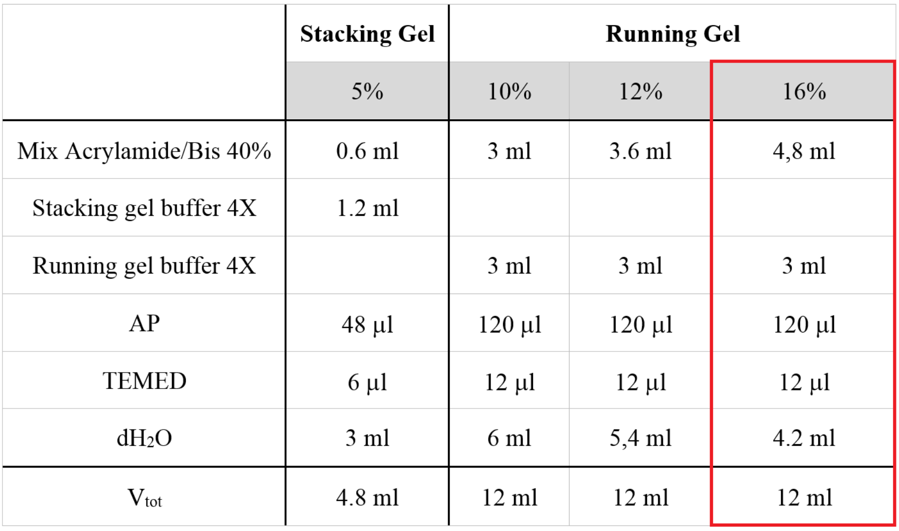

	Stacking Gel	Running Gel		
	5%	10%	12%	16%
Mix Acrylamide/Bis 40%	0.6 ml	3 ml	3.6 ml	4,8 ml
Stacking gel buffer 4X	1.2 ml			
Running gel buffer 4X		3 ml	3 ml	3 ml
AP	48 µl	120 µl	120 µl	120 µl
TEMED	6 µl	12 µl	12 µl	12 µl
dH_2O	3 ml	6 ml	5,4 ml	4.2 ml
V_{tot}	4.8 ml	12 ml	12 ml	12 ml

Figure 2.16: *Formulations for stacking and running gels.* The red square indicate the percentage of acrylamide used for the digestion experiments.

Assembling the gel The first part to be added into the gel plates is the running gel. Isopropanol (Sigma I-9516) was added on the top of the running gel to obtain a flat surface of the polymer. Polymerization of running gel takes about 20 minutes. Successively, isopropanol is discarded and the stacking gel is added on the top of the running gel. Finally, a comb is rapidly inserted to generate the pockets in the stacking gel. Polymerization of the stacking gel take about 30 min. Gels can be stored at 4°C up to 1 week.

Sample preparation Samples for SDS-PAGE were prepared according to original Laemmli procedure [129] in diluted gel buffer (SDS sample buffer) containing sodium dodecyl sulphate (SDS), 2-mercaptoethanol, glycerol, and bromophenol blue tracking dye. Proteins were boiled in SDS sample buffer containing 5% (v/v) 2-mercaptoethanol, which is a thiol reducing agent, and 2% (w/v) SDS, which is an anionic detergent. The treatment simultaneously breaks disulfide bonds and dissociates proteins into their constituent polypeptide subunits. SDS monomer binds to the polypeptides and causes denaturation. For most proteins, the binding ratio is approximately one SDS molecule per two amino acids [130]. Because of the anionic detergent, the charge densities are independent of pH in the range from 7 to 10 [130] and, most significantly, the SDS binding-polypeptides assume the same hydrodynamic shape [130, 131]. Glycerol is added to facilitate sample loading, while bromophenol blue facilitates both sample application and the electrophoretic run to be monitored (it migrates with the ion front). Complete dissociation of proteins is achieved by heating in SDS sample buffer samples to 99°C for 5 minutes.

Running the gels The procedure for running the gel is:

1. Assemble the electrophoresis apparatus and insert the gels.
2. Place the gel assembly in the lower-electrode buffer tank and completely immerse the gels in buffer.
3. Remove the combs from the gels and rinse the wells with running buffer.
4. Fill the upper reservoir of the electrophoresis cell so that running buffer fills the wells.
5. Load the protein standards and the samples in the wells of the gels. Sample volumes depend on the sample preparation and the size of the sample wells. Volumes loaded into the wells are normally of the order of tens of microliters.

6. Put the lid on the tank and connect the leads to the power supply. For most gel types, the anode (+) is indicated by the red lead, while the cathode (-) by the black lead.
7. Turn on the power supply and set it for the electrical conditions, i.e. 200 V constant voltage.
8. Allow the run to proceed until the blue tracking dye from the sample buffer reaches the end of the gel (about 30 min for Laemmli gels in the Bio-Rad minigels apparatus system).

Staining the gel The procedure for staining the gel is:

1. Remove SDS-PAGE gels from glass and rinse four times in dH_2O (every 15 minutes) in a suitable container on a rocking table.
2. Add enough Coomassie Stain to completely cover the gel.
3. Incubate the gel in the Coomassie stain for for at least 1 hour on a rocking table.
4. Pour off the Coomassie Stain.
5. Rinse in dH_2O until the background color of the gel is colourless.

2.2.5 Digestion of protein constituting the hard corona

Optimal conditions for free Bovine Serum Albumin (BSA) digestion by trypsin enzyme (SIGMA T-1426) have been identified in a previous work. Firstly, the enzyme-to-protein ratio was adjusted to the most favourable for digestion, maintaining the time of reaction constant. The digestion time was also explored by fixing the enzyme-to-protein ratio. The optimizal enzyme-to-protein ratio for the digestion of the free BSA was found to be 1:5 and the digestion time 1 hour. In this work the same conditions for the digestion of free and bound HS and HSA have been used.

Digestion of free proteins

The amount of the loaded reference proteins was 5 μg. For serum proteins an average mass value has been used according to the literature [128]. In general, detection requires on the order of 1 μg of protein for easy visualization of bands by coomassie staining . An excess of material is needed, since protein will be fragmented by trypsin. Stock solutions of 1 mg/ml Trypsin, HSA and HS have been prepared. Proteins were dissolved in water, while trypsin was dissolved in HCl 1 mM, pH 3, to prevent autolysis. Trypsin in 1 mM HCl (pH 3) solutions is stable for approximately one year when aliquoted and stored at -20°C. A fresh aliquots have been used for each experiment. The ideal operating conditions for sample digestion is at pH 7-9 at 37°C [132]. Thus, 50 mM ammonium bicarbonate (NH_4HCO_3), pH 8 was employed as operating buffer for the trypsin digestion. Ammonium bicarbonate was freshly prepared before each use. Samples were digested in a thermoblock at 37 °C for 1 hour. The digestion reaction was stopped by the addiction of 1 μL of HCl. The digested sample were visualized by SDS PAGE. For this purpose, SDS sample buffer 4× was added. SDS sample buffer contain bromophenol blue, which is a pH indicator. Acidic pH turn the SDS sample buffer yellow-coloured: 2 μL of Tris 1 M pH 8.8 were then added to adjust the pH conditions to the optimal operating pH. Samples were then boiled at 99°C for 5 min. Afterwards pockets of the gel were filled and the gel was run.

Digestion of the hard protein corona

Monodisperse citrate-stabilized gold NPs with a uniform quasi-spherical shape of $\sim$ 20 nm were conjugated to HS and to HSA following the protocol described in section 2.2.3. After 24 hours of incubation time the samples were centrifuged and resuspended three times (5000 $\times$ g for 10 min) in order to remove unbound proteins and the hard corona samples were obtained. The concentration of protein in the protein corona has been theoretically calculated assuming that just a monolayer of protein covering the NP and knowing the NPs final concentration and the dimension of NPs and proteins. For HS proteins an average molecular weight value has been used. The calculated number of attached protein molecules *per* NP is between 75 albumin/NP and 115 albumin/NP and between 66 serum proteins/NP and 101 serum proteins/NP. Considering an average value, the protein concentration in the hard corona is 0.03 µM, corresponding to 2 µg/ml protein concentration. Considering a loss of NPs-protein complexes during centrifugation corresponding to a 10% of the total and the excess of 5 µg used for the digestion of the free proteins, the protein corona samples were concentrated 5 times to obtain a comparable intensity band. Digestion of the protein corona was compared to the free protein digestion at the same enzyme to protein ratio and at the same digestion time (enzyme to protein ratio 1:5, T = 37°C, t = 1 hour).

2.3 Results and discussion

2.3.1 Hardening of the nanoparticle protein corona

Purification is crucial to study the hardening process of the protein corona since it is indispensable to remove the unbound excess of proteins. The black line in Figure 2.17 represent the SPR absorbance spectrum of the non-purified HS corona, while the purified HS corona spectra is represented by the red line, as example of the effect of purification. The peak at 280 nm in the non-purified sample is associated to the absorbance of excess of the free protein in solution.

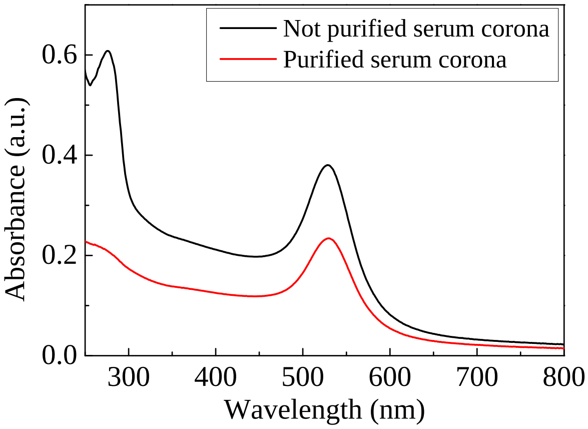

Figure 2.17: Purification effect on the the absorbance spectra of HS corona.

Furthermore, without purification the bioconjugates are not forced out the dynamic equilibrium between soft and hard corona. For this reason, measuring the properties of the non-purified sample could be misleading from the point of view of the hardening process: the evolution towards a more stable (hard) protein corona is masked due to the presence of the soft corona surrounding the NPs, which stabilize the colloids at any time. However, measuring the non-purified samples is useful to follow their evolution in terms of both corona: soft and hard, e.g.

monitor the aggregation state of the NP-protein complexes at different incubation time.

Hardening of the HS protein corona

In this subsection are reported the results of the incubation of 20 nm gold NPs with HS in PB 10 mM, pH 7.4.

An aliquote of the original sample is measured at variable incubation time and results are reported in Figure 2.18 a). The increase in absorbance intensity and the red shift of the SPR peak compared to the NP control (i.e. absorbance spectra of as synthesized NPs diluted in PB 10 mM) is observed as effect of the bioconjugation. Besides the change due to the conjugation and represented by the red-shift of the SPR peak position and by the little increase of the intensity in Figure 2.18 a), no time evolution of the SPR absorbance spectra has been observed.
Figure 2.18 b) shows the SPR absorbance spectra of the HS corona after 24 hours of incubation. The SPR peak shifts towards higher wavelength ($\Delta\lambda = 8.5$), while the intensity of the peak increase ($\Delta I = 0.14$).
Figure 2.18 c) shows the absorbance spectra of the HS corona samples purified at different incubation time. As it can be observed, the increase of the absorbance intensity and the red-shift of the SPR peak compared to the NP control (i.e. the absorbance spectra of the purified NP) is due to the bioconjugation. Despite the similarity on the final consequence for the SPR absorbance on both samples, the SPR absorbance of the non-purified samples follows a markedly different trend over time: at time 0 the SPR peak strongly red-shifts followed by a blue-shift of the SPR peak position. Meanwhile the intensity increases over time reaching a stable maximum value after 4 hours of incubation time. The strongly red-shift observed at time 0 is due to colloidal aggregation of the purified samples. This is consistent with the hardening process of the protective layer of proteins surrounding the NPs. As exposition time

gets longer, a layer of strongly adsorbed protein surrounding the NPs is formed, resulting in a stabilization of the NP surface. Figure 2.18 d) reports the absorbance spectra of the HS corona purified after 24 hours of incubation. The red shift of the SPR peak corresponds to 8 nm, while the increasing in intensity corresponds to 0.07.

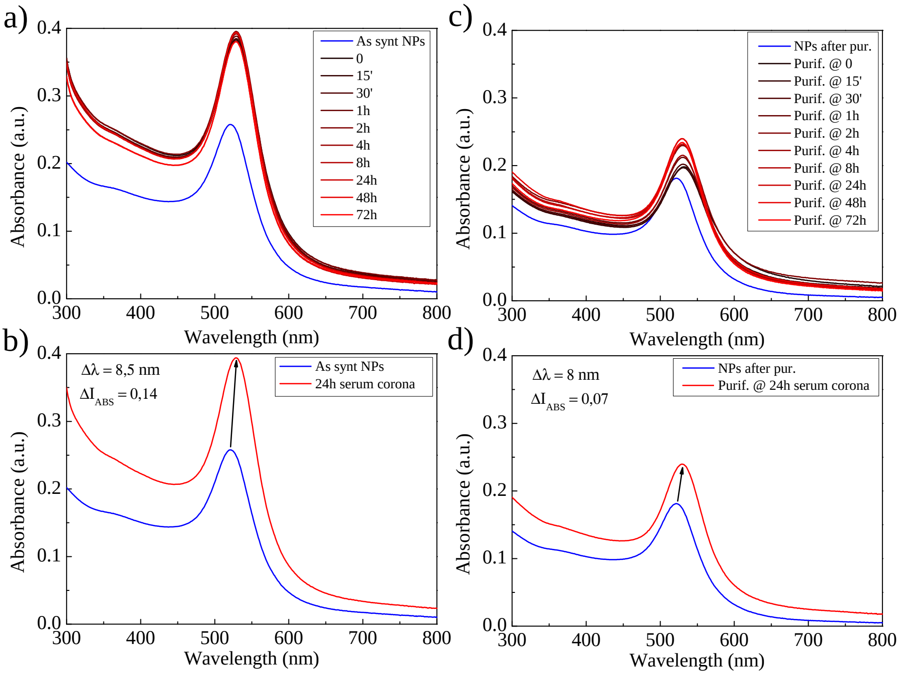

Figure 2.18: *Absorbance of the HS bioconjugated for all the measured samples.* a) absorbance spectra of the HS corona samples measured at different incubation time; b) absorbance spectra of the HS corona after 24 hours of incubation time ($\Delta\lambda = 8.5nm$, $\Delta I = 0.14$); c)absorbance spectra of the HS corona samples purified at different incubation time; d) absorbance spectra of the HS corona purified after 24 hours of incubation time ($\Delta\lambda = 8nm$, $\Delta I = 0.07$).

The time evolution of the SPR peak position (λ_{MAX}) reported in Figure 2.19 a) has been extrapolated from the data in Figure 2.18 a) for the non-purified sample and from Figure 2.18 c) for the purified samples. The evolution of the non-purified samples is represented by the red dots connected through the red line in Figure 2.19 a), while the black squares connected through the black line represents the evolution of the purified samples. The non-purified samples exhibit an initial red-shift of the SPR peak position with respect to the NP control. Successively, no further change in the peak position is measured, which means that no time evolution of the non-purified SPR peak position has been observed. On the opposite, the SPR peak position of the purified samples shows an evolution over time, which supports the observations associated to the absorbance spectra of the purified samples showed in Figure 2.18 c). For the purified samples, the SPR peak position reported in Figure 2.19 a) originally experience a large red-shift followed by blue-shift and stabilization. All the above results regarding NPs surface evolution highlight the importance of the time in protein corona formation: at initial time aggregation is observed, whereas, successively, the hardening of the protein corona stabilizes the NP surface.

Figure 2.19 b) reports the time evolution of the Z-Potential for the same non-purified samples (red dot connected through the red line) and purified samples (black square connected through the black line). The Z-potential of the non-purified samples is principally dominated by the free protein in solution. For this reason it remains stable at the HS reference value in PB 10 mM, which is $\backsim -20$ mV. The Z-potential of the purified samples shows an initial rapid decrease followed by a surface charge stabilization. The final value approach the HS reference value. After the 6^{th} hour, no significant changes have been measured.

The time evolution of the intensity of the SPR absorbance peak reported by the Figure 2.19 c) has been extrapolated from the data represented in Figure 2.18 a) for the non-purified sample and from Figure 2.18 c) for the purified samples. The gradual increase of the absorbance intensity with respect to the sample purified at time 0 has been observed. The intensity increases up to the 6^{th} hour, when it reaches his maximum value. This evolution over time also indicates the gradual stability acquisition of the colloids connected to the hardening of the protein layer on the surface of the NP and it is in agreement with the SPR and Z-Potential evolution (Figure 2.19 a) and 2.19 b)). The differences in the SPR intensity between the non-purified and the purified samples are attributed to material loss during the purification procedure. As previously discussed, purification conditions by centrifugation have been determined by the Stokes law, which allows the identification of the optimal centrifugation conditions that do not affect the material stability. This does not means that the yield on NPs collection is 100%, which results in a the general loss of absorbance intensity compared to the non-purified samples.

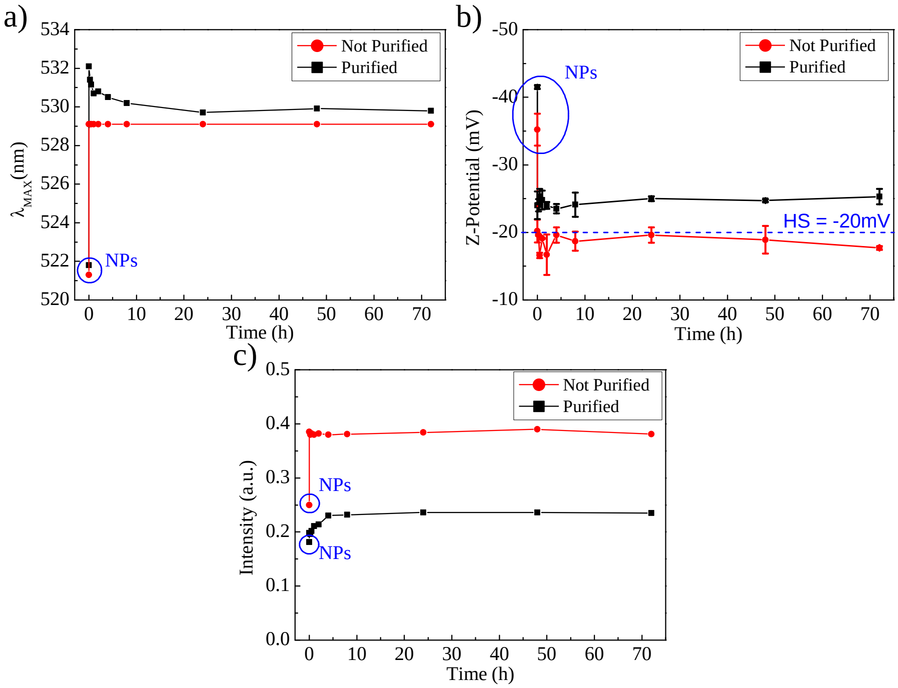

Figure 2.19: Time evolution of a) SPR peak position , b) Z-Potential and c) intensity of SPR peak for both purified and non-purified HS corona.

Figure 2.20 reports the measured DLS by intensity evolution of the non-purified and purified HS protein corona samples. The non-purified samples maintain their equilibrium and their monodispersity over time, while purified samples show the presence of multiple peaks in DLS spectra until the 8 hours of incubation time, confirming the aggregation due to the purification process.

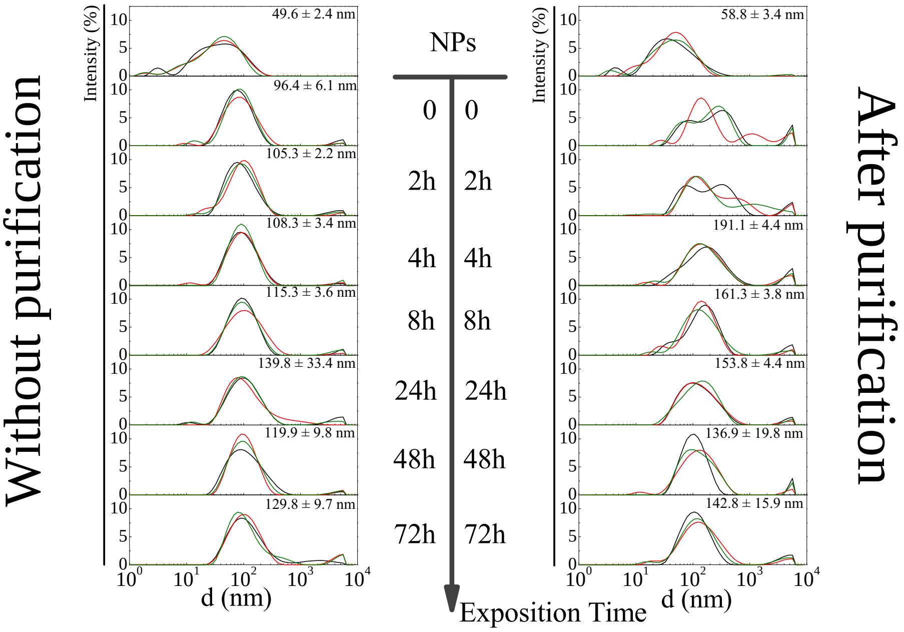

Figure 2.20: Time evolution of the intensity peak of the DLS for the non-purified and the purified HS corona.

Hardening of the HSA protein corona

In this subsection are reported the results of the incubation of 20 nm gold NPs with HSA in PB 10 mM, pH 7.4.

The SPR absorbance spectra of the HSA corona samples directly measured at different time without performing purification is reported in Figure 2.21 a). Once more, it can be observed the increases in absorbance intensity and the red-shift of the SPR peak compared to the NP control, as effect of the bioconjugation. Any subsequent changes has been observed and no time evolution of the SPR peak has been registered for the non-purified samples.
Figure 2.21 b) reports the absorbance spectra of the HSA corona after 24 hours of incubation. The SPR peak shifts towards higher wavelength of a value corresponding to 5.5 nm, i.e. red-shift of the SPR peak, while the SPR intensity increases of a value of 0.07.

Figure 2.21 c) shows the SPR absorbance spectra of the HSA corona samples purified at different incubation time. The decrease of the SPR intensity and the big red-shift of the SPR peak is a consequence of the NP aggregation. Thus, consistently with what observed for the HS corona samples, and contrary to the non-purified HSA corona samples, strong aggregation of the protein corona samples in the initial part of the kinetic is observed. Figure 2.21 d) reports the absorbance spectra of the HSA corona purified after 24 hours of incubation. The red-shift of the SPR peak is 8 nm, while the intensity increasing is of 0.07.

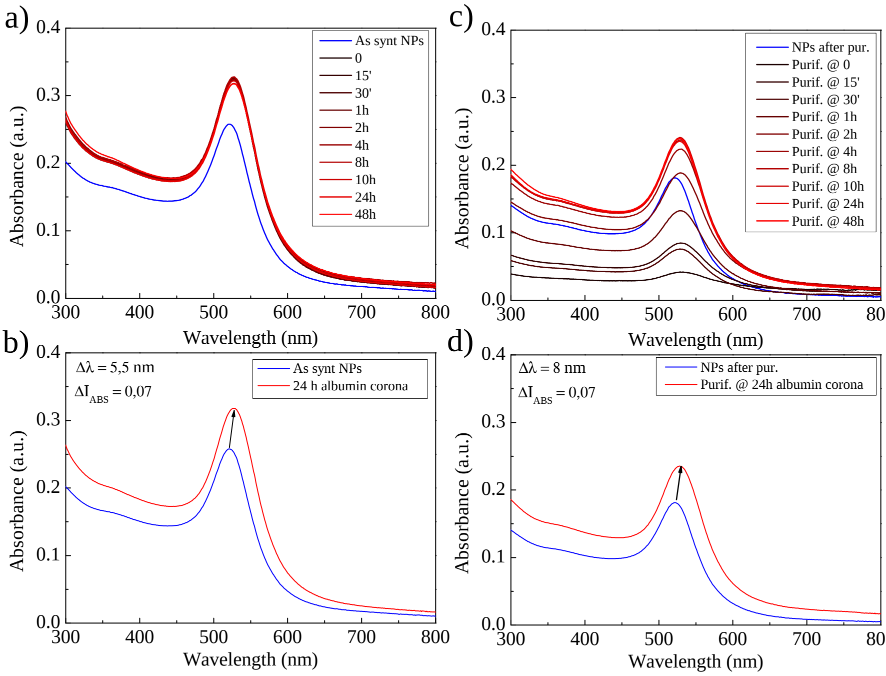

Figure 2.21: *Absorbance of the HSA bioconjugated for all the measured samples.* a) absorbance spectra of the HSA corona samples measured at different incubation time; b) absorbance spectra of the HSA corona after 24 hours of incubation time ($\Delta\lambda = 5.5nm$, $\Delta I = 0.07$); c)absorbance spectra of the HSA corona samples purified at different incubation time; d) absorbance spectra of the HS corona purified after 24 hours of incubation time ($\Delta\lambda = 8nm$, $\Delta I = 0.07$).

The time evolution of the SPR peak position (λ_{MAX}) reported in Figure 2.22 a) for the non-purified corona and for the purified corona are extrapolated from the data in Figure 2.21 a) and 2.21 c).

The evolution of the non-purified samples is represented by the red dots connected through the red line in Figure 2.22 a), while the black squares connected through the black line represent the trend of the purified samples. Analogously to the HS protein corona sample, the non-purified sample shows the red-shift of the SPR peak position with respect to NP control. Successively, no further changes have been detected, indicating that there is no evolution over time of the non-purified SPR. On the other hand, the SPR peak position of the purified samples reported in Figure 2.22 a) experience a large red-shift at time 0 followed by blue-shift and stabilization. As observed for the HS corona, after an initial stage where purification induce strong colloidal aggregation, these reaches stability over time.
In Figure 2.22 b) is reported the time evolution of the Z-Potential for the same samples. The Z-Potential of the non-purified HSA corona in the initial part of the kinetics remains constant at the HSA reference value in PB 10 mM ($\sim$10 mV). As incubation time gets longer, Z-Potential matches the value of the purified HSA corona. This observation suggests that, once formed, the hard corona governs the electrophoretic mobility of the collidal sample. Contrary, the time evolution of the Z-Potential for the same purified samples shows an initial exponential-like decreasing approaching the HSA reference value in PB 10 mM. After 8^{th} hour, the value remains constant until 48 hours of incubation time. The minimum value of Z-Potential has been measured after 10 hours of incubation time.

The time evolution of the intensity of the SPR absorbance peak is represented by the Figure 2.22 c). The decreases of the intensity with respect to the purified NP control is due to the strong sample aggregation induced by purification in the initial part of the kinetic. Successively, the intensity gradually increases as incubation time gets longer, reaching its maximum value after 8 hours of incubation time. This tendency

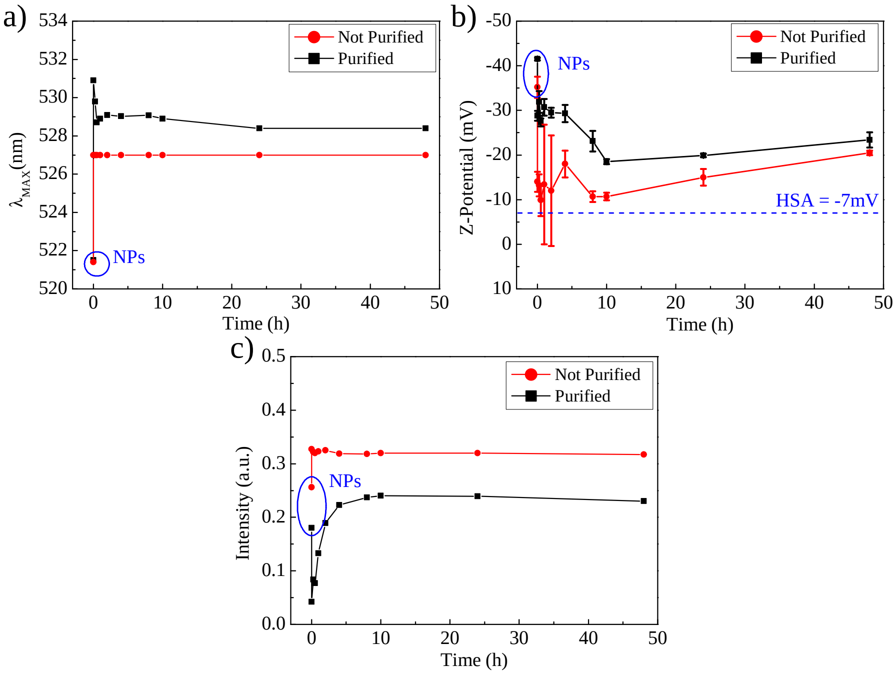

Figure 2.22: Time evolution of a) SPR peak position , b) Z-Potential and c) intensity of SPR peak for the purified and the non-purified HSA corona.

confirms the gradual stability acquisition over time (Figure 2.22 a)).

DLS by intensity measurements for both non-purified and purified samples at different incubation times is depicted in Figure 2.23. The non-purified samples maintains their equilibrium and their monodispersity over time. On the other hand, the purified samples reaches the stability after 8 hours of incubation time, consistently with the time stabilization effect due to protein adsorption.

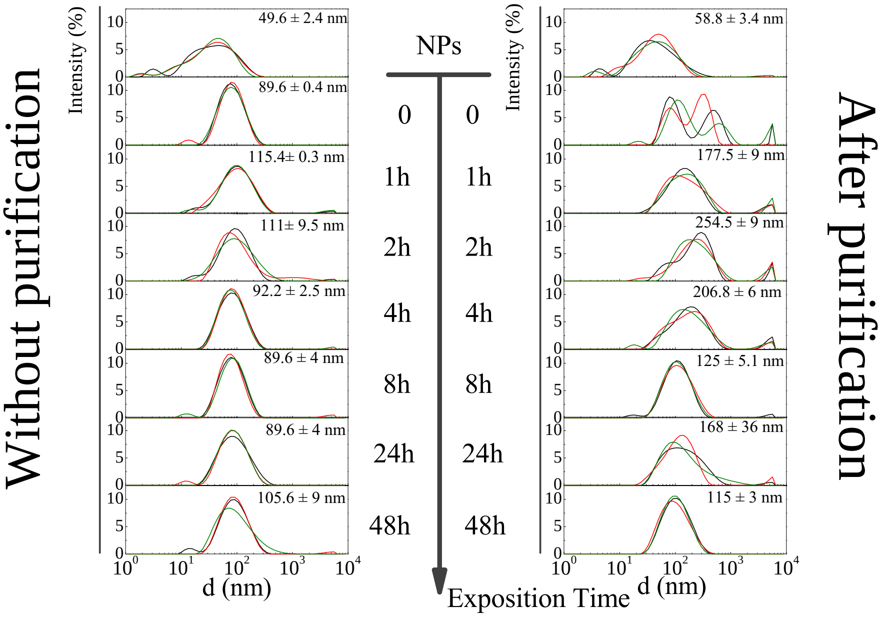

Figure 2.23: Time evolution of the intensity peak of the DLS for the non-purified and purified HSA corona.

Hardening of the IgG protein corona

In this subsection are reported the results of the incubation of 20 nm gold NPs with human IgG in PB 10 mM, pH 7.4.

Figure 2.24 summarizes the results of the incubation of 20 nm gold NPs with human IgG for all the measured samples: both the non-purified samples measured at different incubation time and those purified and measured at different incubation times.

The SPR absorbance spectra of the non-purified samples depicted in Figure 2.24 a) evolve towards an agglomerated state, as it can be observed by the red-shift of the SPR absorbance peak together with the diminution of its intensity (Figure 2.24 a)). Purification induces aggregation at all measured times (Figure 2.24 b)). This observation is confirmed by the DLS results reported in Figure 2.25 for both samples.

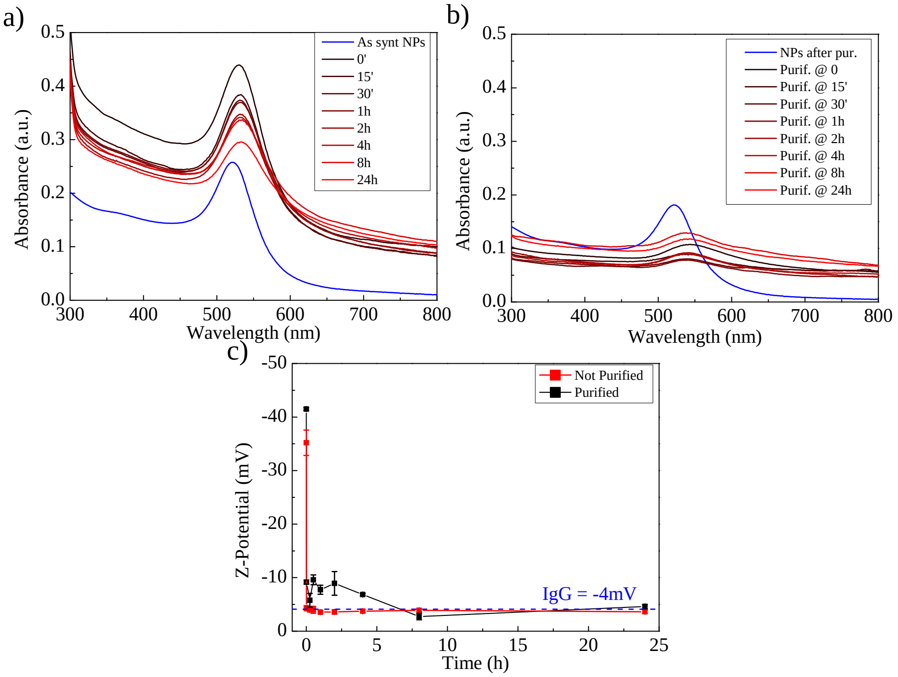

Figure 2.24: *Absorbance of the human IgG bioconjugated for all the measured samples.* a) absorbance spectra of the human IgG corona samples measured at different incubation time; b) absorbance spectra of the human IgG corona samples purified at different incubation time; c)time evolution of the Z-Potential for both the IgG corona.

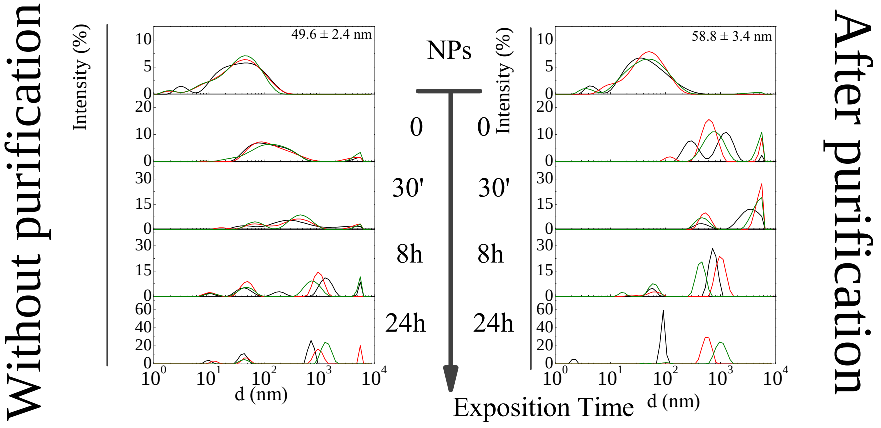

Figure 2.25: Time evolution of the intensity peak of the DLS for the non-purified and purified human IgG.

The trend of the non-purified samples indicates a temporal evolution of the colloids towards an agglomerated state, probably driven by the low IgG affinity for the NPs surface under this experimental conditions. The time evolution of the Z-Potential for all the IgG corona samples is reported in Figure 2.24 c). In this case, the Z-potential is not an useful parameter to evaluate the evolution of the protein corona due to the aggregation.

Discussion

The interaction between NPs and proteins in a physiological medium is immediate. Protein rapidly adsorbs onto the NP surface generating a new entity in which the NP surface properties are altered by the adsorbed protein. The incubation of NPs with HS proteins and HSA in PB 10 mM, pH 7.4, progressively evolve over time towards a stabilized colloidal state, i.e. hardening of the protein corona. Contrary, conjugation of NPs with human IgG lead to NP aggregation under the same experimental conditions. The stabilization effects by protein adsorption has been studied by aggregation-induced effect. This effect can be rationalize as represented in Figure 2.26.

Initially only a weakly bound layer of proteins (blue proteins) adsorb on the particle surface, stabilizing the colloids in the saline physiological medium but being in dynamic equilibrium with the unbound proteins in solution. These proteins form the so-called soft corona. As an effect of longer incubation time, the corona progressively stabilizes the surface through different mechanisms, including possible structural reorganization of adsorbed proteins, leading to a stronger attachment of proteins onto the particles surface (red proteins): hardening of the protein corona. Thus, when purified through centrifugation and re-suspension in protein-free media, protein-coated NPs display different colloidal stabilities depending on the duration of the incubation. After short incubation time,

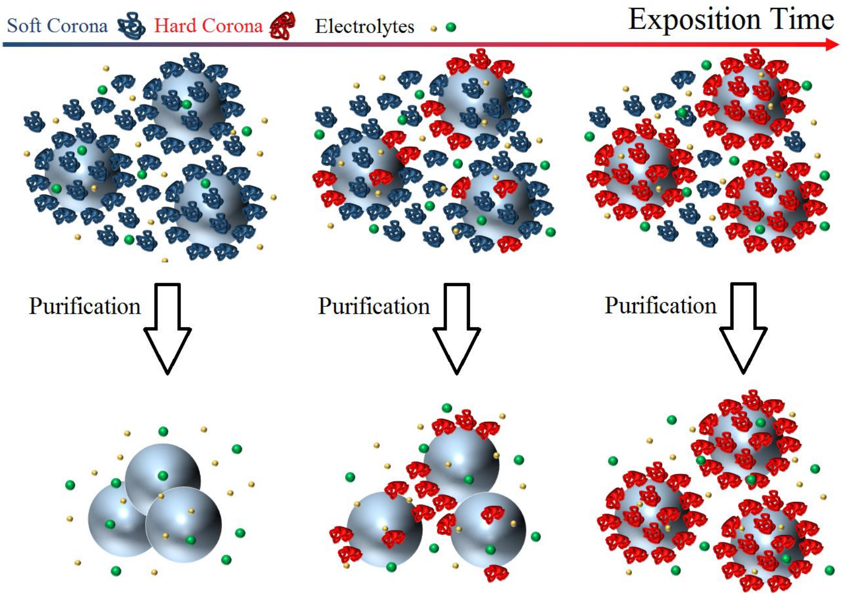

Figure 2.26: *Effect of centrifugation and re-suspension in protein-free medium.* After short incubation time, loosely bound proteins immediately detach from NP surface inducing irreversible NP aggregation in the saline physiological medium. After long incubation time, proteins rigidly bound to NP, protecting them from aggregation induced by centrifugation and re-suspension.

loosely bound proteins immediately detach from NP surfaces inducing irreversible NP aggregation in saline physiological medium. After long incubation time, proteins are stably bound to NP, protecting them from aggregation induced by centrifugation and re-suspension.

Figure 2.27 shows the results of the NP incubation with HS (black square connected by black line) and HSA (red dot connected by red line). IgG-conjugated NP aggregates under these experimental conditions.

Aggregation has been observed for all the analysed samples, depending on the incubation time. Incubation with IgG lead to NP aggregation, while HS corona and HSA corona samples aggregate only in the initial part of the kinetic. Aggregation is represented by the large red shift of

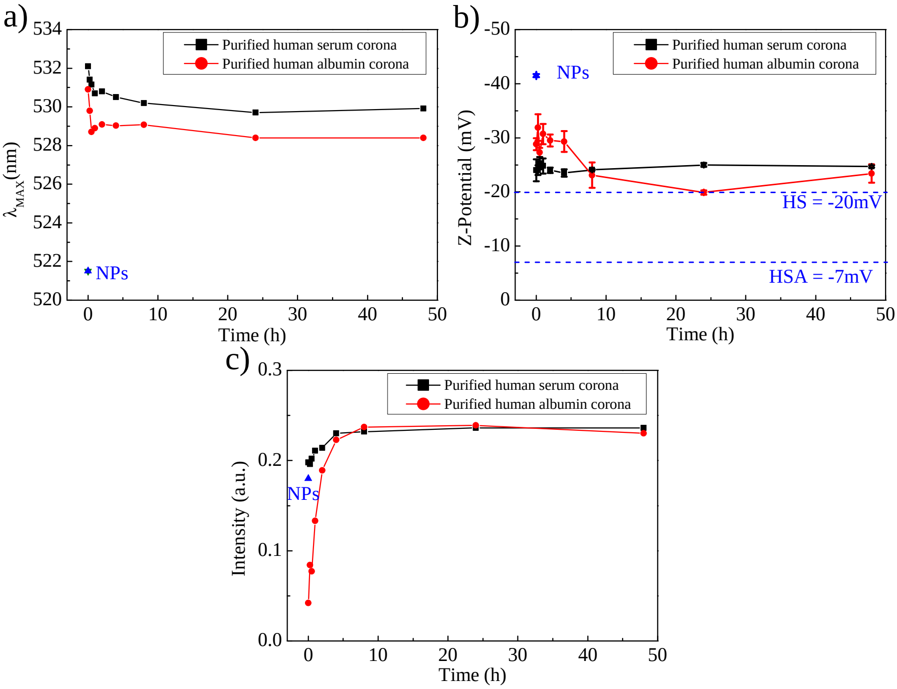

Figure 2.27: *Results of the NP conjugation with HS and HSA*. a) time evolution of the SPR peak position, b) time evolution of the Z-Potential, c) time evolution of the intensity of the SPR peak.

the SPR peak position reported in Figure 2.27 a) and by the decrease of the intensity reported in Figure 2.27 c) with respect to NPs control. As incubation time gets longer, the SPR peak blue-shifts and the SPR intensity increase. This observation is consistent with the formation of a protective layer of proteins surrounding the NPs which stabilized the NP surface. The Z-Potential of the bioconjugates approaches the characteristic protein value over time.

Figure 2.28 depict the time evolution of the hydrodynamic diameter measured by DLS for HS and HSA. As previously reported for SPR and Z-Potential, sample purification after short incubation time clearly induces aggregation (represented by the multitude of peaks in the measure). As incubation time gets longer, the DLS peaks evolve towards the rising of a single monodisperse peak. HS proteins stabilize the surface of NP in 8 hours, while HSA stabilizes the surface of NP in 4 hours.

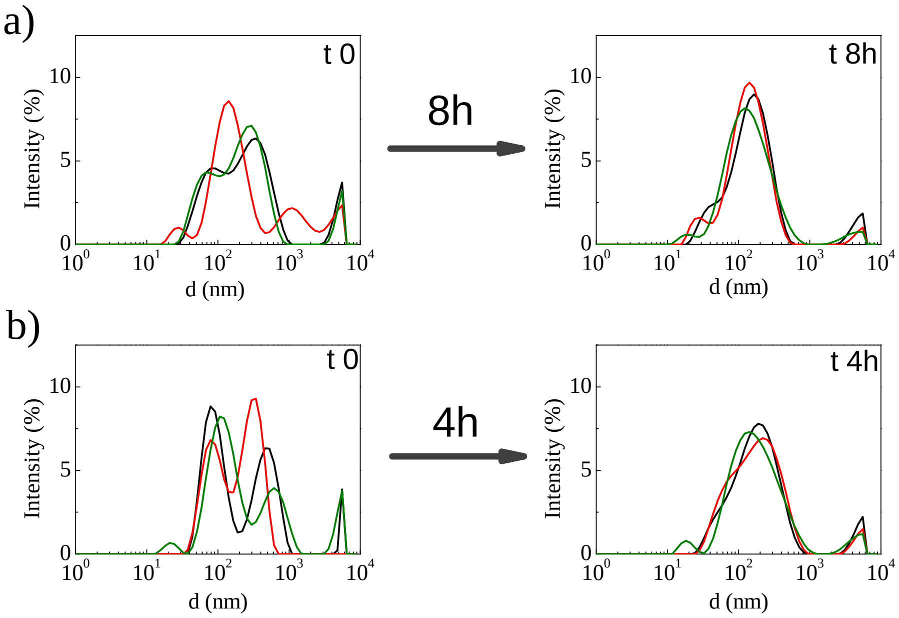

Figure 2.28: *DLS time evolution of the hydrodynamic diameter towards stability measured by intensity for a) HS and b) HSA.* Measurements have been performed in triplicate and each colour correspond to a single DLS measurement on the analysed sample.

For HS and HSA conjugated samples, the colloidal stability increases gradually with longer expositions to proteins, which becomes more and more tightly adsorbed onto NP surfaces and do not get lost with purification.

HS corona The SPR displays little aggregation between 0 and 2 hours, followed by a sample stabilization up to the 8^{th} hours. After 8 hours the absorbance intensity gets its maximum. The Z-Potential displays a decrease of the overall charge approaching the HS reference value in PB 10 mM. The hydrodynamic radius measured by DLS evolves towards a stability after 8^{th} hours.

HSA corona The SPR displays strong aggregation between 0 and 4 hours, followed by a little aggregation and a general sample stabilization until the 8^{th} hour. After 8 hours the absorbance intensity reach its maximum, as well. The Z-Potential displays a progressive decrease of the overall charge, which get to its equilibrium after 8 hours. The hydrodynamic radius measured by DLS evolves towards a stability after the 4^{th} hours.

IgG corona The SPR of the not purified samples displays an evolution towards an agglomerated state. Sample centrifugation and resuspension always leads to strong aggregation at every measured time.

All these observations are visually summarized in Figure 2.29.

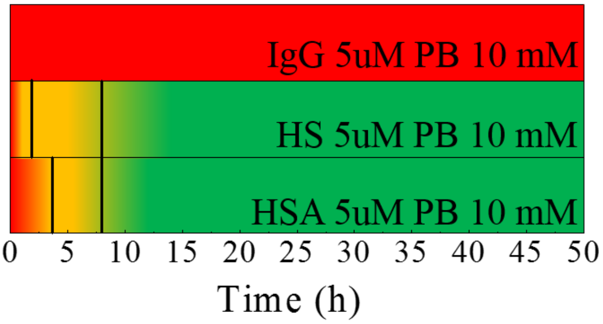

Figure 2.29: *Schematic representation of the kinetic of hard corona formation.* Purification of IgG samples always lead to agglomeration of the complexes: red-coloured part. Purification of HS corona and HSA corona lead to aggregation in the very first part of the kinetic: red-coloured part. Time stabilization effect of the NP surface associated to the protein adsorption, i.e. hardening of the protein corona, is represented by the red-to-yellow coloured part. Fully formed hard corona: green coloured part.

HS and HSA corona show different kinetic behaviour of the studied kinetic, i.e. the time evolution is different. Despite this difference in the evolution over time, the temporal pattern is similar for both corona, with an initial aggregation stage followed by stabilization. Contrary, IgG shows little affinity under this experimental conditions, leading to NP aggregation at every temporal point. From the 8th hour, the Z-potential of the resulting HS and HSA hard corona display the same value of -23 $\pm$ 2 mV. The SPR absorbance intensity of the resulting HS and HSA hard corona is analogous, while the SPR peak position values deviate by $\sim$ 1 nm. This is probably related to the presence of some different molecular compounds adsorbed on the NP surface.

Finally, the adsorption kinetic of HS protein on 20 nm NPs evokes the kinetic of HSA adsortpion under these experimental conditions, consistent with a final composition of the hard corona resulting from the NP incubation in HS rich in albumin. This is also supported by the similar SPR and DLS properties of the two hard corona.

Mass spectroscopy measurement after tryptic digestion of the HS-hard corona by MALDI-TOF is reported in Figure 2.30, confirming the presence of albumin inside the HS hard corona together with some trace of the heavy chain of the IgG.

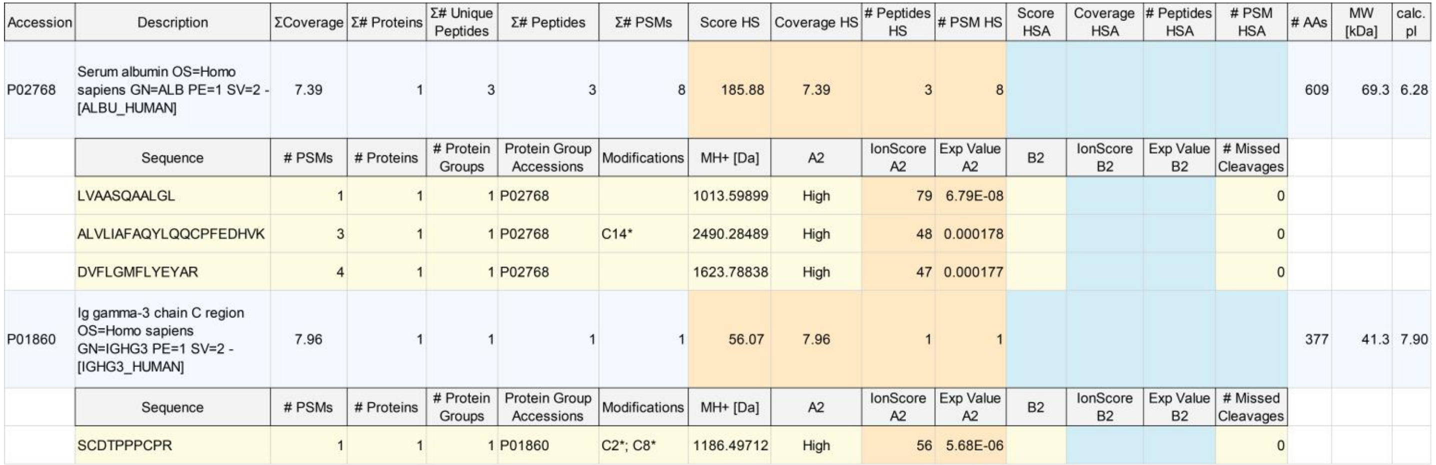

Accession	Description	ΣCoverage	Σ# Proteins	Σ# Unique Peptides	Σ# Peptides	Σ# PSMs	Score HS	Coverage HS	# Peptides HS	# PSM HS	Score HSA	Coverage HSA	# Peptides HSA	# PSM HSA	# AAs	MW [kDa]	calc. pI
P02768	Serum albumin OS=Homo sapiens GN=ALB PE=1 SV=2 - [ALBU_HUMAN]	7.39	1	3	3	8	185.88	7.39	3	8					609	69.3	6.28
	Sequence	# PSMs	# Proteins	# Protein Groups	Protein Group Accessions	Modifications	MH+ [Da]	A2	IonScore A2	Exp Value A2	B2	IonScore B2	Exp Value B2	# Missed Cleavages			
	LVAASQAALGL	1	1	1	P02768		1013.59899	High	79	6.79E-08				0			
	ALVLIAFAQYLQQCPFEDHVK	3	1	1	P02768	C14*	2490.28489	High	48	0.000178				0			
	DVFLGMFLYEYAR	4	1	1	P02768		1623.78838	High	47	0.000177				0			
P01860	Ig gamma-3 chain C region OS=Homo sapiens GN=IGHG3 PE=1 SV=2 - [IGHG3_HUMAN]	7.96	1	1	1	1	56.07	7.96	1	1					377	41.3	7.90
	Sequence	# PSMs	# Proteins	# Protein Groups	Protein Group Accessions	Modifications	MH+ [Da]	A2	IonScore A2	Exp Value A2	B2	IonScore B2	Exp Value B2	# Missed Cleavages			
	SCDTPPPCPR	1	1	1	P01860	C2*; C8*	1186.49712	High	56	5.68E-06				0			

*(Carbamidomethyl)

Figure 2.30: Mass spectroscopy measurement after tryptic digestion of the HS-hard corona by MALDI-TOF confirming the presence of albumin inside the HS hard corona together with some trace of a region of the IgG.

2.3.2 Altered digestion of proteins constituting the hard protein corona

Protein forming the hard corona can undergo induced structural changes that can affect their biological function [94]. Limited proteolysys is a simple biochemical method which provides information regarding the protein conformation in the adsorbed state [133, 134]. Trypsin is one of the most widely used serine proteases. The principle of limited proteolysys is that a protein, incubated with a relatively low concentration of enzyme, undergoes fragmentation at specific recognition sites throughout the polypeptide chain. Normally trypsin cleaves peptides on the C-terminal side of lysine and arginine amino acid residues at exposed regions [65, 135–140]. Thus, regions with enhanced flexibility and accessibility are more prone to digestion by trypsin than protected or static regions. After tryptic digestion, samples are analyzed by SDS PAGE to identify the cleavage products. The appearance of low molecular weight bands denotes digestion of the full length protein. The intensity and the appearance/disappearance of bands can be monitored and quantified [135]. Variables that can optimize the digestion effect are protease dilution, temperature and incubation time.

Here, tryptic digestion is used to monitor the flexibility and the accessibility of cleavage sites in the protein bound to the surface of NPs with respect to the free protein.

Thus, trypsin was employed to partially digest HS protein and HSA, both in solution and adsorbed onto gold NPs. The fragments were then visualized by SDS-PAGE. Polyacrylamide gels 16% were employed for the visualization of the product segments. Different protein segments after digestion with trypsin are expected depending on the residue availability on the NP surface, which can be related to the conformational state and accessibility of adsorbed proteins. Figure 2.31 schematizes the rationale of the tryptic digestion.

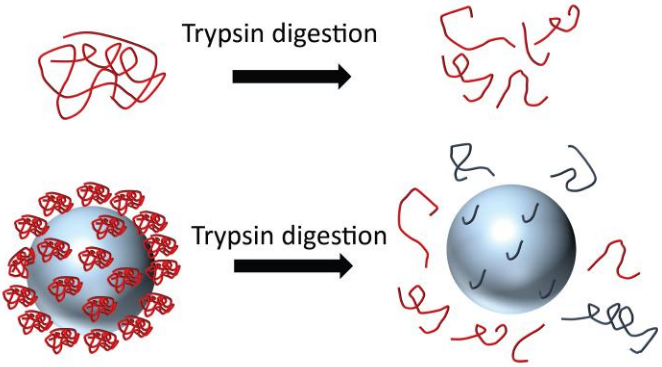

Figure 2.31: Schematic picture of the rationale of the protein metabolization of free proteins or hard corona proteins. Red protein: free protein generating digestion products; blue proteins: different fragment as a consequence of the digestion.

The digestion conditions used are:

- protein to trypsin ratio 1:5
- digestion time 1 hour 37°C

The hard corona samples were prepared as described in the subsection 2.2.3. After 24 hours of incubation time, the hard corona is fully formed. Figure 2.32 reports the properties of the hard corona samples. The formation of the hard corona is confirmed by the red-shift of the UV-Vis spectra of the purified bioconjugates and the decrease of the negative charge in the Z-Potential values from -41 mv $\pm$ 0.3 to -25 $\pm$ 0.4 for HS hard corona and from -41 mv $\pm$ 0.3 to -20 $\pm$ 0.4 for HSA hard corona (Figure 2.32).

The samples were washed before digestion by three centrifugation and resuspension cycles in 2.2 mM SC, pH 7.8. The effective removing of the protein excess has been investigated by loading the supernatant of each centrifugation step on a 16% polyacrilamide gel. Figure 2.33 reports the protein depletion of the supernatants as a result of the centrifugation and resuspension cycles for the HS hard corona (Figure 2.33 a)) and for the HSA hard corona (Figure 2.33 b)).

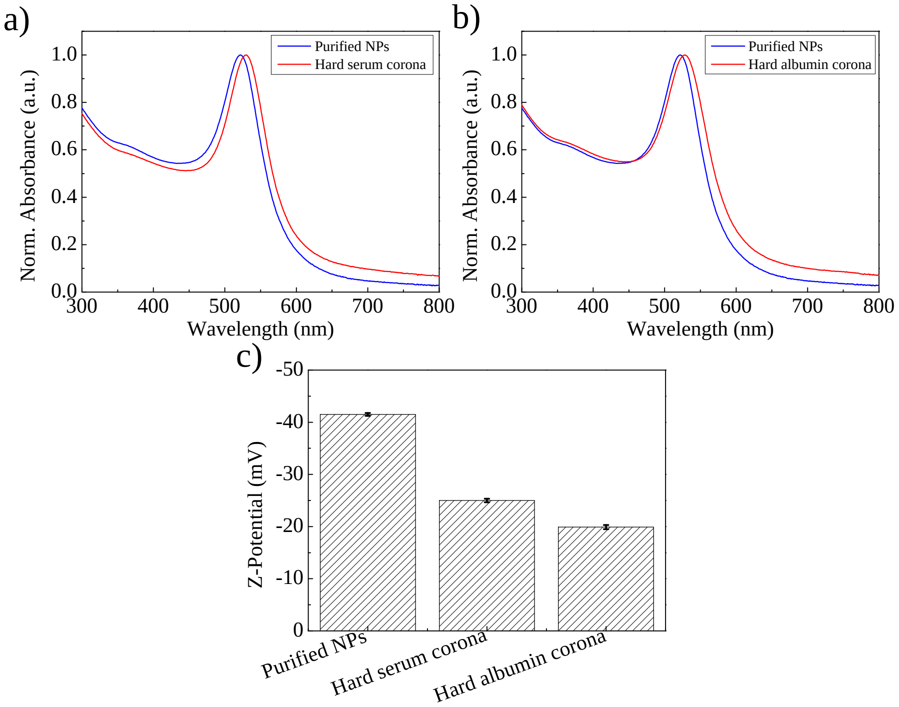

Figure 2.32: *Properties of the digested NP-hard corona.* a) Normalized SPR absorbance of HS hard corona b) Normalized SPR absorbance HSA hard corona. The blue line represents the purified NPs control. c) Z-Potential of the HS and HSA hard corona.

After the second centrifugation cycle, the supernatant can be considered protein-free and the hard corona completely washed (see lane 4 in Figure 2.33 a) and b)). Thus, the hard corona samples, together with the controls, were digested and the results are shown in Figure 2.34. In this experiment, the controls consisted in the digestion of the free proteins. Hard corona samples without undergoing tryptic digestion were also loaded in order to visualize the protein constituting the hard corona.

The loading order, as well as the sample preparation, is reported in table 2.5. The number in the first column corresponds to the number of the lane in Figure 2.34.

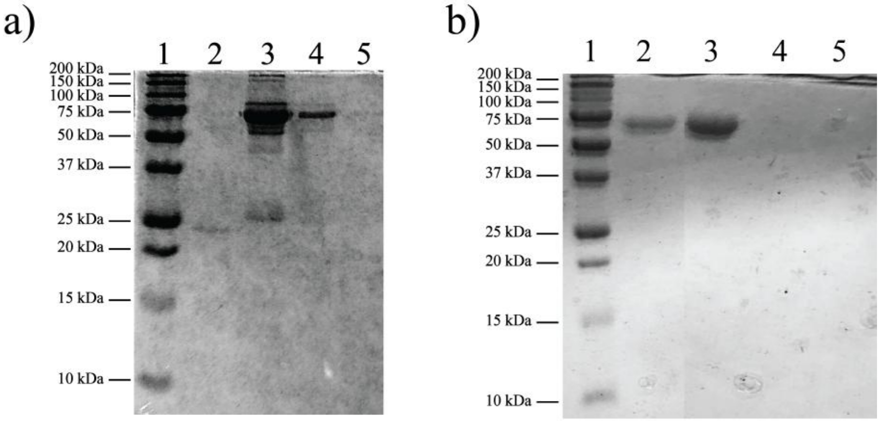

Figure 2.33: *Sample purification of the hard corona samples before the digestion protocol.* a) purification of the HS hard corona. Loading order: 1. Protein Marker; 2. Trypsin; 3. Supernatant of the first wash; 4. supernatant of the second wash; 5. supernatant of the third wash; b) purification of the HSA hard corona. Loading order: 1. Protein Marker; 2. HSA reference; 3. Supernatant of the first wash; 4. supernatant of the second wash; 5. supernatant of the third wash.

Lane 6 and lane 8 in Figure 2.34 confirm the presence of protein inside the hard corona for both samples.

A different pattern is observed between Lane 3 and Lane 7, which respectively correspond to the free HS protein digestion and to the digestion of the adsorbed HS protein, as well as between Lane 5 and Lane 9, which respectively correspond to the free HSA protein digestion and to the adsorbed HSA protein digestion.

The coloured bands in the lanes can be interpreted in terms of a gel densitometry, which represents the relative density of the contents of each lane. The profile plot of the lanes 3, 5, 7 and 9 have been obtained from Figure 2.34 and compared in Figure 2.35. From the profile plot, a different digestion pattern is clearly observed when comparing the free protein and the protein constituting the hard corona.

SAMPLE	$\mathbf{V}_{TOT}$ (**μL**)	$\mathbf{V}_{PROT}$ (**μL**)	$\mathbf{V}_{TRYP}$ (**μL**)	$\mathbf{V}_{AmBic}$ (**μL**)	$\mathbf{V}_{SDS}$ (**μL**)
1 Protein Marker					
2 Free HS protein	30	10	0	12.5	7.5
3 Digested free HS protein	30	10	1	11.5	7.5
4 Free HSA	30	5	0	17.5	7.5
5 Digested free HSA	30	5	1	16.5	7.5
6 HS hard corona	30	10	0	12.5	7.5
7 Digested HS hard corona	30	10	1	11.5	7.5
8 HSA hard corona	30	5	0	17.5	7.5
9 Digested HSA hard corona	30	5	1	16.5	7.5

Table 2.5: Loading order of the gel in Figure 2.34 and sample preparation for the digestion. The numbers in the column "Sample" correspond to the loading order.

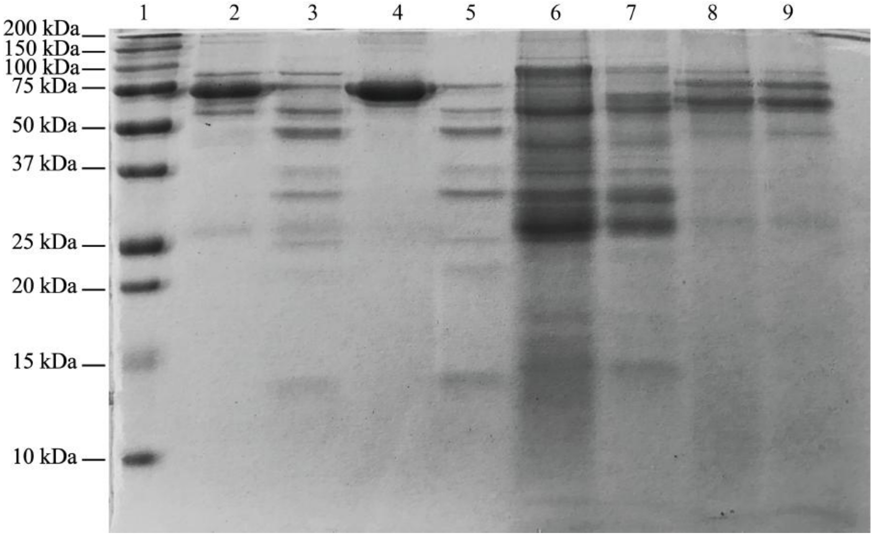
1
2
3
4
5
6
7
8
9
200 kDa
150 kDa
100 kDa
75 kDa
50 kDa
37 kDa
25 kDa
20 kDa
15 kDa
10 kDa

Figure 2.34: *Samples digestion and relative control*. Lane 1: protein marker; lane 2: free HS proteins; lane 3: digested free HS protein; lane 4: free HSA; lane 5: digested free HSA; lane 6: HS hard corona; lane 7: digested HS hard corona; lane 8: HSA hard corona; lane 9: digested HSA hard corona.

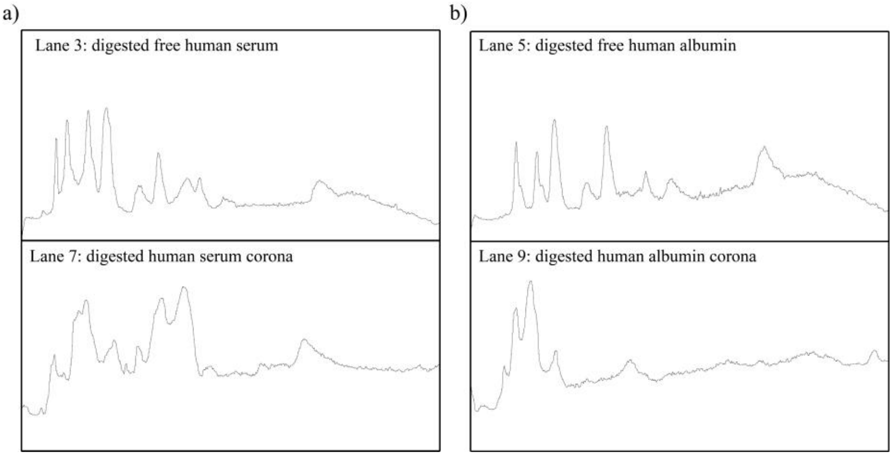

Figure 2.35: *Profile plot of digested sample*. a) profile plot of Lane 3 and 7 of the gel in Figure 2.34, b) profile plot of Lane 3 and 7 of the gel in Figure 2.34.

For HS samples, the main differences between the digested free HS protein (lane 3) and the digested adsorbed HS proteins (lane 7) are:

- presence of two new band between 50 kDa and 75 kDa in Lane 7 compared to lane 3;
- lack of 50 kDa band and presence of 45 kDa band in Lane 7 compared to lane 3;
- different band intensities between 25 and 37 kDa ion lane 7 compared to lane 3;

For HSA samples, the main differences are:

- absence of low molecular weight band between 10 kDa and 25 kDa in Lane 9 compared to lane 5;

The experimental results indicate that protein digestion generate different patterns depending on the state of protein (free or adsorbed on gold NPs).
For the HSA, the free protein is more prone to digestion by trypsin with respect to the adsorbed HSA. This can be related to a decrease of exposed regions to trypsin digestion of albumin inside the hard corona. Consequently, less fragments are generated after trypsinization of adsorbed HSA with respect to its corresponding free proteins. An altered digestion pattern has been also observed for the adsorbed HS proteins with respect to free HS proteins. The increase of the intensity of the low molecular weight band, in the region between 25 and 47 kDa, indicates that digestion events can occur, resulting in a generation of more fragments and low molecular weight bands with respect to the digested free proteins.

Concluding, protein metabolization is extremely connected to the state of the proteins: proteins in free state and protein in adsorbed state generate different digestion patterns. For HSA the adsorbed state can be described as a more static conformation with respect to the free state. In the adsorbed conformation some residues of the protein are less exposed resulting in a general protection of the protein under digestion. The adsorbed state of HS proteins is more accessible to digestion compared to the HSA in the adsorbed state. This can be related to the presence of some different molecular compounds adsorbed on the NPs surface with respect to the HSA hard corona, which exhibit different behaviour when exposed to tryptic digestion.

2.3.3 Parameters affecting the hard corona formation

Many parameters such as NP size, shape, curvature, solubility, surface properties, buffer composition and incubation time affect the stability, composition, thickness, and conformation of the protein corona [19, 41, 81, 141]. Importantly, Maiorano et al. [18] studied the interactions between commonly used cell culture media and differently sized citrate-stabilized gold NPs by different spectroscopic techniques (including DLS and UV-Vis). They studied the influence of the media composition on the formation of NP-protein conjugates. They demonstrated that the interactions are differently mediated by Dulbecco's Modified Eagle Medium (DMEM) and by Roswell Park Memorial Institute medium (RPMI) supplemented with the protein source from Fetal bovine serum (FBS). DMEM and RPMI are exploited for most cell cultures and strongly vary in amino acid, glucose, and salt composition. A range of spectroscopic, electrophoretic, and microscopic techniques were applied in order to characterize the colloids formed by dispersing NPs with different size in these cellular culture media. They reported the formation of a large time-dependent protein corona in DMEM and RPMI with different coating dynamics. SDS-PAGE and MS have revealed that the average composition of protein corona does not reflect the relative abundance of serum proteins. They also found that DMEM induced a more abundant and quite stable protein corona on different sizes of gold NPs compared to RPMI. Understanding the different formation of NP-proteins complexes mediated by liquid environment is crucial to reach a deeper understand of the cellular response [18].

In this section, the results of the investigation of some experimental parameters on the kinetic of hard corona formation are reported. Better understanding of the role of each parameter is of major importance for the design of targeting nanomaterials, long-circulating drug carriers, or for decreasing the toxicity. Specifically, the kinetics of the protein corona formation by changing the temperature and stirring conditions together with the effect of the presence of impurity in the protein preparation and the effect of the buffer composition, is investigated.

The bioconjugates were obtained as illustrated in subsection 2.2.3.

Temperature effect

The time evolution of the 20 nm conjugated NPs with HSA at different temperature in 10 mM PB, pH 7.4, is reported. Specifically, the tested temperature condition for the conjugation are 4°C and and 25°C (Room Temperature RT). Figure 2.36 and Figure 2.37 report the results of the conjugation at different temperature. Data represented in Figure 2.37 a) are extrapolated from data represented in Figure 2.36 a) and b).

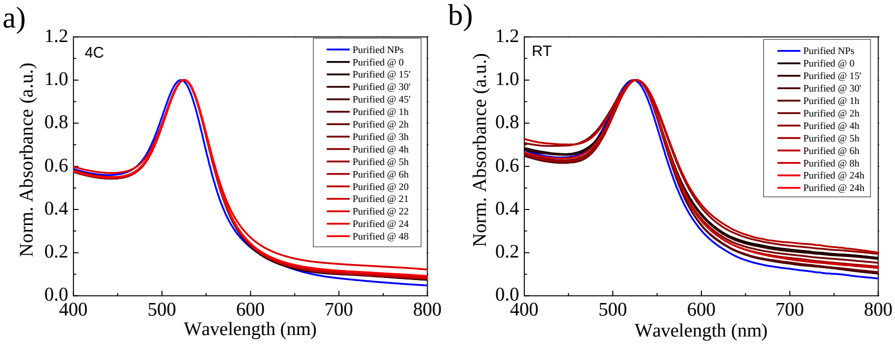

Figure 2.36: Absorbance spectra of the purified sample at different incubation time for: a) 4°C, b) RT.

When NPs are incubated at 4°C, their correspondent SPR (Figure 2.37 a)) shows an immediate 4 nm red shift, while, no time evolution of the SPR peak position has been measured. The Z-Potential (Figure 2.37 b)) decreases over time, approaching the HSA reference value. The average hydrodynamic radius (Figure 2.37 c)) measured by DLS shows an initial aggregation, followed by a stabilization from 8 hours of incubation time.

The RT-conjugated samples represented in Figure 2.36 b) exhibit a marked time dependency, which is better showed by Figure 2.37. The SPR and the Z-Potential evolves with time (Figure 2.37 a) and b)). The hard corona is fully formed when the SPR peak position, the average hydrodynamic radius and the Z-Potential, stabilize with time. The average hydrodynamic radius (Figure 2.37 c) is constant after conjugation and no aggregation effect of the colloids is registered.

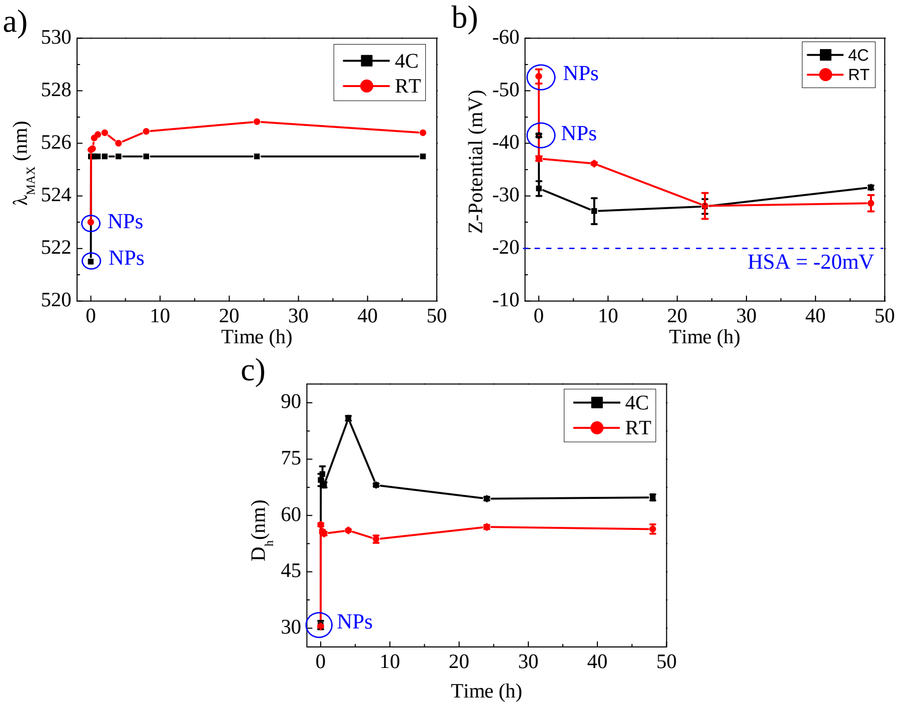

Figure 2.37: Effect of temperature on the formation kinetic of HSA corona: a) time evolution of the SPR peak, b) time evolution of the Z-Potential, c) time evolution of the hydrodynamic radius.

Thus, the reported time needed for the hard corona to be completely formed is 24 hours and it is not temperature-dependent. The final hard coronas are characterized by a similar Z-Potential value: -31 mV for the 4°C-conjugated and -29 mV for RT-conjugated. The red shift is 4 nm for both samples, while the hydrodynamic radius is ∼60 nm for the RT-conjugated and ∼ 67 nm for the 4°C-conjugated. These observations suggest that temperature affect the kinetic of the hard corona formation, but not affect the resulting hard corona. Concluding, the physicochemical characteristic of the two hard corona conjugated at different temperature are comparable.

Stirring effect

The time evolution of the 20 nm conjugated NPs with HS (Sigma H-4522) was studied under stirring conditions and without stirring at RT in 10 mM, pH 7.4. Figure 2.38 and Figure 2.39 report the results of the conjugation at different stirring conditions. Data represented in Figure 2.39 a) are extrapolated from data reported in Figure 2.38 a) and b).

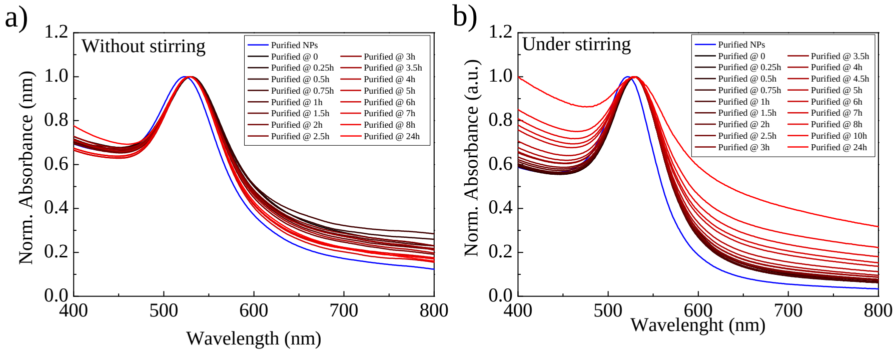

Figure 2.38: Absorbance spectra of the purified HS corona sample: a) conjugation without stirring, b) conjugation under stirring conditions.

As it can be observed in Figure 2.39 a), NPs get stabilize by protein adsorption: at short incubation times NPs exhibit a strong red-shift of the SPR peak which is followed by a blue-shift and a stabilization with time.

Z-Potential of the bioconjugates (Figure 2.39 b)) without stirring exponentially decay over time,reaching the HS reference value after 24 hours of incubation time. Z-Potential approximates to the HS reference value

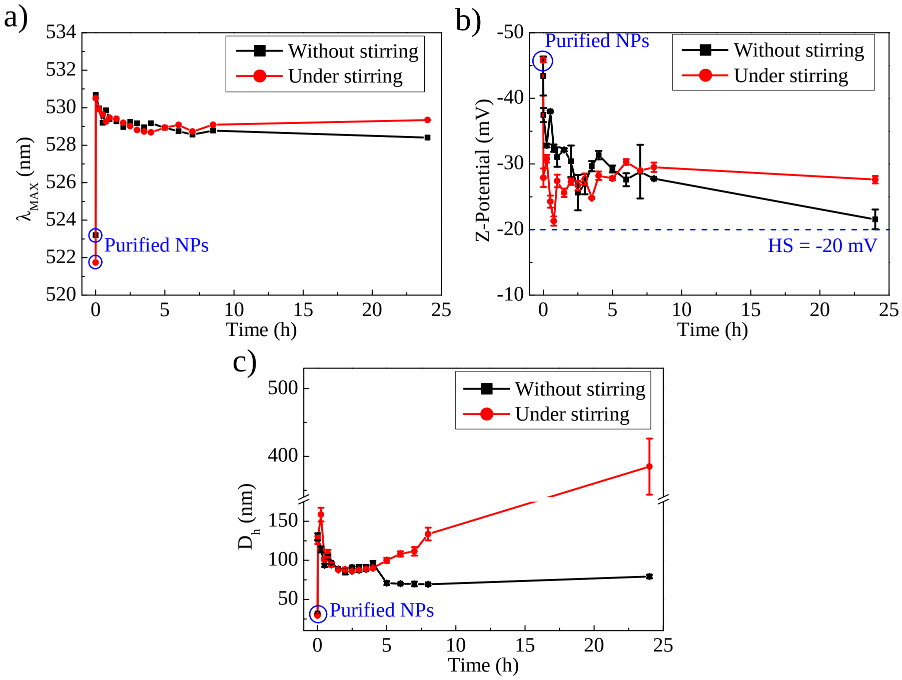

Figure 2.39: Effect of stirring conditions on the formation kinetic of HS corona: a) time evolution of the SPR peak, b) time evolution of the Z-Potential, c) time evolution of the hydrodynamic radius.

quicker when stirring is used in the incubation process compared to conjugated without stirring. In 2 hours it reaches the HS value.

The influence on the average hydrodynamic radius is reported in Figure 2.39 c). The under stirring-incubated samples show clear aggregation starting after 5 hours of incubation time. The hydrodynamic radius has an extremely high value after 24 hours of incubation time compared to the 24 hour-radius of the sample conjugated without stirring. The measure could be reasonably affected by the induced denaturation and aggregation of proteins due to the mechanical stress induced by the stirring conditions [142]. The protein destabilization drive NP aggregation, leading to an increase of the bioconjugates average hydrodynamic radii. Denaturation could influence also the charge of the conjugated, affecting the Z-Potential measurement. Therefore, stirring conditions induce strong protein destabilization, which clearly affect the kinetic of the protein corona and the resulting physicochemical properties of the hard corona.

Purity of the original protein preparation

It is reported the time evolution of the 20 nm conjugated NPs with HSA from two different suppliers characterized by a different purity degree, in 10 mM PB, pH 7.4, at RT, without stirring conditions. HSA from EMD Millipor (12668-10GM) is characterized by a degree of purity of > 95%, while HSA from Sigma Aldrich (A-9511) is characterized by a degree of purity of > 97%. When dissolved in a reference buffer, proteins with different purity levels might lead to a different buffer composition, due to the presence of some compound in different concentration in the original preparation. Since the nature of the buffer could affect the bioconjugation, the presence of these compounds, although in small quantity, could affect the formation of the protein corona. Data represented in Figure 2.41 a) are extrapolated from data represented in Figure 2.40 a) and b).

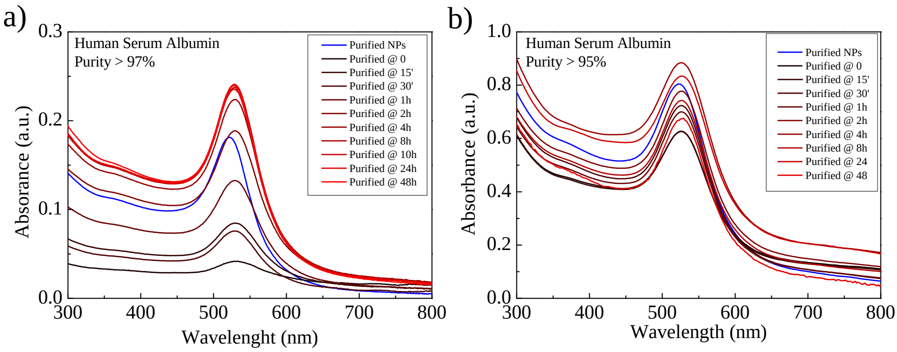

Figure 2.40: Absorbance spectra of the purified human albumin corona sample: a) conjugation with HSA from Sigma Aldrich (A-9511) with a degree of purity of > 97%, b) conjugation with HSA from EMD Millipor (12668-10GM) with a degree of purity of > 95%,.

The presence of the impurity on the conjugation influence the surface protection effect against aggregation induced by purification, as shown by Figure 2.40 and by Figure 2.41 a).

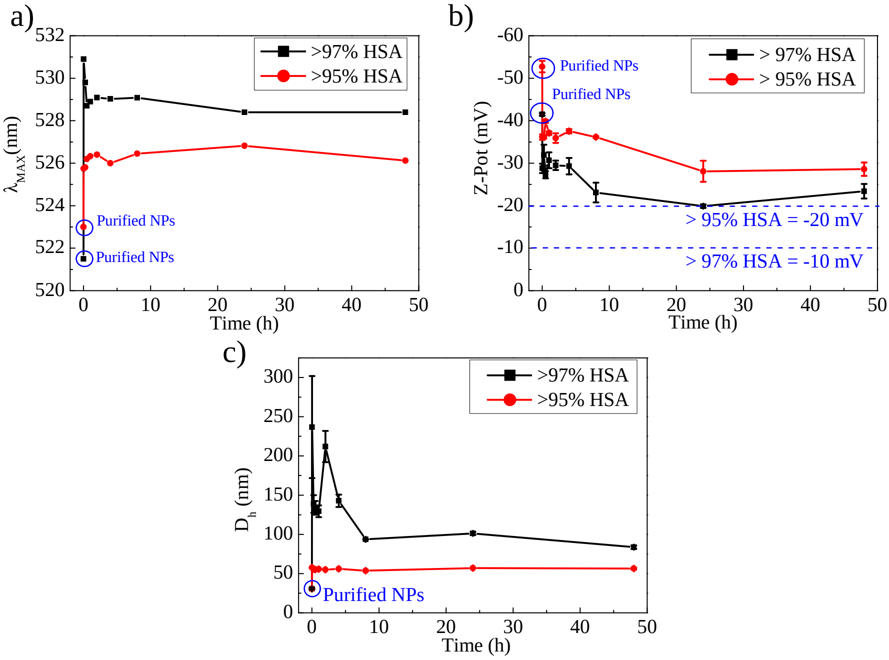

Figure 2.41: Effect of the presence of impurity on formation kinetic of the human albumin corona: a) time evolution of the SPR peak, b) time evolution of the Z-Potential, c) time evolution of the hydrodynamic radius.

The evolution of the SPR peak position of the more pure HSA indicates strong aggregation when purified after little incubation time. As it can be deduce by the red-shift of the adsorbed peak in Figure 2.40. The same conclusion is derived from Figure 2.41 a). However, at longer incubation times, the hardening of the protein corona stabilize the samples. Time evolution of the SPR peak position using the less pure protein exhibit an exponential-like increase in the first part of the kinetic followed by stabilization of the SPR peak position at ∼4 hours of incubation time. Instead, the Z-Potential (2.41 b)) exponentially decrease for both HSA protein corona approaching their correspondent free HSA reference value, which is different for the two different HSA. Z-potential is also affected by the purity degree of the protein. The evolution of the hydrodynamic radius reported in Figure 2.41 c) is consistent with the evolution of the SPR absorbance peak: at small incubation times purification induce aggregation, as it can be deduced by the high value of the average hydrodynamic radius. Stabilization of the NP surface takes place after 8 hours of incubation time.

Thus, the level of purity affect the kinetic of protein adsorption and the physicochemical characteristic of the resulting hard corona. The results shows that the presence of minor compounds protect the surface of the NP from aggregation induced by purification at small incubation times. The Z-Potential value for the two hard corona is comparable, and it is $\sim$ -25 mV $\pm$ 2 mV, while the SPR shift is different: 3 nm for the less pure albumin, 7 nm for the more pure one.

Chemical composition of the buffer

The time evolution of the 20 nm conjugated NPs with different protein, namely BSA, HSA, IgG and HS, dissolved in different media: 2.2 mM sodium citrate (SC), DMEM, PBS and PB 10 mM. The conditions and results are summarized in Table 2.6.

Protein	Buffer	Effect on the colloids
BSA	SC 2.2 mM	Protein corona formation
	DMEM	Aggregation
	PB 10 mM	Protein corona formation
HSA	SC 2.2 mM	Protein corona formation
	DMEM	Aggregation
	PB 10 mM	Protein corona formation
	PBS	Protein corona formation
HS	SC 2.2 mM	Aggregation/protein denaturation
	DMEM	Protein corona formation
	PB 10 mM	Protein corona formation
IgG	SC 2.2 mM	Aggregation
	DMEM	Protein corona formation
	PB 10 mM	Aggregation
	PBS	Aggrergation

Table 2.6: Effect of tested buffer on protein corona formation.

Bovine Serum Albumin Figure 2.42 reports the results of the conjugation of NPs with BSA in 2.2 mM SC, pH 7.8.

The SPR absorbance peak and the hydrodynamic radius reach the stability after 16 hours of incubation time. The Z-Potential (Figure 2.42 c)) needs almost 48 hours to reach the BSA reference value in SC 2.2 mM, which is ∽-20 mV ± 1.7 mV.

On the other hand, NPs incubated in a solution of BSA in DMEM 100% lead to colloids aggregation as it can be observed in Figure 2.43 a) by the intensity decrease together with the appearance the peak at ∽670 nm correlated to the appearance of a new NPs population. Z-Potential decrease with time, getting closer to the BSA reference value after 48

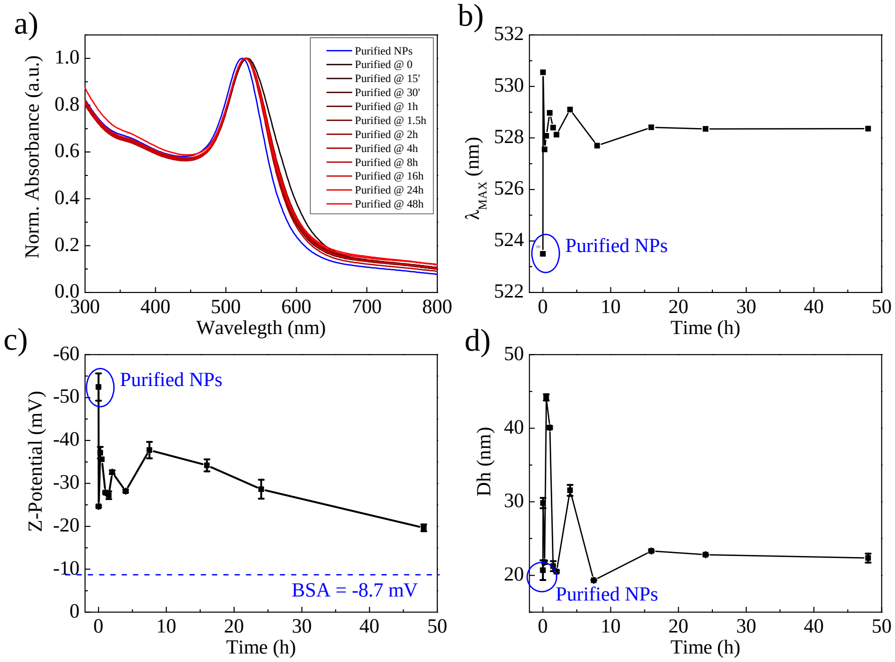

Figure 2.42: Conjugation of NP with BSA in SC 2.2 mM buffer: a) SPR absorbance spectra of the purified samples, b) time evolution of the SPR peak position, c) time evolution of the Z-Potential, d)time evolution of the hydrodynamic radius.

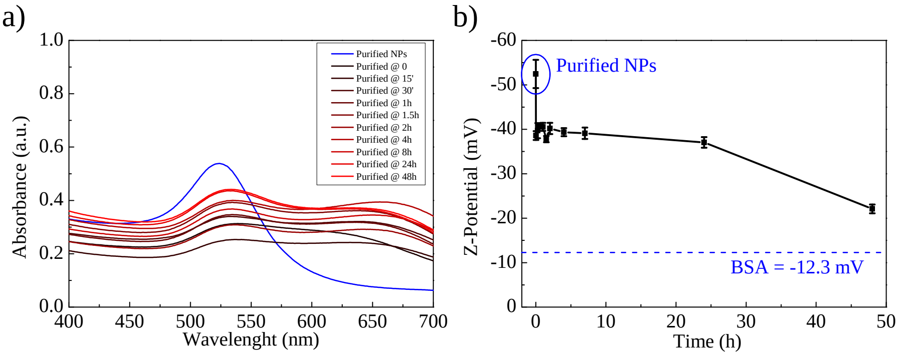

Figure 2.43: *Conjugation of NP with BSA in DMEM 100%.* a) absorbance spectra of the purified samples, b) time evolution of the Z-Potential.

hours of incubation time, although in this case the Z-Potential can not be considered as an indicator of the evolution of the protein corona due to the sample aggregation.

Human Serum NPs incubation in SC 2.2 mM supplemented by HS, leads to NP aggregation (Figure 2.44).

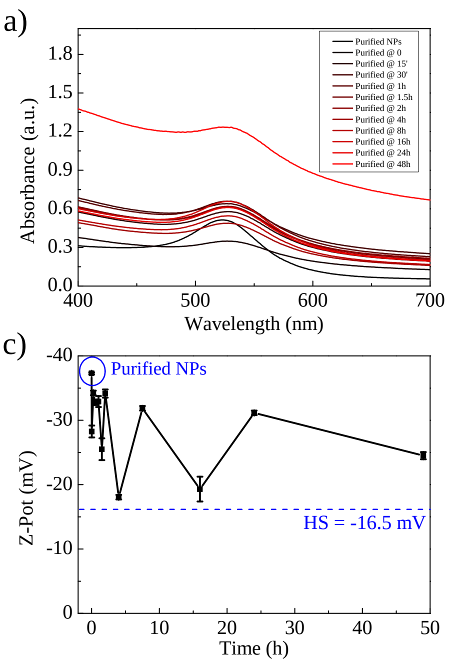

Figure 2.44: *NP incubation in SC 2.2 mM buffer supplemented by HS*. a) SPR absorbance spectra of the purified samples, b) time evolution of the SPR peak position, c) time evolution of the Z-Potential, d)time evolution of the hydrodynamic radius.

Using long incubation time , as it can be observed in the SPR absorbance spectra of the purified sample in Figure 2.44 a) by the decrease of the intensity of the peak and by the increasing of intensity at wavelength 700 nm. The hydrodynamic radius after 48 hours of incubation time highly increase due to aggregation and Z-Potential shows instability.

Figure 2.45 report the results of NPs incubation in DMEM 100% supplemented with HS. Under these experimental conditions it has been observed the quick formation of the HS hard corona. The SPR and the Z-Potential, reported in Figure 2.45 a), b) and c), reaches their stability after 8 hours of incubation. Starting from 24 hours no changes in the hydrodynamic radius have been measured (Figure 2.45 c)).

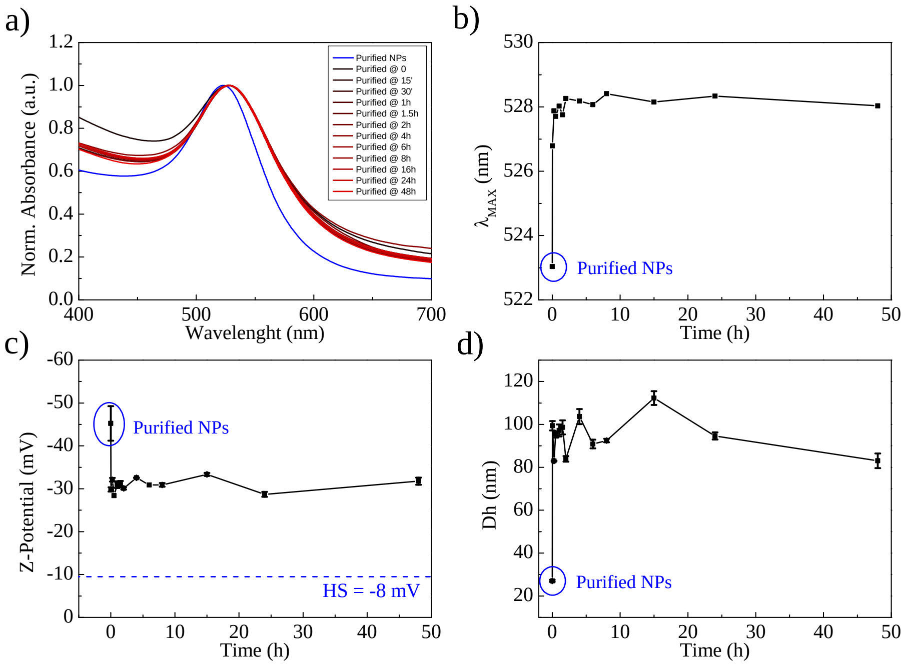

Figure 2.45: *NP incubation in DMEM 100% supplemented by HS*. a) SPR absorbance spectra of the purified samples, b) time evolution of the SPR peak position, c) time evolution of the Z-Potential, d)time evolution of the hydrodynamic radius.

Immunoglobulin G Time evolution of the IgG protein corona in PB 10 mM, pH 7.4 has been deeply investigated, and the results are reported in the subsection 2.3.1 and discussed in section 2.3.1. Here, it has been explored the NPs conjugation with IgG dispersed in DMEM 100%. Due to the increasing interest in the conjugation of gold NPs with antibody, for example in rapid diagnostic application [143–145], this part is described more in detail in the next section.

NP-IgG conjugation in 100% DMEM physiological media

IgG is an antibody isotype fundamental for immune system function [56]. In this context, IgG binds pathogens resulting in their immobilization, coats the pathogen surfaces (opsonization) allowing their recognition and phagocytosis, and binds and neutralizes toxins [56]. Despite its important role in the immune system and in many medical applications, IgG is still rarely used as a model protein in protein-NP interactions. Since IgG is the second most abundant protein in human blood plasma [90], a better understanding of the behaviour of the NP-IgG bioconjugated under physiological conditions is needed for understanding NPs fate when they are dispersed in HS. The protocol for the formation of the IgG corona is represented in Figure 2.46.

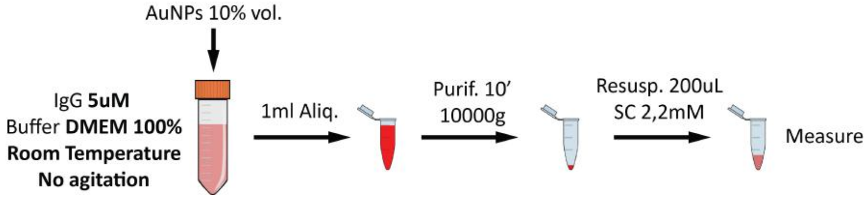

Figure 2.46: Protocol for the formation of the IgG corona in DMEM 100%.

The incubation was performed directly in 1 ml cuvette. Different cuvettes were prepared corresponding to different incubation times. The volume of NPs added to the protein solution has been kept constant and it is 10% of the total volume. The final NPs concentration is $\sim 3 \times 10^{11}$ NPs/ml, while the IgG concentration is 5 μ M, corresponding to 3×10^{15} prot/ml. The purification protocol consisted in the centrifugation of the sample at 10000×g during 10 minutes.

The results for the time evolution of the IgG conjugation are reported in Figure 2.47.

Figure 2.47 a) shows the normalized absorbance spectra of the IgG corona samples purified at different time, up to 1 week of incubation time. The red shift of the SPR peak compared to the NP control spectra is observed as effect of the bioconjugation. A stabilization effect of the SPR peak over time is observed: there is strong aggregation until 4 hours of incubation time, followed by a general sample stabilization. After 8 hours the SPR absorbance spectrum mainly recover his shape.

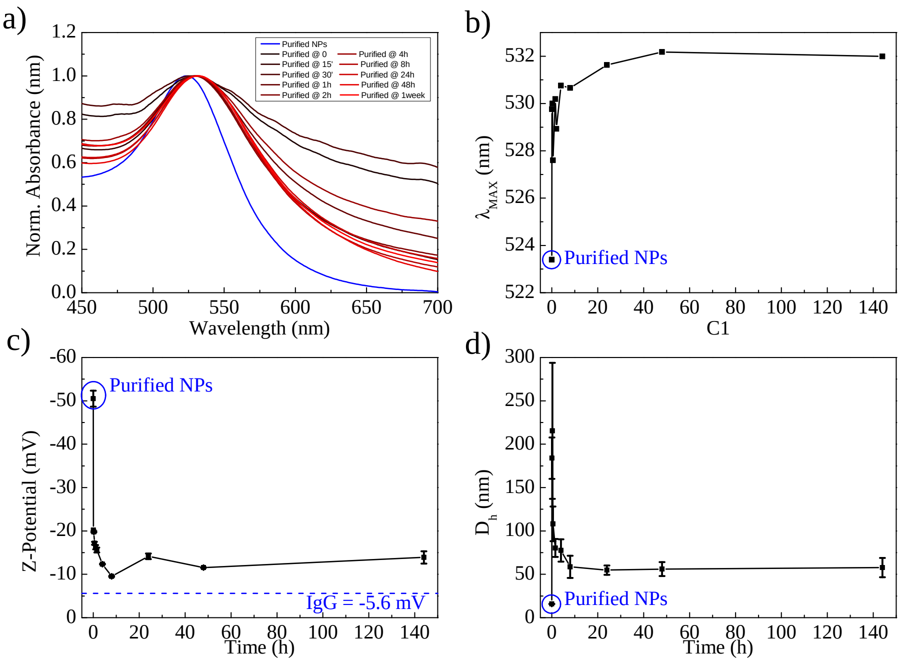

Figure 2.47: Conjugation of NP with Imunoglobulin G in DMEM buffer: a) absorbance spectra of the purified samples, b) time evolution of the SPR peak position, c) time evolution of the Z-Potential, d)time evolution of the average hydrodynamic radius.

Figure 2.47 b) shows the time evolution of the maximum of the SPR peak position extrapolated from the spectra in Figure 2.47 a), confirming similar considerations. After 24 hours of incubation time sample reach stability and the adsorbed protein stabilizes the NP surface protecting them from aggregation induced by purification. Figure 2.47 c) reports the time evolution of the Z-Potential for the same purified samples. After an initial exponential-like decreasing, Z-Potential reach its minimum value after 8 hours of incubation time. Between 8 and 24 hours Z-Potential oscillate between -11 mV and -14 mV, probably as an effect of stabilization of the surface charge. The Z-potential value after 48 hours of incubation time remain constant at -13 ± 1 mV . Figure 2.47 d) reports the time evolution of the average hydrodynamic diameter D_h. The strong aggregation at shots time is confirmed by the DLS measurements.

The sample gets stabilized after 8 hours of incubation time. Resuming:

- SPR: strong aggregation until 8 hours of incubation time, followed by a general sample stabilization up to the 24^{th} hour.
- Z-Potential: progressively decrease of the charge, which reaches its equilibrium between 8 and 48 hours.
- DLS: the average hydrodynamic diameter D_H shows aggregation of the samples followed by a sample equilibration after 8 hours of incubation time.

Figure 2.48 show the time evolution of the DLS by intensity.

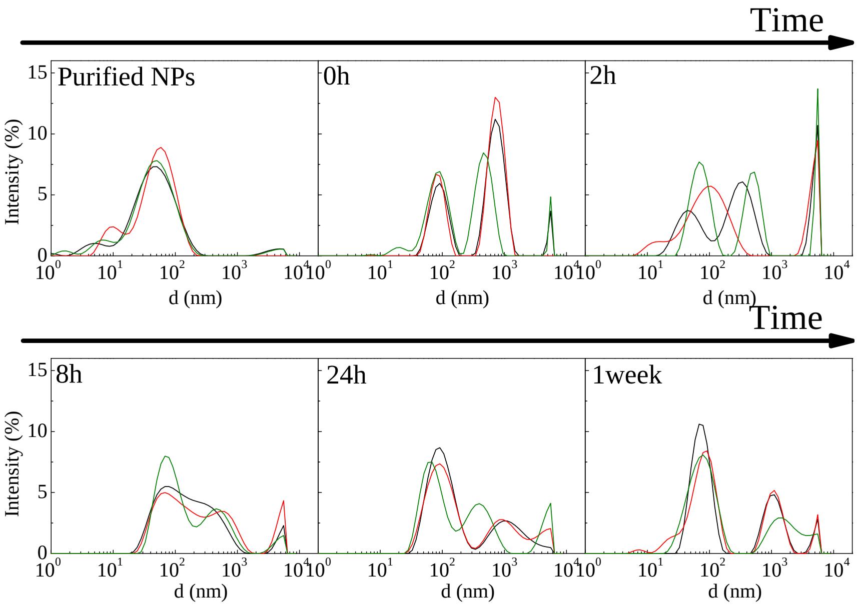

Figure 2.48: Time evolution of the DLS by intensity of the IgG-conjugated NPs.

Aggregation is observed at every purification time. Also when the shape of the SPR absorbance peak is mainly recovered, after 24 hours of incubation time, the DLS show the presence of a second polpulation ascribable to NP agglomerates. This is related to the lack of optimal conditions for obtaining monodisperse, colloidal IgG-conjugated NPs in complete physiological buffer.

Concluding, it is worth to note that, although the number of samples and replication are homogeneous for all the reported measurements, DLS and Z-Potential measurements, often return error bars which are different from point to point. This effect have been associated to the multiple sources of experimental errors which normally affect the measurements independently from how the operator handle the samples and operate trying to maintain their integrity. These errors are various and include the presence of micro-scratches on the optical surfaces or cell coating damage, small air bubble in the solution, temperature gradients, burned electrodes and contamination from previous samples. Thus, together with sample dispersity, which critically affect the measurement dispersion and, therefore, the error bars, some other operating and instrumental issue have to be considered as a source of experimental errors.

Chapter 3

Conformational properties of the hard corona

3.1 Introduction

As discussed in the general introduction, proteins absorb onto NPs surfaces, forming a layer of tightly attached molecules, the hard protein corona, and an external layer of weakly bound and rapidly exchanging molecules, the soft protein corona [81, 146]. From these interactions can arises structural rearrangement of protein forming the hard corona which can alter the subsequent protein biological responses in a physiological environment. Thus, the detection of these induced conformational changes is of paramount importance to understand the physiological fate and function of the nanoconjugates, as well as for designing new nanomedicine based technologies [63, 147–149].

The biophysical investigation of the hard protein corona structure at the nanoscale level is challenging due to the multiple factors affecting the interaction, comprising scattering, aggregation and interference with NP [94, 149], which might lead to a specific conformational changes driven by specific conjugation conditions.

Several procedures have been developed for the investigation of NP-protein bioconjugates by different biophysical techniques. For example, Norde and Favier [48], in a pioneering work, reported that BSA and lysozyme undergo structural alterations when adsorbed onto finely dispersed silica (SiO_2) particles, investigating protein structure by CD. Cinar and Czeslik [51] presented a study of pressure-and temperature-dependent unfolding of lysozyme and bovine ribonuclease A (RNase) using FTIR spectroscopy. They found that secondary structures of both proteins do not change significantly when they are adsorbed onto SiO_2 NPs. Vertegel et al. [147] showed that the structure and the function of lysozyme upon adsorption onto SiO_2 NPs is strongly dependent on the size, and hence curvature, of the NPs, evidencing that NPs with dimension of 4 nm and 20 nm retained native-like protein structure and function when compared to less curved, 100 nm NPs. The effects of the size of the SiO_2 NPs were further investigated by Lundqvist et al. [63]. They analysed the conformational stabilities of variants of human carbonic anhydrase on the surfaces of SiO_2 NPs, with different diameters (6, 9, and 15 nm). They monitored the structure of the adsorbed protein by CD and nuclear magnetic resonance (NMR) showing that NPs with a higher diameter cause larger perturbations on the proteins secondary structure upon interaction with NPs. In contrast, the effects on the tertiary structure seems to be independent of the particles curvature [63]. Gagner et al. demonstrated that the morphology and atomic structure of the surface of gold NPs affect the structure and function of adsorbed lysozyme and chymotrypsin (ChT) [72, 150]. Lysozyme lost respectively 10% and 15% of secondary structure when adsorbed onto 10 nm gold nanospheres or 36 nm gold nanorods. On the other hand, ChT retained most of its secondary structure at low surface coverage. A 40% loss in secondary structure and 86% loss of activity was observed. Wang et al. [151], using H/D exchange of amide protons monitored by NMR, reported the structural perturbations occurred upon adsorption on 15 nm gold NPs for GB3 protein and ubiquitin. They found that exchange rates are very similar in the presence and absence of NPs, supporting a model where the adsorbed protein remains largely folded on the NPs surface [151].

Summarizing, CD [152], FTIR spectroscopy [52], NMR [151, 153], H/D exchange coupled to NMR [151] or MS [154], SANS [155], UV-Vis [151], covalent footprinting [148], partial proteolysis [156] and dual polarization interferometry [157] have been applied so far to the structural investigation of standard globular proteins. The emerging picture is that folded, globular proteins tend to adsorb onto NPs in a native-like state, although some structural perturbations have been reported. In particular, conformational changes induced by interactions with NPs have been described for lysozyme [48, 147, 158–161], albumin [48, 65, 162], α-chymotrypsin [150], Apolipoproteins A-I and B100 [65], ubiquitin and GB3 [151], transferrin [41], carbonic anhydrase II [63], Myoglobin [154].

As a matter of fact, despite the progress on the investigation of structure of protein inside the hard corona, most studies focused on the behaviour of globular proteins, characterized by a high level of structural stability. A different interesting structural class is offered by intrinsically disordered proteins (IDPs) [163–167]. IDPs lack an ordered three-dimensional structure and exist in solution as heterogeneous and dynamic conformational ensembles [34]. They are often involved in the process of forming amyloid aggregates, which are the hallmark of systemic and neurodegenerative disorders, also known as amyloidoses [168]. In this context, the potential effect of the NPs surface is still almost unexplored. Parveen et al. [169] reported that NPs can induce or inhibit amyloid aggregation of IDPs, depending on the protein and surface properties. However, it is not clear if these effects are mediated by conformational changes or not. Other mechanisms arising from the protein-NPs interactions could involve changes in local protein concentration and/or competition between bulk and surface, resulting in eliciting amyloid aggregation

[166]. IDPs show the tendency to undergo disorder-to-order transitions upon binding to physiological partners and similar transitions can be induced by interactions with surfaces. Understanding the mechanisms controlling the conformational changes and the conformational stability of IDPs is of paramount importance in order to explain their biological activity.

One of the most intensively studied IDP, in its interactions with NPs is α-synuclein. Yang et al. [164] reported that the CD spectra of the free α-synuclein in solution and the synuclein adsorbed onto gold NPs are almost identical, suggesting that bioconjugation under those conditions does not affect the degree of structural disorder that characterizes α-synuclein in the absence of interactors. In addition, they determined by limited proteolysis experiment that α-synuclein binds to the surface of gold NPs via the N-terminus, while the C-terminus is projected outward from the NP surface, leaving the protein free to undergo conformational transitions [164, 165].

3.1.1 Goals and strategy

The goal of this study is to investigate the changes on the secondary structure of IDPs when adsorbed onto NPs surface. 50 nm SiO_2 NPs were employed. Three different IDPs, namely α-casein, $Sic1^{\Delta 214}$-His_6 and α-synuclein, were selected to investigate structural properties of IDPs forming the hard corona on SiO_2 NPs, together with lysozyme, as a model globular protein, which interactions with SiO_2 NPs are already well characterized [48, 73, 147, 148, 158, 160, 161, 170, 171]. Far-UV, CD and FTIR were applied to secondary-structure analysis of the free and surface-adsorbed proteins.

It is shown that IDPs constituting the hard corona are mainly unstructured, but exhibit a small protein-specific conformational change. A minor increases in helical content is observed for casein and α-synuclein.

This transition on α-synuclein is consistent with the IDPs tendency to undergo disorder-to-order transitions. The bound proteins are blocked in their largely disordered conformation and do not undergo folding induced by dehydration, in contrast to their free forms. Furthermore, the hydrodynamic diameter of lysozyme in solution approaches the thickness of the hard corona, while IDPs show a lower diameter comparing to their respective hydrodynamic diameter, suggesting a protein collapsed form. Finally, the tendency of α-synuclein aggregation in the presence of NPs was tested. The reported results showed that NPs promote α-synuclein aggregation in a concentration-dependent manner: the presence of increasing concentrations of NPs promoted aggregation.

Additionally, another set of experiment focuses on the conformational and spectroscopic properties of the globular protein transferrin (Tf) forming the hard corona on the same 50 nm SiO_2 NPs. Tf is an abundant serum metal-binding protein best known for its role in iron delivery [172]. The influence of these conformational rearrangements on the function of metal-bounding proteins has been investigated as a model of protein biological activity influenced by conformational changes induced by the interaction with NP surface. In a previous work it has been shown that terbium (Tb) can bind to Apo-Tf at the two iron-binding sites with lower affinity than iron [173]. The presence of Tb confers specific fluorescent emission properties detectable by fluorescence resonance energy transfer (FRET) with tryptophan residues.
All these features were studied by comparing the structural and spectroscopical properties of:

- Apo-Tf, the metal free protein
- Holo-Tf protein bound to iron
- Tb-Tf, protein bound to terbium instead of iron

It is shown that Tb-induced fluorescence properties are maintained inside the hard corona, while apo-Tf undergoes dramatic structural rearrangements upon binding.

Here, I would like to highlight that this part of the work has seen the essential contribution by the master student Valentina Rigamonti.

3.1.2 Scientific relevance of the selected materials

In this section, a brief general description of the selected materials and their biological importance is supplied for a better understanding of the following sections.

Silica NPs

Silica (SiO_2) is a versatile material, with a large potential for chemical and physical modifications and high level of biocompatibility [174]. Moreover, SiO_2 NPs exhibit good chemical and mechanical stability. They are characterized by negative surface charges and a relatively high hydrophilicity promoting protein–NP interactions mainly by electrostatic forces [174–176]. In this work, the Stober process [177] is used for the preparation of monodispersed SiO_2 colloids, by means of hydrolysis of alkyl silicates and subsequent condensation of silicic acid in alcoholic solutions using ammonia as catalyst [177] (Figure 3.1). The hydrolysis and condensation reactions provide precursor species and the necessary supersaturation for the formation of particles. Additionally, the size of silica NPs can be modulated by changing TEOS and ammonia relative concentrations.

Intrinsically disordered proteins

Intrinsically disordered proteins (IDPs) lack persistent structure. They are challenging to structural biology, due to the inapplicability of standard methods for characterization of folded proteins, as well as for their

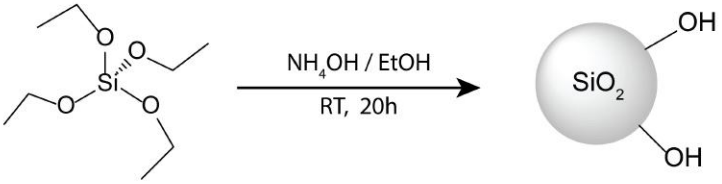

Figure 3.1: *Stober synthesis*. Mono-dispersed spherical silica NPs synthesized following the Stöber-Fink-Bohn method, starting from tetraethyl orthosilicate (TEOS), water, ammonia, and absolute ethanol, as precursor.

deviation from the dominant structure/function paradigm. IDPs exist in solution as heterogeneous and dynamic conformational ensembles [34]. IDPs are widespread in nature and they are importantly involved in a variety of biological function. Thanks to their high surface availability, IDPs show the tendency to quickly bind to interactors of different nature, assuming different conformational properties depending on the interactor. It has been shown that structural destabilization of IDPs leads to the formation of amyloid fibrils, which, in turn, are associated with a variety of neurodegenerative diseases, including Alzheimer's, Parkinson's and prion diseases [178, 179]. Amyloid fibrils are insoluble internal β structure fibers [180]. Amyloid formation has been rationalized as a nucleation-dependent polymerization process [181–192] consisting of two phases: (i) a nucleation/lag phase, in which the perturbations in the protein structure produce partially folded intermediates, with a high propensity to aggregate, and (ii) an elongation/growth phase, in which the nuclei grow by further addition of monomers to form larger polymers/fibrils. The kinetics of amyloid formation is well represented by a sigmoidal curve with a lag phase followed by rapid growth phase and a plateau (figure 3.2).

Understanding the mechanisms controlling conformational changes and conformational stability of IDPs is important to explain their biological and pathological activity.

The typical disorder-to-order transitions of these proteins upon binding

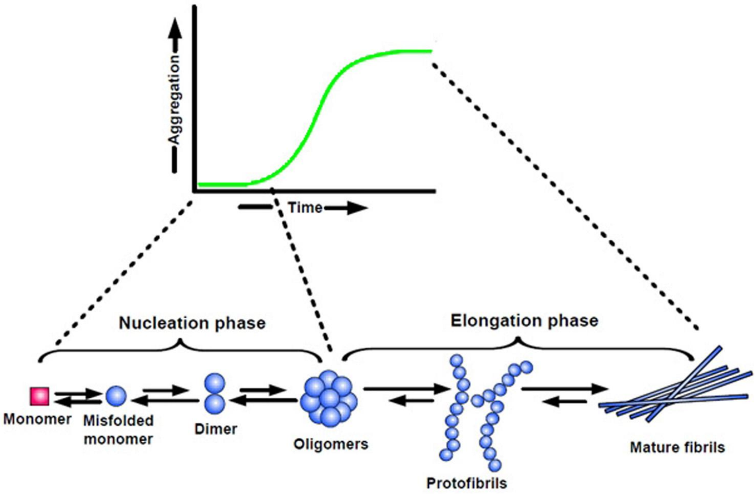

Figure 3.2: Schematic diagram showing the nucleation-dependent polymerization model of amyloid fibril formation [193].

to physiological partners can be induced by interactions with surfaces. Adsorption to NPs offers the possibility to investigate IDP interactions with surfaces in a colloidal state, exploring the structural effects of adsorption under specific conditions of solvent, surface chemistry and topology.

α-*synuclein*

α-synuclein is an IDP (14 kDa ,140 amino acids) characterized by an amphipathic lysine-rich amino terminus, which mediates the interactions with membranes, and a disordered, acidic carboxy-terminal tail, which has been implicated in interactions with metals, small molecules and proteins [194]. In this context, the interactions with NPs can mimic the effect on the natural interactor. After interaction with membranes, monomeric α-synuclein predominantly adopts an α-helical conformation, but at high concentrations the protein undergoes conformational changes, either before or together with its oligomerization, to form β-sheet-rich structures, which leads to the formation of intracellular inclusions called Lewy bodies [194–196]. It has been shown that the accumulation and redistribution of α-synuclein aggregates in specific brain regions is strictly connected to various synucleinopathies, including Parkinson's deseas (PD) and PD with dementia (PDD) [194]. In PD, the accumulation of these amyloid fibrils affect the regulation of dopamine release and transport, leading to the loss of dopaminergic neurons with the effect to reduce the neuronal responsiveness [195].

α-casein

The casein milk proteins have been described as natively unfolded with random-coil structure [197]. While their function is presumed to be primarily nutritional, increasing the solubility of calcium and phosphate, caseins also have a remarkable ability to stabilize proteins, i.e. to inhibit protein aggregation and precipitation, by an activity comparable to molecular chaperones [198]. α-casein (22.9 kDa, 214 amino acids) comprise two distinct gene products, designated α_{s1}- and α_{s2}- casein, which are unrelated in sequence but have very similar physicochemical properties. It has been shown that upon incubation at neutral pH and 37°C, the typical spherical particles of α_{s2}- casein rapidly converted to twisted, ribbon-like fibrils 12 nm in diameter, which occasionally formed loop structures (fibrils) [198]. Thus, α_{s2}-casein is particularly susceptible to fibril formation under physiological conditions. However, this fibril formation is mainly inhibited by α_{s1}- casein [198].

Sic1

In *Saccharomyces cerevisiae*, the IDP Sic1 is an inhibitor of the cyclin-dependent kinase (Cdk), which blocks the activity of S-Cdk1 (Cdk1 / Clb5,6), playing an essential regulatory role in cell cycle progression kinase essential for DNA replication. Sic1 dysfunction can affect the

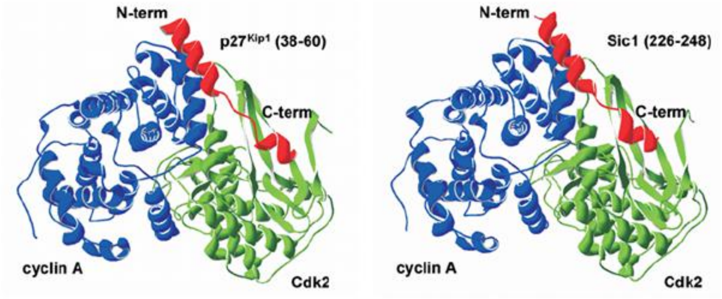

Figure 3.3: Structural prediction of p27 and Sic1. In red the inhibitory domain is indicated.

DNA replication, leading to an alterate cell growth and proliferation. Interestingly, Sic1 possess a human homologue, the protein p27Kip1, both having a structurally conserved inhibitory domain (figure 3.3) with the difference that p27Kip1 inhibits G1 cyclins and not cyclin B [199].

Sic1$^{\Delta 214}$-His$_6$ (9.3 kDa, 70 amino acids) corresponds to the last His tagged Kinase-Inhibitory Domain, which is the minimum domain for the inhibition of Clb5/6-Cdk1 [200, 201].

Globular proteins

Globular proteins, compared to IDPs, are characterized by ordered structure. Their conformation can accurately determine by crystallography, NMR or bioinformatics. Globular proteins are often used as model proteins and offer a reference for the investigation of NP-induced structural effects.

Lysozyme

Lysozyme (14.3 kDa, 129 amino acids) is an enzyme that posses primarily a bacteriolytic function by attacking the peptidoglycan bacterial cell walls. Peptidoglycan is composed of the repeating units of N-acetylglucosamine (NAG) and N-acetylmuramic acid (NAM), crosslinked by peptide bridges. Lysozyme acts by hydrolyzing the bond between NAG and NAM, increasing the bacteria's permeability eliminating the bacteria [202, 203]. In human, lysozyme is expressed in the mucous membranes of the nasal cavity and tear ducts. It is also found in saliva, tears, milk, cervical mucus, leukocytes, and kidney tissue. The majority of the lysozyme used in research is purified from hen egg white. Under physiological conditions, lysozyme is folded into a compact, globular structure (figure 3.4) with a long cleft involved in binding to the bacterial carbohydrate chain and hydrolysis.

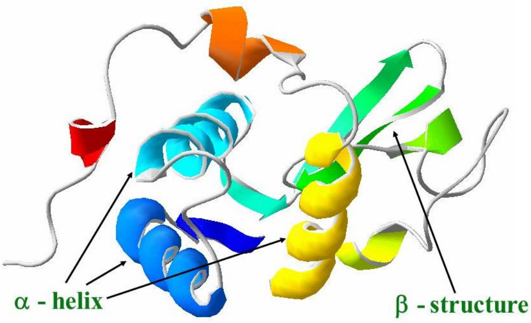

Figure 3.4: Lysozyme structural prediction.

Transferrin

Transferrin (Tf) is a powerful iron chelator, capable of binding iron tightly but reversibly [204]. A molecule of Tf can bind two atoms of ferric iron (Fe^{3+}) with high affinity (K_d = 10^{23} M^{-1}), which is higher in the extracellular pH of 7.4 and decreases in the acidified endosomes, allowing the dissociation of Fe [204, 205]. Serotransferrin belongs to a family of homologous iron-binding glycoproteins that encompasses lactoferrin (found both intracellularly and in secretions, including milk), melanotrasferrin (present on melanoma cells) and ovotransferrin (present in egg white). They are all monomeric proteins of 76–81 kDa and consist of two structurally similar lobes, namely N- and C-lobes, each containing one iron-binding site (figure 3.5) [206]. The N-lobe (336 amino acids) and C-lobe (343 amino acids) are linked by a short spacer sequence. Each lobe contains two domains (N1-N2 and C1-C2) comprising a series of α-helices, which overlay a central β-sheet [206] (Figure 3.5 a)). The domains interact to form a deep, hydrophilic metal-binding site. The binding sites posses four amino acids including two tyrosines, one aspartic acid and one histidine [173]. These residues are arranged in a distorted octahedral arrangement [173] (Figure 3.5 b)). In addition, the binding site requires two oxygen molecules donated by a carbonate molecule to stabilize the iron atom. The surrounding amino acid residues are thought to further stabilize the metal-binding site, and they have crucial roles in iron release [173].

X-ray studies revealed that in the apo form of Tf (apo-Tf, the iron-free form of Tf), the iron-binding cleft in the N lobe is wide open when compared to the closed holo-structure [206]. The resulting crystal structures shows that the two domains of each lobe are closed over a Fe^{3+} ion. Thus, upon uptake or removal of the iron ion, the domains rearrange their conformation, rotating as a rigid body around a rotation axis [173, 206]. The holo-Tf shows a much higher affinity for the transferrin receptor than the apo-form, suggesting that iron-dependent conformational arrangement is important for the cellular uptake of iron [173].

Protein function: focus on iron chelation Iron is important for all living organisms and plays a central role in many biological processes

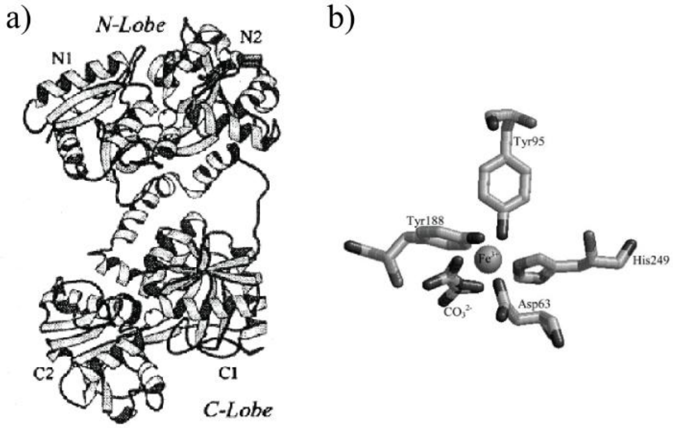

Figure 3.5: *Tf binding* Fe^{3+}. a) Stereo Cα plot of holo-ovotransferrin. N1 and N2 represent domains N1 and N2, while C1 and C2 domains C1 and C2 respectively. Wite balls are Fe^{3+}. The figure was produced using cristallographic data [206]. b) For Fe^{3+} the co-ordination sites are octahedral, with four ligands supplied by the protein, i.e. two from tyrosinate residues, one from an aspartate residue and one from a histidine residue, plus two ligands supplied by an exogenous, bidentate carbonat [173].

[207]. The adult human body contains approximately 3–5 g of iron and more than two thirds of this iron (>2 g) is incorporated in haemoglobin. However, free iron is found to be toxic, promoting free radical formation resulting in oxidative damage to tissues [204, 205, 207]. For these reasons, it is vital that iron is transported in an inactive. The primary role of transferrin is therefore to transport iron safely around the body to supply cells. Plasma concentration of Tf is stable from birth, ranging from 2 mg/ml to 3 mg/ml, and the in vivo half-life of this protein is eight days [204]. Thus, iron bound to plasma Tf corresponds to less than 0.1% of total body iron ($\sim$3 mg), but it represents the most active pool in kinetic terms [205]. The binding and release of iron by Tf involves several factors, including pH, temperature and protein and ionic concentrations [204, 206].

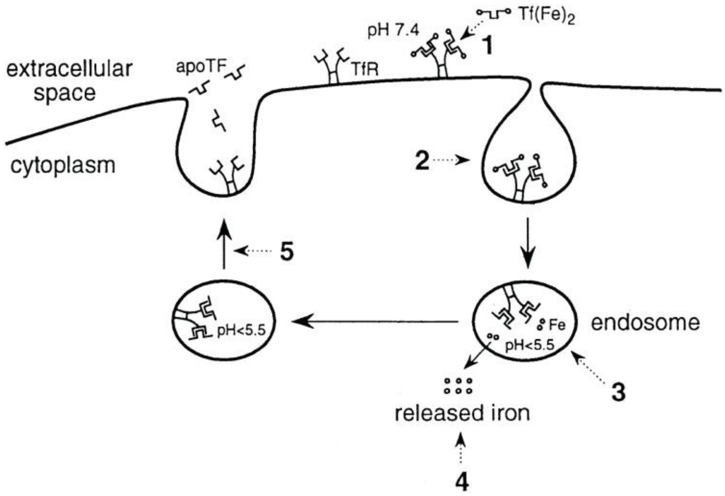

Figure 3.6: *Cellular uptake of iron through the Tf system via receptor-mediated endocytosis.*

The transferrin receptor system Iron-loaded Tf (holo-Tf, Tf(Fe)$_2$ in Figure 3.6) binds transferrin receptors (TfR) on the surface of actively dividing cells [204, 206] (1 in Figure 3.6). Subsequently, the Tf–TfR complex is internalized and transported to endosomes (2 in Figure 3.6). ATP-dependent proton pumps then force H+ ions into the endosomes reducing the pH to 5.5, promoting iron release (3 and 4 in Figure 3.6) [204, 206]. Under low pH conditions, the TfR alters its conformation to enable apo-Tf to remain bound to the receptor. Once the complex reaches the cell surface, the TfR changes again its conformation due to pH increases, causing the realise of the apo-Tf (5 in Figure 3.6). The apo-Tf molecules then circulate until they become in contact with free iron again, and the cycle of Tf-mediated iron redistribution is continued. TfR is an attractive molecule for the targeted cancer therapy since it is upregulated on the surface of many cancer types. Additionally, TfR is efficiently internalized, allowing the use of Tf as a therapeutical delivery agent in cancer cells [208].

3.2 Materials and methods

3.2.1 Synthesis of silica NPs

Reagents

Tetraethyl orthosilicate (TEOS) (Sigma 520918), absolute ethanol and aqueous ammonia (28%) were purchased from Sigma Aldrich (St. Louis, MO). Deionised water with resistivity ~ 18.2 MΩ has been used in all the experiments. All glasswares were firstly immersed in acidic bath, then abundantly rinsed in deionised water, and successively immersed in basic bath overnight. Before the use glasswares were abundantly rinsed in deionised water.

Synthesis and characterization

Colloidal, negatively charged SiO_2 NPs of ~ 50 nm diameter were prepared by hydrolysis and condensation of tetraethyl orthosilicate (TEOS) in the presence of ethanol and ammonia, according to the Stöber methodology [177, 209].

To obtain 50 nm SiO_2 NPs aqueous ammonia (28%) (1.827 g) was added to absolute EtOH to a total volume of 50 ml and rapidly stirred. 1.99 ml of TEOS was then rapidly added to this mixture. The reaction was sealed and stirred at room temperature for a further 20 hours. The NPs were then centrifuged at 2000×g for 10 minutes for removing large aggregates. The ethanol excess in the supernatant was then eliminated by evaporation using a rotary evaporator under aspirator vacuum. Further purification was achieved by centrifugation (2000×g for 10 minutes) and filtration, in order to remove all the present aggregates. The final concentration was measured by drying an aliquot of the NP solution at 90°C for ~2 hours. The concentration of the final NP stock is ~3 mg/ml.

The Z-Potential of the NPs is ∼-35 mV. Figure 3.7 shows a representative DLS measure by intensity of the as synthesized 50 nm SiO_2 NPs. The NP dimension was further investigated by TEM. Figure 3.8 report the size distribution of the NPs. Data reported in figure 3.8 are extrapolated from TEM images represented in figure 3.9.

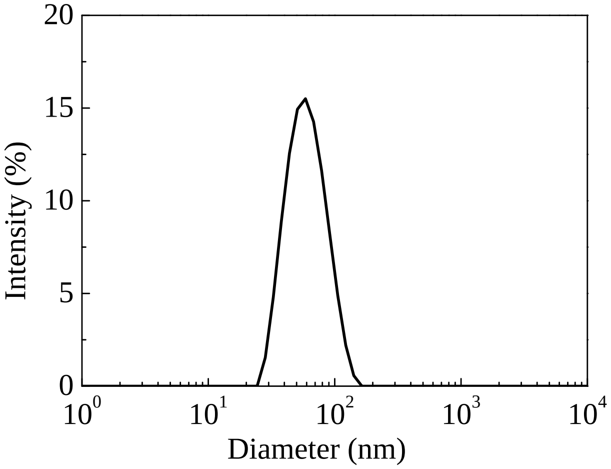

Figure 3.7: Representative DLS by intensity results of the synthesis of 50 nm SiO_2 NPs

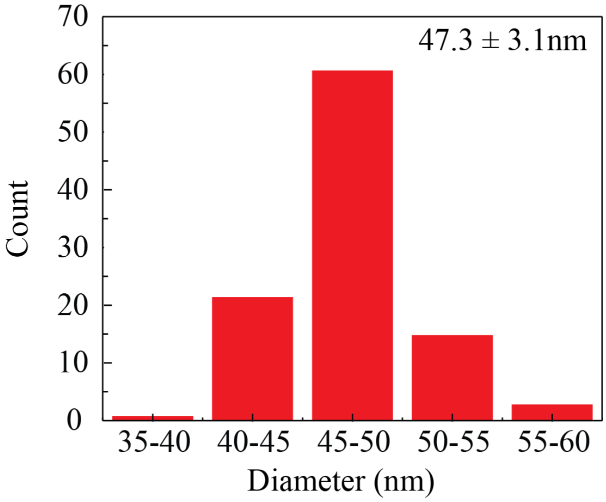

Figure 3.8: Representative size distribution of synthesized 50 nm SiO_2 NPs extrapolated from TEM images.

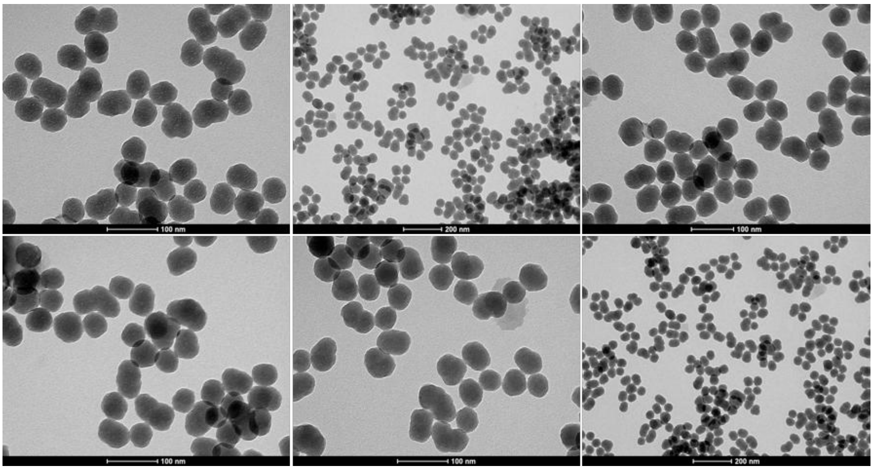

Figure 3.9: Representative TEM images of synthesized 50 nm SiO_2 NPs

3.2.2 Proteins

Chicken egg-white lysozyme (L-6876) and bovin α-casein (C6780) were purchased from Merck (Darmstadt, Germany). Human α-synuclein and yeast $Sic1^{\Delta 214}$-His_6 were expressed in *Escherichia coli* and purified as previously described respectively by Latawiec et al. [210] and by Brocca et al. [200]. Human α-synuclein nucleotide sequence was cloned into the pET11a expression vector and introduced into *Escherichia coli* strain BL21 (DE3). Expression of α-synuclein was obtained by growing cells in 100 μg/mL ampicillin containing Luria-Bertani broth at 37°C until an OD600 of about 0.6, followed by induction with 0.6 mM isopropyl β-thiogalactopyranoside for 5 hours [210]. All the proteins and NP stock solutions were prepared in 10 mM phosphate-buffered saline (PBS), pH = 7.4. The final composition of the buffer is 137 mM NaCl, 2.7 mM KCl, 10 mM Na_2HPO_4 and 2 mM KH_2PO_4. Protein concentration was assessed by absorbance at 280 nm, employing the following extinction coefficients:

- 36000 M^{-1} cm^{-1} for lysozyme [211]

- 1490 M^{-1} cm^{-1} for Sic1$^{\Delta 214}$-His$_6$, calculated from the aminoacid sequence by ExPASy ProtParam tool [212]
- 25900 M^{-1} cm^{-1} for α-casein, calculated from the aminoacid sequence by ExPASy ProtParam tool [212],
- 5120 M^{-1} cm^{-1} for α-synuclein [213]
- 85240 M^{-1} cm^{-1} for apotransferrin and holotransferrin, determined by sigma datasheet.

Sic1$^{\Delta 214}$-His$_6$ production and purification

Yeast Sic1$^{\Delta 214}$-His$_6$ was cloned and expressed in *E. coli* according to Brocca et al. [200]. Pre-cultures were inoculated from a single-cell colony from a fresh selection plate. Preparative cultures were obtained in shaking flasks by 1:20 dilution of pre-cultures in fresh Luria-Bertani broth supplemented with 50 mg/l ampicillin. Thus, the volumes were scaled from 20 to 200 ml and the cultures were grown at 37°C and 220 rpm to an optical density at 600 nm (OD600) between 0.5 and 0.7. Cultures were then transferred to 30°C to reduce the risk of proteolytic degradation and induced with 200 μM isopropyl-β-d-thiogalactopyranoside (IPTG) to an OD600 of 1.3.

Induced cells were then collected by centrifugation at 9400 g at room temperature for 15 min. The supernatant was discard and the pellet resuspended in the extraction buffer. Lysated cells were then disrupted by french press. The cell suspension was collected and exposed to denaturing thermal treatment by incubating the suspension at 95°C for 5 minutes. An intrinsically disordered protein might be enriched in the soluble fraction of heat-treated crude extracts based on their resistance to heat treatment. The IDP-enriched-crude-extracts were then cooled in ice for 10 minutes and centrifuged for 10 minutes at 10000×g to collect cellular debris and the insoluble protein fraction. Finally, the protein was purified by Immobilized-Metal Affinity Chromatography (IMAC) schematically represented in Figure 3.11 [200]. The chemical affinity between Ni^{2+} and the His-Tag promotes binding of the protein to the resin, which, is then eluted by the application of the elution buffer containing 50 mM sodium phosphate, 300 mM NaCl, 250 mM imidazole, pH 8.0. The eluted fraction corresponds to the purified protein. The typical concentration value of purified protein obtained by this procedure is 0.3 mg/ml.

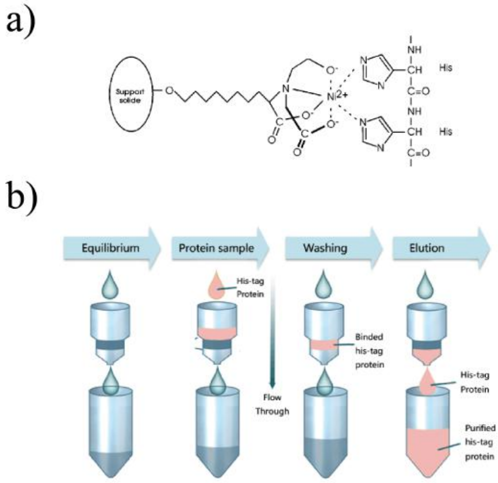
a)
Support solide
Ni2+
NH
CH
His
C=O
NH
CH
His
C=O
b)
Equilibrium
Protein sample
Washing
Elution
His-tag Protein
Binded his-tag protein
Flow Through
His-tag Protein
Purified his-tag protein

Figure 3.10: *Immobilized-metal affinity chromatography IMAC.* a) Representation of the Ni^{2+} resin; b) Representation of the IMAC procedure.

Figure 3.11 report the SDS-PAGE analysis of the all the passages of $Sic1^{\Delta214}$-His_6 expression and purification. The loading order of the lanes is indicated in the caption. Particularly, lane 8 and lane 9 confirm the final purified sample by the characteristic bands at ∼9200 kDa.

The secondary structure of the purified $Sic1^{\Delta214}$-His_6 has been investigated by CD after further protein purification for desalting by gel filtration chromatography on PD-10 columns. This step allows the separation of high molecular weight substances from small molecules like salts and buffer components. The PD 10 final buffer was Ammonium

Acetate 200 mM. The resulting CD of the PD 10-purified Sic1$^{\Delta 214}$-His$_6$ is reported in figure 3.12.

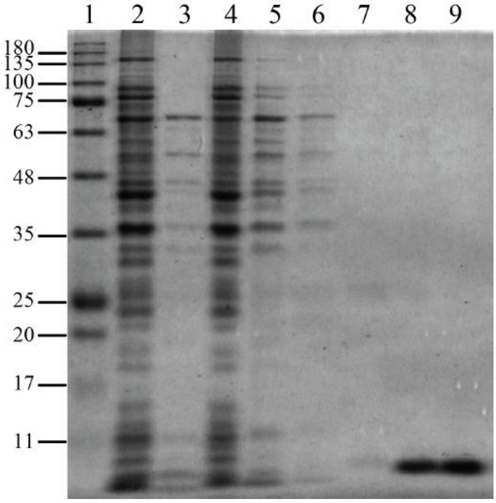

Figure 3.11: *SDS-PAGE analysis of Sic1$^{\Delta 214}$-His$_6$ purification.* The loading order of the lanes is: lane 1 protein-marker, lane 2 total fraction of expressed protein; lane 3 not soluble fraction of expressed protein; lane 4 flow-through fraction of expressed protein; lane 5 soluble fraction of expressed protein; lane 6 first washed fraction; lane 7 second washed fraction; lane 8 Eluate 1; lane 9 Eluate 2. Lane 8 and lane 9 correspond to the eluate with higher purified protein concentration.

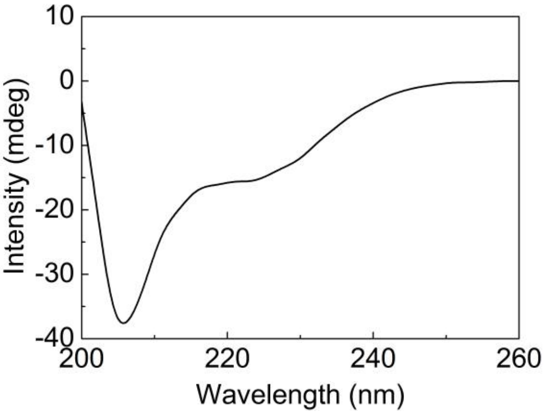

Figure 3.12: Circular dichroism of the PD-10-purified Sic1$^{\Delta 214}$-His$_6$.

The CD spectra was collected after lyophilization of the protein solution and powder resuspension in PBS. The presence of the peak at $\sim$ 200 nm is consistent with a mainly random coil secondary structure of Sic1$^{\Delta214}$-His$_6$.

3.2.3 Hard corona preparation

The hard corona samples were prepared by incubating 10 mg/mL NPs with 150 μM protein solution (final concentrations in a final volume of 100 μL). The corresponding protein/NP molar excess is $\sim$8-9$\times10^2$. The mixed solution has been kept under mild agitation for 1 hour at 4°C. The temperature of 4°C has been chosen in order to prevent any possible temperature perturbation of the protein structure. After incubation the nanoconjugates are collected and washed by four cycles of centrifugation and resuspension in fresh buffer at 17000$\times$g for 10 minutes. Resuspension has been performed by 30 seconds sonication in 1 mL of fresh PBS buffer. The final pellets were resuspended in 100 μL of fresh PBS for biophysical analyses. The controls were prepared by the same procedure using either protein solution without NPs or NPs dispersion without protein

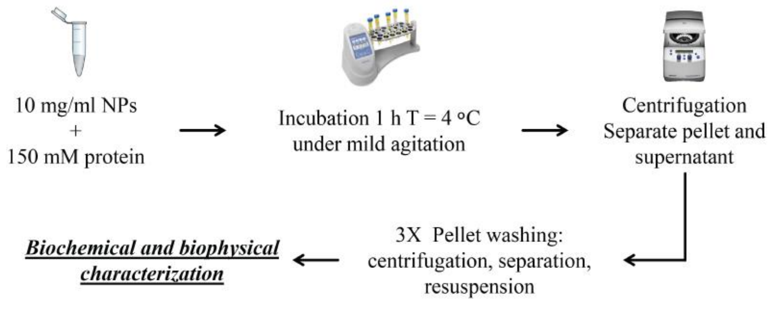
10 mg/ml NPs
+
150 mM protein
Incubation 1 h T = 4 °C
under mild agitation
Centrifugation
Separate pellet and
supernatant
3X Pellet washing:
centrifugation, separation,
resuspension
Biochemical and biophysical
characterization

Figure 3.13: Protocol for hard corona preparation.

The protein concentration inside the hard corona was not directly determined by measuring the sample absorbance at 280 nm due to NP scattering which interfere with the direct mesure. Alternatively, protein concentration in the hard corona was calculated by the difference between the initial protein amount and that removed by washing step.

3.2.4 Characterization techniques

DLS measurements

The hydrodynamic diameter of NPs was measured by dynamic light scattering (DLS) on a Malvern Zetasizer Nano ZS90 (Malvern Instruments Ltd, Worcestershire, UK). The samples were prepared at an average concentration of 100 μg/mL in PBS and were allowed to equilibrate at 25°C for 30 seconds before the analysis.

CD measurements

CD spectra were acquired in the range of 260–190 nm on a J-1500 spectropolarimeter (JASCO Corporation, Tokyo, Japan), equipped with a Peltier system for temperature control, in a 1 mm-pathlength cuvette containing 100 μL of sample, using 1-nm bandwidth and 20 nm/s scanning speed. Spectra were subtracted by the blank and baselines were aligned at 260 nm.

TEM analysis

TEM images were acquired on a FEI Tecnai G2 Spirit BioTWIN instrument (Hillsboro, Oregon, USA) operating at 120 kV. For this purpose, a 1 μL drop of NPs was deposited on a formvar-coated, copper grid and allowed to dry overnight. For observation of the protein Corona, the samples were negatively stained using 2% uranyl acetate staining solution in PBS. To this purpose, the grids were put on the staining drop for a few minutes, the excess of staining was dried by filter paper and the grid was allowed to dry on air overnight. NP size distribution was investigated using the MeasureIT software (Image Processing and Analysis in Java), taking into consideration 200 NPs per sample.

FTIR measurements

For Fourier-Transform Infrared (FTIR) measurements, 2-4 µL of the samples were deposited on a BaF_2 infrared window and dried at room temperature, in order to obtain a solid film. The FTIR absorption spectra were then acquired in transmission mode by means of a Varian 670-IR FTIR spectrometer coupled to the Varian 610-IR infrared microscope (both from Varian, Mulgrave VIC, Australia Pty Ltd) equipped with a mercury cadmium telluride nitrogen-cooled detector [214]. Measurements were performed at 2 cm^{-1} spectral resolution, 25 kHz scan speed, 512 scan co-additions, and triangular apodization. The variable microscope aperture was adjusted to 100 µm × 100 µm and 5-10 areas for each sample were measured to verify the reproducibility of the results. Only spectra with the Amide I band intensity below 0.8 were considered reliable.

For H/D exchange, the protein film on the BaF_2 window was rehydrated by the deposition of 8 µL of D_2O around the dried films. The chamber was then tightly closed by a second window using a flat O-ring [215] and incubated for 5 hours at room temperature to allow an extent of exchange comparable to that obtained by conventional transmission-mode measurements on protein solutions in D_2O [201, 216, 217]. The FTIR spectra of the D_2O-rehydrated samples were collected as described above.

The protein spectra were obtained by subtraction of the proper reference spectra, strictly collected under the same conditions, by adjusting the subtraction factor until a flat baseline was obtained in the 2200–1750 cm^{-1} region. In this region, NPs displayed the typical bulk SiO_2 bands at $\sim$1978cm^{-1} and at $\sim$1872 cm^{-1} [218]. Figure 3.14 report a representative subtraction procedure for lysozyme. The blue spectrum is related to the protein constituting the hard corona and is obtained by subtracting the NP signal from the measured spectrum. In the spectrum obtained by subtraction, the SiO_2 bands at $\sim$1978 cm^{-1} and at $\sim$1872 cm^{-1} are not present, highlighting a successful subtraction procedure.

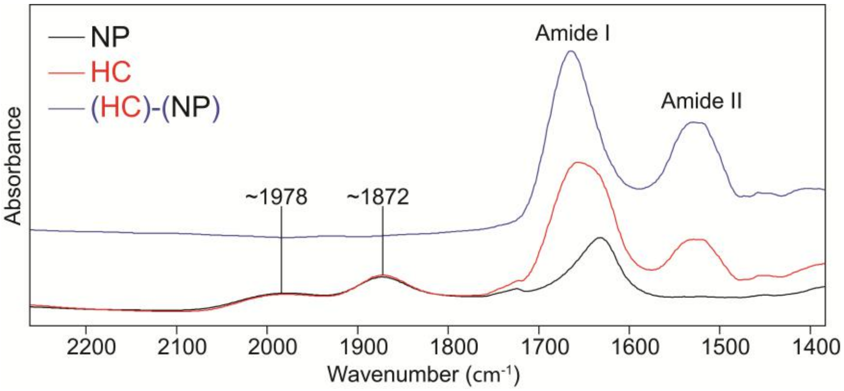

Figure 3.14: *FTIR spectra*: representative subtraction procedure for lysozyme hard corona.

Absorption spectra were normalized by the Amide I band area, to compensate for possible differences in the protein content, and the second-derivatives [219] were calculated following the Savitsky-Golay method. Data collection and analysis were performed using the Resolutions-Pro software (Varian, Mulgrave VIC, Australia Pty Ltd).

SDS PAGE analysis

For the extent explication of SDS PAGE refer to the material and methods section of Chapter 2. SDS PAGE at 16%-18% acrylamide concentration (depending on the molecular weight of the examined protein) was used to visualize the proteins recovered from hard corona samples. Proteins were detached from the NP surface by boiling 5 min in SDS sample buffer (2% w/v SDS) [129]. The electrophoresis was performed according to SDS PAGE original protocol [129], on vertical 1-D minigels (Mini-PROTEAN IV, Bio-Rad laboratories, Hercules, California, U.S.A.). Broad-range, pre-stained molecular-weight standards from 11 kDa to 180 kDa (GeneSpin, Milan, Italy) were used for gel calibration. Gels were stained in Coomassie blue (Bio-Rad laboratories, Hercules, California, U.S.A.).

Study of α-synuclein aggregation in the presence of NPs

The aggregation reactions were carried out in a 96-well View Plates (Perkin Elmer, Waltham, MA) in a total volume of 100 μL. Each well contained recombinant human α-synuclein at constant concentration of 0.5 mg/mL in 0.1 M NaCl, 20 mM Tris pH 7.4 and 10 μM Thioflavin T (ThT). The aggregation reactions were performed in the presence of increasing NPs concentrations at the follow α-synuclein to NPs ratios: 1:0.1; 1:0.5, 1:1, 1:2 and 1:5. The ratios here are expressed in terms of mg/mL. Reactions were performed at 37°C under constant shaking and in the presence of one 3-mm glass bead. The fluorescence was read every 5 min on Spectramax M5 fluorescence microplate reader (Molecular Devices, Sunnyvale, CA) by bottom reading at excitation of 444 nm and emission of 485 nm. Each sample analysis was performed in four replicates.

These experiments were performed in collaboration with the group of Prof. Giuseppe Legname in Trieste (SISSA).

Fluorescence emission analysis

The detection of the Tb(III)- Transferrin fluorescence was performed on a Cary Eclipse (Varian - California, USA) fluorescence spectrophotometer coupled with a Cary Temperature Controller (Varian - California, USA) temperature control system. Samples were analyzed in 1 cm-pathlength cuvette at 25°C. The spectra were acquired by excitation at 295 nm, monitoring the emission in the range 310-575 nm. Ammonium Acetate ($C_2H_7NO_2$) supplemented with ammonium bicarbonate (NH_4HCO_3) at respectively final concentration of 100 mM and 25 mM, pH 8.1, was used for fluorescence measurements (AAB buffer). The complexes were formed by incubation for 10 minutes of a 25 μM apo-Tf solution with an excess of terbium chloride ($TbCl_3$ 3 mM). Each spectrum was subtracted by the blank, consisting of the only AAB buffer.

3.3 Results and discussion

3.3.1 Hard Corona preparation

UV-Vis and SDS-PAGE of the hard corona samples

Figure 3.15 reports the trend of the protein concentration in the supernatant of the first four centrifugation cycles, determined by UV absorbance at 280 nm. Concentration was calculated by the lambert-Beer law, knowing the molar absorbance coefficient of all the proteins. The trend of the plots in Figure 3.15 clearly shows the progressive protein depletion in the supernatants. The red line in figure 3.15 represents the evolution of the protein concentration in the supernatant of each centrifugation step in the presence of NPs, while the black line shows the evolution of the protein concentration in the supernatant of each centrifugation step in the absence of NPs. The free protein concentration is already negligible after the first step. The pellet of the fourth cycle has been resuspended and the hard corona sample is considered formed. The hard corona samples prepared as described have been used in all the following experiments.

Figure 3.16 reports the SDS PAGE analysis of the material recovered from the bioconjugates. By comparing the supernatants of the first centrifugation step in the absence (lane 2) or presence of NP (lane 3) it is possible to appreciate the amount of adsorbed protein onto the NP surfaces, by the difference in intensity of the two lanes. The presence of the protein in the final hard corona sample is confirmed by the presence of the characteristics band in lane 6, corresponding to the pellet of the fourth centrifugation cycle of the protein + NP sample (the hard corona sample). On the contrary, no protein band is detectable in the final pellet of the control samples with either protein only (lanes 4) or NPs only (lanes 5).

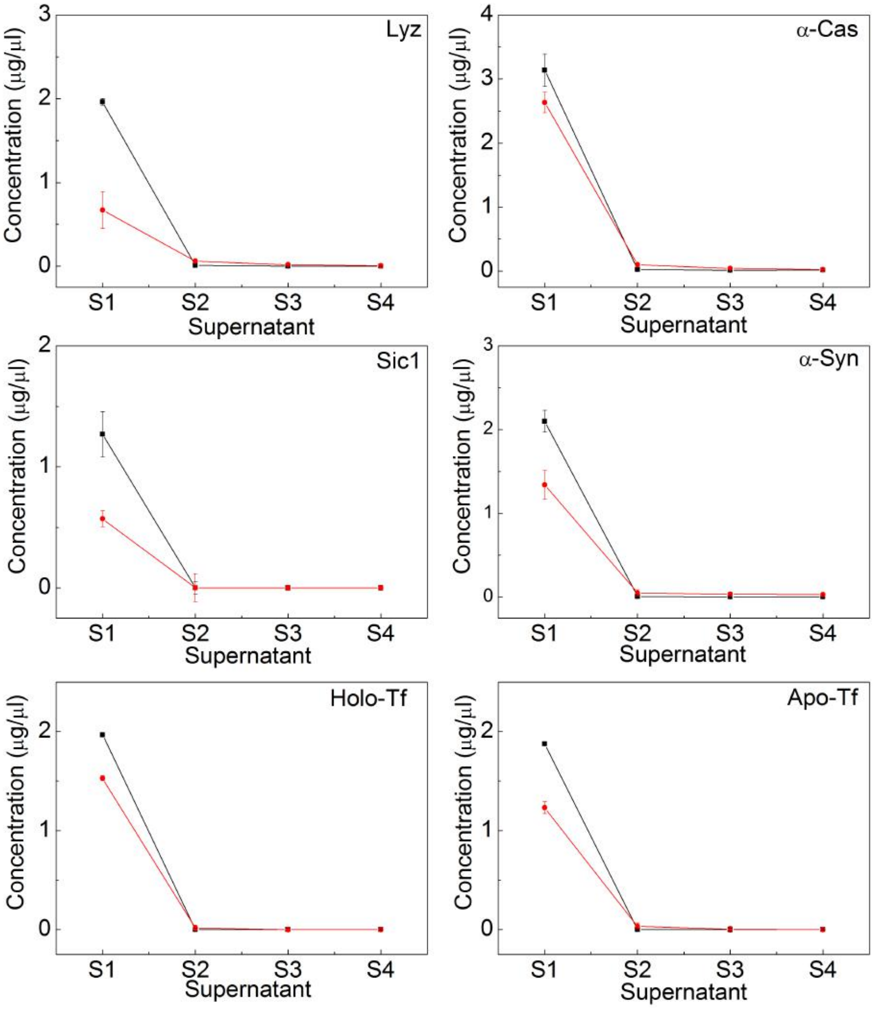

Figure 3.15: Protein concentration in the supernatant of each centrifugation step in the presence (red line) or absence (black line) of NPs. α-Cas, α-casein; α-Syn, α-synuclein; Lyz, lysozyme; Sic1, Sic1$^{\Delta 214}$-His$_6$; Holo-Tf, holotransferrin; Apo-Tf, apotransferrin.

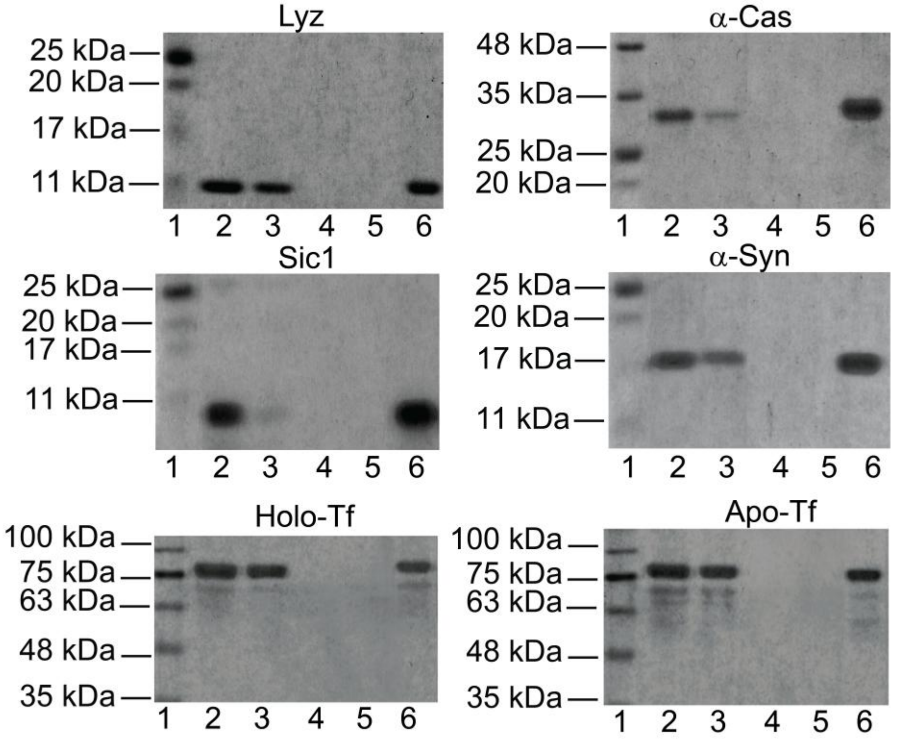
Lyz
25 kDa
20 kDa
17 kDa
11 kDa
1 2 3 4 5 6
α-Cas
48 kDa
35 kDa
25 kDa
20 kDa
1 2 3 4 5 6
Sic1
25 kDa
20 kDa
17 kDa
11 kDa
1 2 3 4 5 6
α-Syn
25 kDa
20 kDa
17 kDa
11 kDa
1 2 3 4 5 6
Holo-Tf
100 kDa
75 kDa
63 kDa
48 kDa
35 kDa
1 2 3 4 5 6
Apo-Tf
100 kDa
75 kDa
63 kDa
48 kDa
35 kDa
1 2 3 4 5 6

Figure 3.16: *SDS PAGE*. Lane 1, molecular-weight markers; lane 2, supernatant of the first centrifugation step (protein only); lane 3, supernatant of the first centrifugation step (protein + NPs); lane 4, pellet of the fourth centrifugation step (protein only); lane 5, pellet of the fourth centrifugation step (NPs only); lane 6, pellet of the fourth centrifugation step (protein+ NPs). α-Cas, α-casein; α-Syn, α-synuclein; Lyz, lysozyme; Sic1, Sic1$^{\Delta 214}$-His$_6$, Holo-Tf, holotransferrin; Apo-Tf, apotransferrin.

IDPs are known to migrate slower in SDS PAGE compared to globular proteins with the same molecular mass as a result of their enrichment in charged amino acids and pourly hydrophobic residues [220]. For this reason, in figure 3.16 the IDP characteristic bands are found not to correspond to their molecular weight. Finally, it is also shown that holo- and apo-Tf hard corona undergo degradation to lower molecular weight products. This effect is more pronounced in the case of the apo-Tf, and it could be due to the proteolytic cleavages by traces of contaminant proteases. Since susceptibility to partial proteolysis is strongly affected by protein conformation, this result suggests that apo-Tf undergoes significant structural rearrangement in the presence of silica NPs.

The absorption yield has been calculated by subtracting the protein concentration in the supernatant in the presence of NPs from the protein concentration in the supernatant in absence of NPs as indicated by equation 3.1, where C_{HC} is the protein concentration in the hard corona, $C^{Protein}_{S1+S2+S3+S4}$ the protein concentration in the supernatant in absence of NPs and $C^{NP+Protein}_{S1+S2+S3+S4}$ the protein concentration in the supernatant in the presence of NPs.

$$C_{HC} = C^{Protein}_{S1+S2+S3+S4} - C^{NP+Protein}_{S1+S2+S3+S4} \tag{3.1}$$

Table 3.1 shows the results of this calculation. The data have been extrapolated from figure 3.15. For this calculation it has been assumed that no loss of NP takes place during the washing cycles.

DLS analysis

For all the investigated samples, a significant increase in NP dimensions has been observed (Figure 3.17 and Table 3.2). The average hydrodynamic diameter shifts from the 50 nm of the as synthesized fresh NPs, to over 300 nm. In particular, in the case of lysozyme and $Sic1^{\Delta 214}$-His_6 the hydrodynamic diameter has been detected in the micrometer scale, while for α-synuclein and holo-Tf aggregates are detected. For lysozyme, this detection is in agreement with some previous observation suggesting that this protein induce strong aggregation of silica, polystyrene, and gold NPs [65, 70–73]. Additionally, DLS measurements of the $Sic1^{\Delta 214}$-His_6 in absence of NP indicate a diameter which is discrepant from the expected size value for $Sic1^{\Delta 214}$-His_6, which is a ~9000 kDa protein (see Table 3.3). This observation is consistent with an intrinsic instability

	$C_{(S1+S2+S3+S4)}$ only protein (mg)	$C_{(S1+S2+S3+S4)}$ protein + NPs (mg)	C_{HC} (mg)	Yeld (%)
Lysozyme	1.99 ± 0.09	0.75 ± 0.23	1.27 ± 0.36	62 ± 13
α-casein	3.33 ± 0.4	2.8 ± 0.24	0.3 ± 0.1	10 ± 4
Sic1$^{\Delta 214}$-His$_6$	1.23 ± 0.17	0.6 ± 0.2	0.6 ± 0.2	53 ± 12
α-synuclein	1.99 ± 0.4	1.4 ± 0.11	0.6 ± 0.2	29 ± 7
holo-Transferrin	1.97 ± 0.02	1.54 ± 0.16	0.5 ± 0.15	24.6 ± 7
apo-Transferrin	1.88 ± 0.01	1.27 ± 0.13	$0.65 \pm 0{,}2$	33.9 ± 8

Table 3.1: Calculated yeld of protein adsorption inside the hard corona for all the analysed protein. The experimental error in the calculation of the protein concentration of supernatants here has been derived from triplicates measurements, while for the protein concentration inside the hard corona an estimated experimental error of 30% has been used.

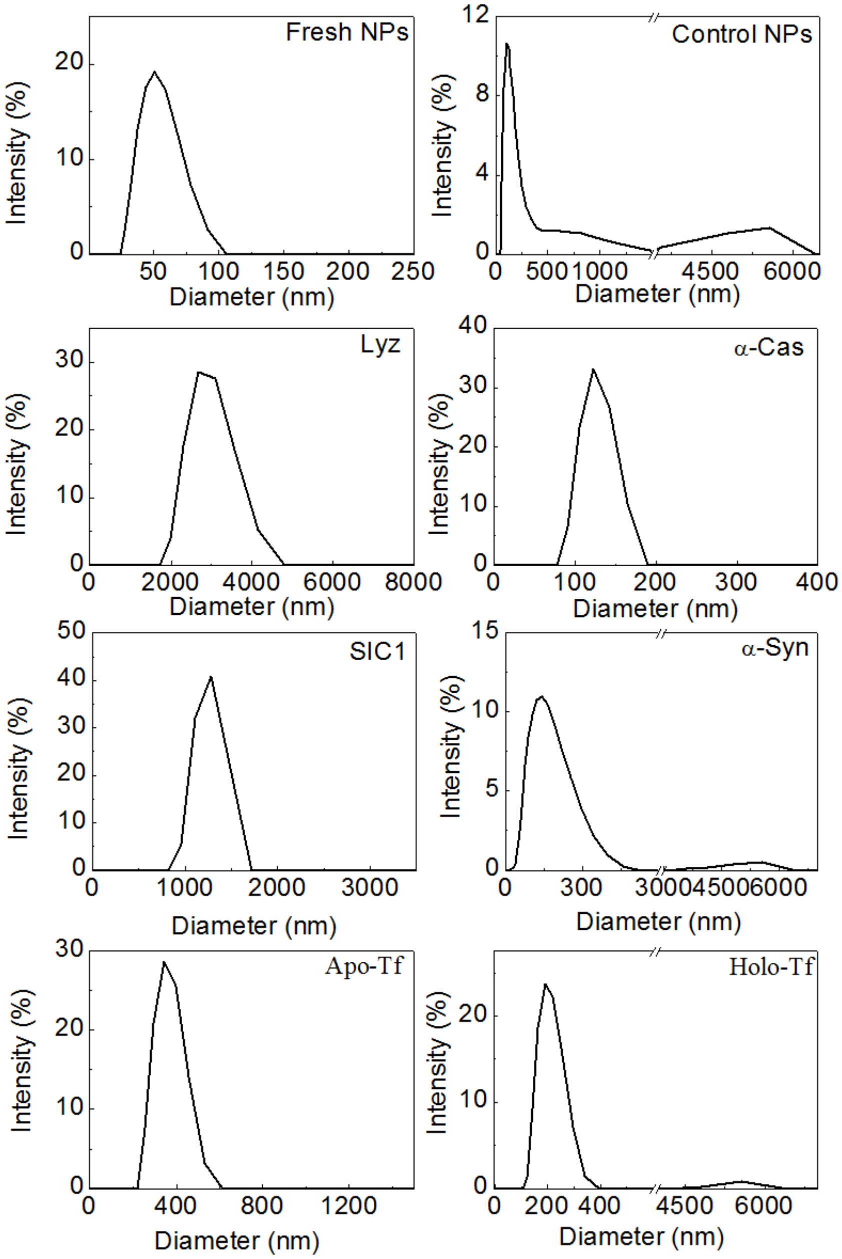

Figure 3.17: *Distributions of the hydrodynamic diameter measured by DLS.* A representative profile is reported for each hard corona sample, for the naked original NPs (called Fresh NPs), and for naked NPs treated by the same steps as the hard corona samples (called Control NPs). α-Cas, α-casein; α-Syn, α-synuclein; Lyz, lysozyme; Sic1, Sic1$^{\Delta 214}$-His$_6$; Holo-Tf, holotransferrin; Apo-Tf, apotransferrin.

Sample	D_H	PDI
NP control	393.7 ± 58.2	0.336 ± 0.016
NP + Lysozyme	2973 ± 261.7	0.252 ± 0.014
NP + α-casein	126.9 ± 2.80	0.233 ± 0.007
NP + $Sic1^{\Delta214}$-His_6	2144 ± 242.9	0.277 ± 0145
NP + α-synuclein	172.5 ± 30.00	0.225 ± 0.008
NP + Holo-Transferrin	241.3 ± 55.50	0.221 ± 0.016
NP + Apo-Transferrin	375.6 ± 13.40	0.146 ± 0.055

Table 3.2: DLS measure of all the hard corona, compared to the NP control.

under these experimental conditions (PBS, pH 7.4) as reported by Brocca et al. [200].

The high increase in NP dimension after the hard corona formation indicated by the DLS analysis is not attributed to the formation of several layers of proteins on the NP surface. This observation is confirmed by TEM images reported in the following subsection, where only a thin layer of protein is visible. SiO_2 NPs undergo aggregation after the centrifugation steps even in the absence of protein. For this reason, the DLS measurement cannot be used to evaluate the morphology of the hard corona layer, as well as the presence of the protein corona.

TEM analysis

NP size was measured by TEM before and after hard corona formation implementing the negative staining by uranyl acetate technique. The uranyl acetate staining allow for the direct visualization of the adsorbed protein and the size determination of the hard corona. The hard corona thickness was estimated according to a simple core–shell model, with protein molecules surrounding the NPs (figure 3.18).

Images of naked and coated NPs are reported in figure 3.19, while figure 3.20 shows the size distribution of the colloids derived from 200

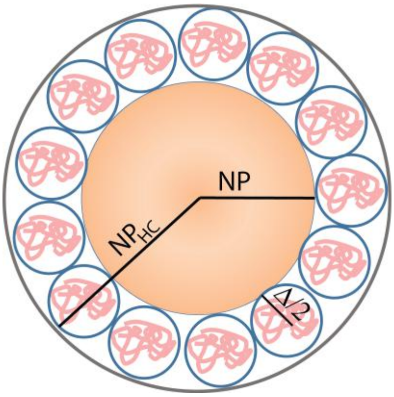

Figure 3.18: Core–shell model with proteins surrounding NPs for the estimation of the protein layer thickness. NP radius of NP;Δ/2 radius of protein, NP$_{HC}$=NP + Δ/2

randomly picked NP. The as synthesized fresh NPs shows an average size of 47.3 ± 3.1 nm with a narrow size distribution. The control NP sample (the sample treated by the same procedure as the hard corona samples in the absence of any protein) display similar features. As a result of incubation with proteins and after the washing cycles, NPs acquire a larger diameter and appear surrounded by a light halo, ascribable to the hard corona. The hard corona thickness was thus calculated by the size difference of coated and naked NPs. The inset shows a single enlarged NP, in order to appreciate the effect of the staining on NPs.

The thin layer surrounding the SiO_2 NPs derive from protein adsorption and it is clearly showed by the selected TEM images in Figure 3.19. This adsorbed protein layer completely coats the NPs, also in the case of aggregates of NPs, and its thickness is highly regular.

In order to estimate how many layers of protein are adsorbed on the NP surface, the theoretical hydrodynamic diameter of each protein was calculated according to the relation with chain length, specific for globular or disordered proteins [33, 201] and respectively depicted by the equations 3.2 and 3.3:

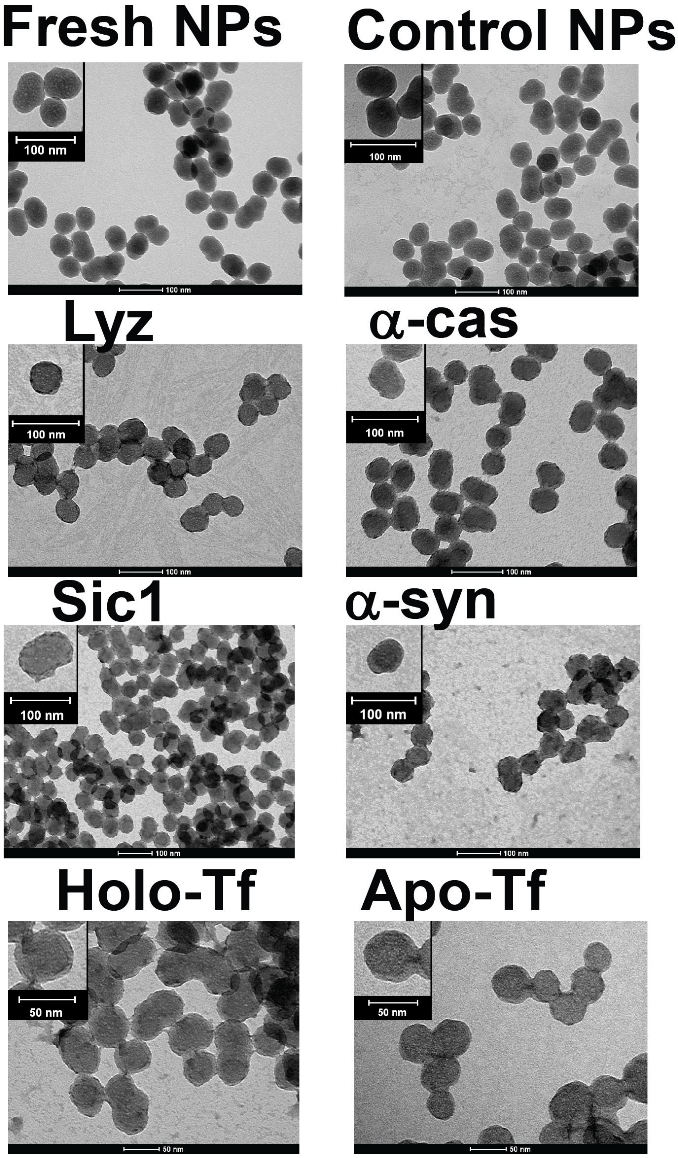
Fresh NPs
Control NPs
100 nm
Lyz
α-cas
Sic1
α-syn
Holo-Tf
Apo-Tf
50 nm

Figure 3.19: *TEM analysis*. A representative TEM image is reported for each hard corona sample, for the naked, as synthesized NPs (Fresh NPs), and for NPs treated by the same steps as the hard corona samples (Control NPs). Scale bars for 100 and 50 nm are given. α-Cas, α-casein; α-Syn, α-synuclein; Lyz, lysozyme; Sic1, Sic1$^{\Delta214}$-His$_6$; Holo-Tf, holotransferrin; Apo-Tf, apotransferrin.

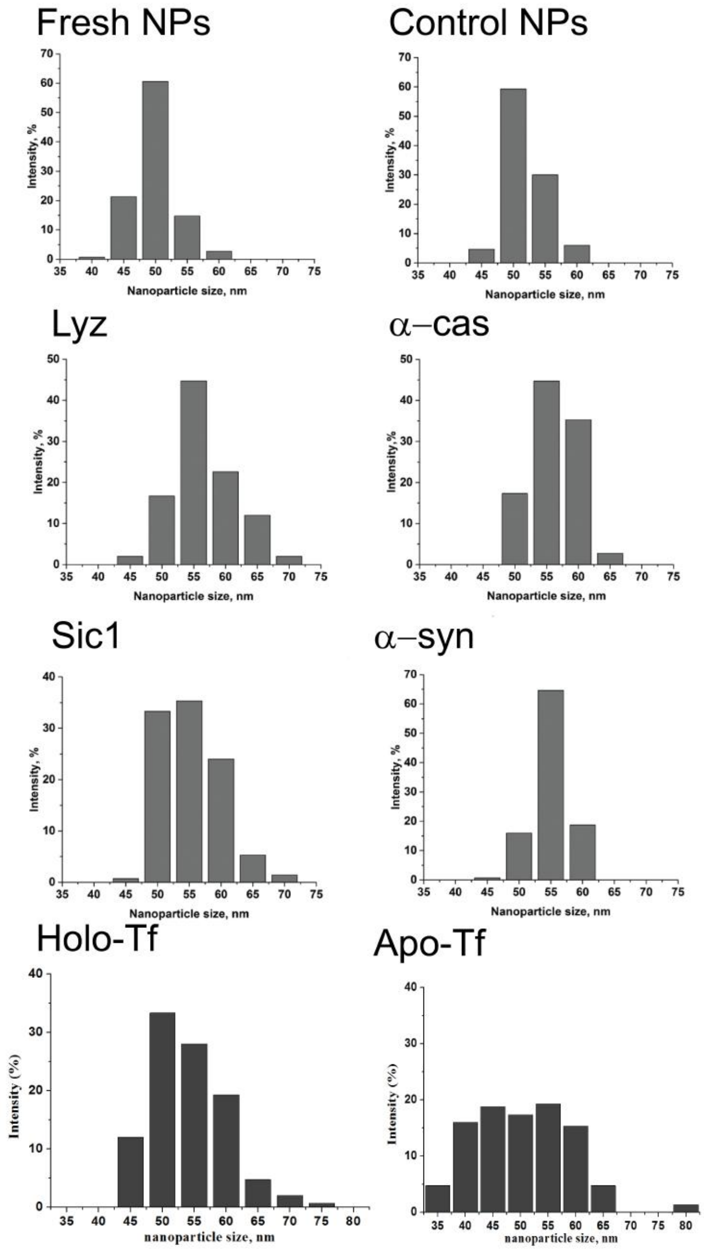

Figure 3.20: *Size distribution.* Size distributions derived from 200 randomly picked NPs from each sample. α-Cas, α-casein; α-Syn, α-synuclein; Lyz, lysozyme; Sic1, Sic1$^{\Delta 214}$-His$_6$; Holo-Tf, holotransferrin; Apo-Tf, apotransferrin.

$$log(R_H^{glob}) = 0.525 + 0.358log(N) \tag{3.2}$$

$$log(R_H^{IDP}) = 2.49N^{\nu} \tag{3.3}$$

Where N is the residues number and ν is a factor equal to 0.509. These equations are simple fits of empiric data deriving from the analysis of the hydrodynamic dimensions of globular proteins in different conformational states and on the hydrodynamic behaviour of 60 IDPs under conditions of neutral pH and physiological salt concentrations, and are not based on a theoretical physical model [33]. In the case of IDPs, a range of values is indicated. The maximum and minimum value represents the limit cases of molten-globule or native-coil conformation [33].

Table 3.3 reports the diameter values for the hard corona samples (NP$_{HC}$) and the control sample of NPs (NP) in absence of proteins obtained by TEM. DLS measurements of the hydrodynamic radius is also reported (DLS measurements of R$_H$). The experimental estimation of the hard corona thickness is given by the half the difference ($\Delta/2$) between the hard corona samples (NP$_{HC}$) and the control sample of NPs (NP). Thus, this value is compared to the diameter of the free protein in solution, determined by the relation to chain length [33] and calculated by equations 3.2 and 3.3. This value match the thickness of the hard corona for lysozyme and transferrin, indicating that the two hard corona are formed by a monolayer of natively folded protein molecules, stably adsorbed to the surface of NPs. Contrary, for IDPs the hard corona thickness assessed by TEM is smaller than expected, even in the hypothesis of a molten-globule state. This observation suggests that IDP are collapsed on the surface of the NPs. This phenomena could be due to the extensive interactions with the NP surface or can be induced by dehydration on

Protein	NP_{HC} (nm)	NP (nm)	$\Delta/2$ (nm)	Calculated R_H (nm)	DLS measurements of R_H (nm)
Lysozyme (129)	54.08 ± 4.98	47.71 ± 3	3.18	3.8	3.54 ± 0.09
α-casein (214)	53.55 ± 3.60	47.71 ± 3	2.92	5.1 - 8.02	12.6 ± 1.18
$Sic1^{\Delta 214}$-His_6 (77)	52.82 ± 4.45	47.71 ± 3	2.55	3.64 - 4.84	347.8 ± 3.80
α-synuclein (140)	52.74 ± 2.70	47.71 ± 3	2.51	4.44 - 7.1	7.91 ± 1.02
holo-Transferrin (678)	56.47 ± 5.80	47.71 ± 3	4.38	4.53	7.26 ± 0.19
apo-Transferrin (678)	57.37 ± 8.95	47.05 ± 3	5.16	4.53	5.82 ± 0.14

Table 3.3: *Calculation of the hard corona thickness*. Diameter values are obtained by TEM analysis for the hard corona samples (NP_{HC}) and the control sample of naked NPs (NP). Half the difference ($\Delta/2$) is compared to the diameter of the free protein in solution derived by the relation to chain length (N) for globular proteins or IDPs depending on the type of protein. DLS measurements are also reported. The value are expressed in nm

TEM grids. Anyway, the hard corona thickness is consistent with a monolayer of bound molecules also for IDPs. The conformation of the globular proteins and of the IDPs inside the hard corona was further analyzed by CD and FTIR.

3.3.2 Secondary structure by CD

The hard corona samples were analysed by far-UV CD in PBS buffer, in order to determine protein secondary structure in the adsorbed state and the results are reported in figure 3.21.

The red line represents the results for each hard corona sample, which is compared to the original protein solution (black line) and to the negative control (blue line). The negative control corresponds to a sample in which the protein has been subjected to the same steps as the hard corona sample, in the absence of NP. For better comparison, the spectra have been normalized by the maximum of the intensity . The insets show the difference spectra, calculated by the difference between the hard corona spectra and the original protein spectra (red line minus black line).
The presence of CD protein signals in the final hard corona sample depends on the presence of NPs (the negative control does not return any CD protein signals). Thus, the signal can be ascribed to NP-bound protein exclusively.

The shape of the CD spectra of the adsorbed proteins reported in figure 3.21 are similar to the reference spectra of the original solutions for lysozyme, Sic1$^{\Delta 214}$-His$_6$ and holo-Tf, suggesting that no major conformational changes take place during formation of the hard corona. For α-casein and α-synuclein, a shift of the absolute minimum towards higher wavelengths and appearance of a shoulder around 222 nm is observed for the bound protein compared to the reference. Apo-Tf inside the hard corona displays different spectral features relative to the free

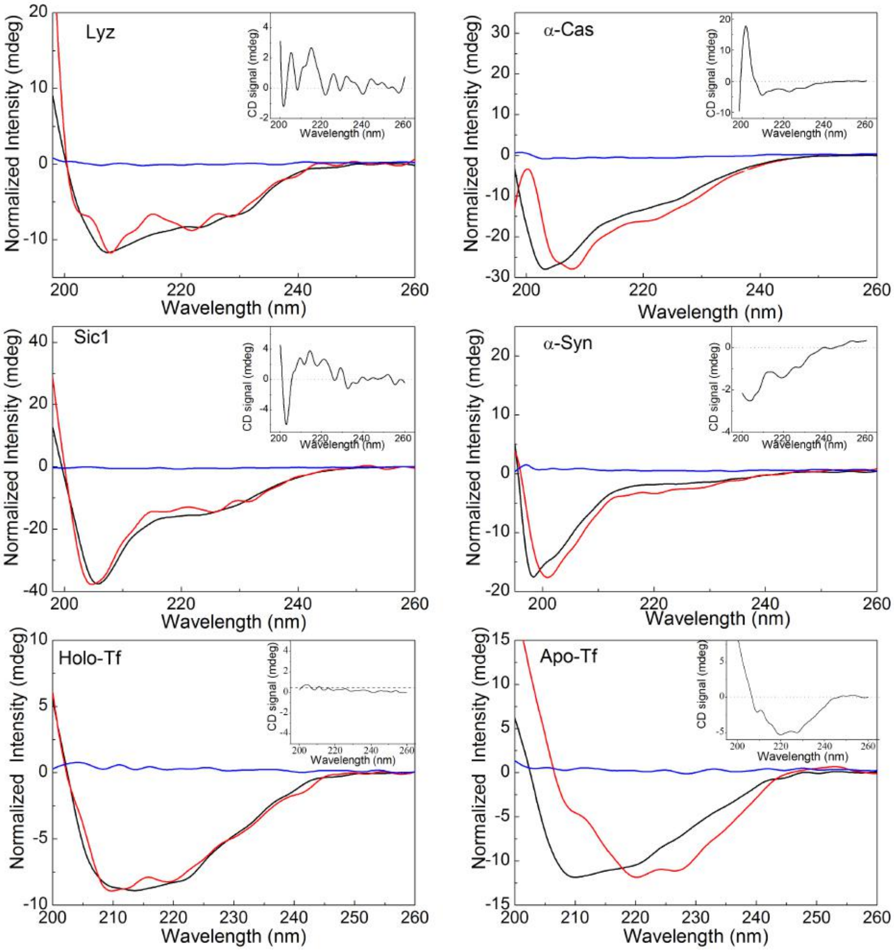

Figure 3.21: *Far-UV CD spectra.* Representative, normalized by maximal intensity, results reported for each hard corona sample (red), in comparison to the original protein solution (black) and the negative control (blue), in which the protein has been subjected to the same steps as the hard corona sample, in the absence of NPs. The insets show the difference spectra (hard corona minus free protein). α-Cas, α-casein; α-Syn, α-synuclein; Lyz, lysozyme; Sic1, Sic1$^{\Delta214}$-His$_6$.

protein, with a broad single minimum around 220 nm rather than the double minimum at 222 and 208 nm.

These changes are highlighted by the difference spectra in the insets of figure 3.21. In the case of α-casein and α-synuclein a typical α-helix profile is obtained. Thus, an increase of the helix component results from adsorption of these proteins. It is worth noting that this effect recalls the membrane effect on α-synuclein. These results suggest that the interaction with SiO_2 NPs induces formation of helical segments in these IDPs.
For apo-Tf, the difference spectrum suggest the features of a β-structure, with a minimum around 225 nm. This result indicates that the apoprotein undergoes a major conformational transition while binding to the NPs, characterized by α-to-β conversion. This evidence also suggests that iron contributes to the Tf structure stability, since the holo-Tf largely maintains its secondary structure.

Finally, the raw far-UV CD spectra normalized by the protein concentration and protein length indicates a general important losses of signal intensity throughout the entire wavelength range (data shown in figure A.1, Appendix A). This behaviour is probably ascribable to sample aggregation and scattering [221]. Indeed, this effect is more pronounced for lysozyme and $Sic1^{\Delta214}$-His_6, which are the samples that aggregate the most.

The quantitative estimates of secondary-structure composition by CD are normally critically connected to precise estimates of protein concentration, which is not straightforward for bio-nanoconjugates. In this case, it is still useful considering qualitative spectral features of the collected CD spectra. Thus, since the presence of aggregation and scattering make the quantitative interpretation of CD spectra intricate, the results have been complemented by FTIR measurement. This technique is less affected by aggregation and scattering phenomena, being very sensitive to protein conformational changes [51] also in the presence of these events. Here, FTIR has been used for further precise secondary-structure investigation of the bound protein. As summarized in the introduction of this chapter, FTIR has already been successfully applied to the investigation of the protein corona, on several different proteins and NPs [51, 52, 222–224]. In particular, data collected after H/D exchange permit the discrimination of the contributions of α-helix and random coil, which otherwise overlap in FTIR spectra [217, 225].

3.3.3 Secondary structure by FTIR Spectroscopy

For a more detailed analysis of the NP-bound protein secondary-structure composition, the samples were investigated by FTIR microspectroscopy [214, 217, 225]. As anticipated, compared to CD, FTIR spectroscopy is less affected by the light-scattering phenomena induced by sample aggregation. Therefore, this technique is particularly suited to the investigation of nanoconjugate structure [221, 226, 227]. Furthermore, second-derivative analysis of the collected FTIR spectra allows the direct determination of the distinct secondary-structure components and the quantitative assessment of spectral changes. This is possible after the normalization over the area of the Amide I band, which is is mainly due to the stretching vibration of backbone carbonyls and, thus, offers an internal reference for the total protein content of the samples. For this reasons, the absorption spectra have been normalized at the Amide-I band area, to compensate for possible differences in the protein content.

Figure 3.22 reports the FTIR data for all the samples considered and compares the free protein, represented by the black line, and the protein constituting the hard corona, represented by the red line. The absorption spectra of the dehydrated protein film is reported on the left panel, while the absorption and second-derivate spectra of the D_2O-rehydrated protein film are reported respectively in the middle and right panels.

The absorption spectra of the dehydrated and D_2O-rehydrated protein films display minor differences in the Amide I region, which can be better evaluated and interpreted by the second-derivative analysis.
In every following subsection, an interpretation of each systems is reported.

Secondary structure of the adsorbed Lysozyme

In the case of lysozyme, the free protein displays the typical peaks of α and β structures, according to previous assignments [228]. These peaks are clearly altered in the second-derivative spectrum of the hard corona, with a remarkable reduction of the α-helical content. This result is indicative of structural perturbation of the protein in hard corona, with loss of helical segments. This finding is consistent with previous analyses of lysozyme showing a consistent perturbation of the native protein structure inside the hard corona [51, 229].

Secondary structure of the adsorbed α-Casein

α-Casein does not show induced conformational changes by FTIR, even by the analysis of the second-derivative spectra. The spectra are dominated by the peak at 1644 cm^{-1}, which can be assigned to disordered structures [217, 225]. In contrast, minor conformational changes are detected by CD, as illustrated above. This discrepancy can be due to the difference in the molecular properties giving rise to CD and Amide-I FTIR signals, which respectively are related to the far-UV electronic transitions of the peptide bond and to the stretching vibration of the CO group. The different molecular properties involved in the measure, together with the different sensitivity of the methods towards the changes

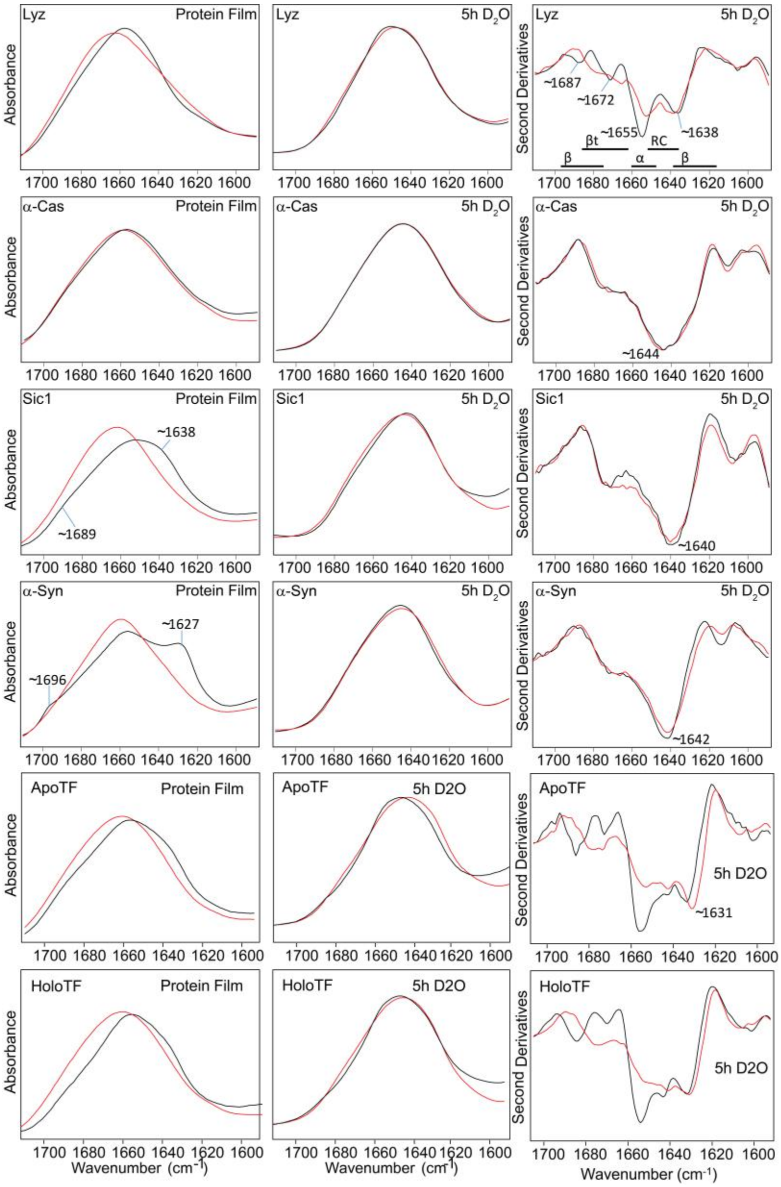

Figure 3.22: *FTIR spectra in the Amide I band.* Representative results are shown for each hard corona sample (red line), in comparison to the original protein solution (black line). The absorption spectra of the dehydrated protein film (left panel) and the absorption and second-derivate spectra of the D_2O-rehydrated protein film (middle and right panels) are shown. Absorption spectra have been normalized at the Amide-I band area. The peak position of selected spectral components is indicated. α-Cas, α-casein; α-Syn, α-synuclein; Lyz, lysozyme; Sic1, Sic1$^{\Delta 214}$-His$_6$; Holo-Tf, holotransferrin; Apo-Tf, apotransferrin. This figure is reproduced with kind permission of Antonino Natalello.

in secondary structure can affect the resulting spectra. Thus, it is possible that minor structural perturbations are detected by only one of the two methods, although both probing protein secondary structure.

Secondary structure of the adsorbed Sic1$^{\Delta 214}$-His$_6$

The Sic1$^{\Delta 214}$-His$_6$ spectra reported in the panel of the protein film suggest that the free protein acquires ordered β structure after the formation of the protein film by dehydration. This observation is supported by the appearance of Amide I shoulders at ~1638^{-1} and 1689 cm^{-1}, which is the spectral range where both intra- and intermolecular β-sheets can adsorb [217, 225]. The observed transition does not take place in the NP-bound protein suggesting that conformational changes due to solvent evaporation are prevented in the case of adsorbed protein. Finally, upon rehydration in D_2O, the free protein reverts to the typical spectrum of Sic1$^{\Delta 214}$-His$_6$ in bulk solutions [201] with a broad minimum in the second derivative at ~1640 cm^{-1}, assigned to random-coil structures [200, 201, 217, 225].

Secondary structure of the adsorbed α-Synuclein

α-Synuclein displays a behaviour similar to Sic1$^{\Delta 214}$-His$_6$, with a strong effect induced by dehydration on the free protein. The positions of the induced bands at ~1627 cm^{-1} andat ~1696 cm^{-1} are characteristic of intermolecular β-sheets [217, 225], indicating that the process is mediated by protein aggregation.

Analogously to Sic1$^{\Delta 214}$-His$_6$, conformational changes elicited by solvent evaporation are prevented inside the hard corona, suggesting that bound protein molecules impede the protein-protein interactions, probably by either extensive contacts with NPs and/or structural/topological constraints. Also for α-synuclein, rehydration in D_2O restores the typical solution spectrum [216] with a broad minimum in the second derivative at ∼1642 cm^{-1}, assigned to random-coil structures [216, 217, 225]. A minor shift of the main second-derivative peak of the bound protein is observed. This effect could be ascribed to the formation of either β structures or hydrated helices inside the hard corona [230]. According to the CD spectra reported in figure 3.21, which suggests the acquisition of α-helix structure, we assign these spectral changes to a partial coil-to-helix transition with the formation of bifurcated H-bonds involving backbone atoms and water molecules [230].

Secondary structure of the adsorbed holo- and apo-Tf

The free proteins displays the typical peaks of α and β structures. These peaks are clearly altered in the second derivative spectra of the hard coronas, with a remarkable decrease in the α-helical component, as indicated by the band at ∼1655 cm^{-1} and an increase in β-sheet/β-turn content as indicated by the signals at ∼1680 cm^{-1} and ∼1670 cm^{-1}. Additionally, for the apoprotein only, the increase of the peak at ∼1631 cm^{-1} indicates a more remarkable increase in the β-structure component. These results confirm the observations from CD and indicate that non-native β structure is formed upon apo-Tf binding to the NP surface. Thus, although apo- and holo-Tf have the same structure in solution, the formation of the hard corona induces major structural rearrangements in the apoprotein, characterized by α-to-β conversion, likely due to a reduced conformational stability in the absence of bound metal.

3.3.4 Effect of NPs on α-synuclein aggregation

The effect of SiO_2 NPs on α-synuclein aggregation to form amyloid fibrils has been investigated. The experiments were performed in collaboration with Prof. Giuseppe Legname, Laboratory of Prion Biology, Trieste, Italy.

The aggregation of the unstructured α-synuclein protein may be linked to the pathogenesis of Parkinson's disease [194]. Here, we tested how SiO_2 NPs affect the aggregation of α-synuclein in vitro.

Generally, the aggregation of α-synuclein follows a nucleation-dependent polymerization profile, composed of an initial lag phase, where no fibrils are detected, an exponential phase where fibril concentration rapidly increases, and a final plateau phase. The aggregation process can be monitored in real time by Thioflavin T (ThT) fluorescence enhancement upon binding to amyloid fibrils. Practically, the ThT Assay measures changes in fluorescence intensity of ThT upon binding to amyloid fibrils. The enhanced fluorescence can be observed by fluorescence microscopy or by fluorescent spectroscopy.

Contrasting data on the effect of NPs on the aggregation process of amyloidogenic proteins have been reported. It has been shown that NPs of various nature, including gold and polystyrene, enhance α-synuclein fibrils formation in vitro [166, 231]. Moreover, in vivo studies have shown the induction of α-synuclein aggregation in PC12 cells after exposure to SiO_2 and titanium dioxide NPs [232, 233]. On the contrary, different generations of PAMAM dendrimers inhibited α-synuclein aggregation in vitro [234, 235]. Similarly, gold NPs inhibit aggregation of HSA [67].

The aggregation reactions were performed in the presence of increasing NPs concentrations at constant α-synuclein concentration.

Figure 3.23 reports the results of the ThT assay. In the absence of NPs, the aggregation followed the expected [210] nucleation-dependent kinetics, with a lag phase of about 6 hours. The presence of increasing concentrations of NPs promoted aggregation by boosting the kinetics and shortening the lag phase apparently to complete suppression. These results indicate that NPs exert a major influence on the onset of the aggregation process and fibril-elongation kinetics. These effects display a clear concentration dependence on NPs concentration(figure 3.23).

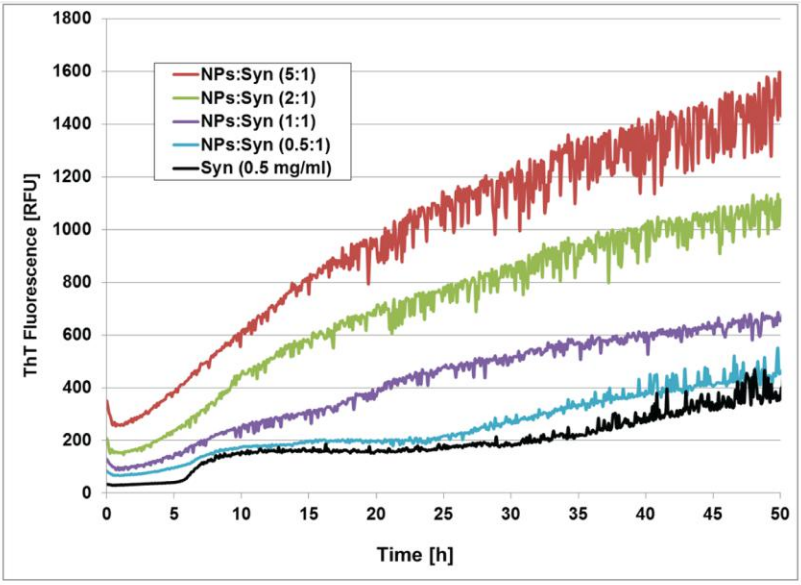

Figure 3.23: *Effect of NPs on the aggregation kinetics of α-synuclein.* ThT fluorescence signal is reported as a function of incubation time, for 0.5 mg/mL α-synuclein samples in the presence of increasing concentrations of NPs (black, 0 mg/mL; red, 2.5 mg/ml; green, 1 mg/mL; purple, 0.5 mg/mL; blue, 0.25 mg/mL). Each curve represents the mean of four replicates.

This result supports previous data suggesting that NPs may promote the nucleation process, accelerating the rate of fibril formation by locally increase protein concentration. As shown in the previous section, α-synuclein inside hard corona does not increase its β structures when adsorbs onto NP surface. Thus, the mechanism does not seem to be the direct stabilization of an amyloidogenic conformer by the NP surface [236]. Indeed, an indirect effect involving the soft corona seems to plays a key role in promoting amyloid aggregation.

3.3.5 Spectroscopic properties of transferrin hard corona

Tb^{3+} complex of the iron-transport protein transferrin

Tb^{3+} is often selected as a luminescent label for proteins because its emission can be easily sensitised by energy transfer (Fluorescence Resonance Energy Transfer) from the intrinsic protein fluorophores of the aromatic amino acids, tyrosine, tryptophan, and phenylalanine [173]. The efficiency of this transfer in Tb^{3+}–protein complexes depends on the distance between the sensitising amino acid and the coordinated metal ion. However, when Tb^{3+} is directly co-ordinated to a tyrosinate residue, highly efficient sensitisation of the lanthanide ion emission takes place. Tf binds much more weakly to lanthanide ions than to Fe^{3+} (by a factor of ca. log K = 13.24 [173]).

In general, Tb^{3+} luminescence is characterised by seven narrow emission bands at ca. 490, 545, 585, 623, 651, 670, and 681 nm corresponding to transitions from the $^5D_4$ excited state to the $^7F_6$, $^7F_5$, $^7F_4$, $^7F_3$, $^7F_2$, $^7F_1$ and the $^7F_0$ components of the ground states, respectively [173].

Here, the Tb-Tf complexes were formed by incubating the apo-Tf (25 μM) with an excess of $TbCl_3$ (3mM) in AAB buffer.

Figure 3.24 shows emission spectra of 25 μM apo-Tf, with and without 3 Mm $TbCl_3$ and of the Tb^{3+} at an excitation wavelength of 295 nm (which matches an absorption maximum of the protein). Apo-Tf (figure 3.24 a)) shows one broad emission band centred at 330 nm, attributed to the fluorescence of the aromatic amino acids. The excitation of the $TbCl_3$ solution at 350 nm results in the two characteristic Tb peak at 490 nm at 545 nm (figure 3.24 b)). The formation of the Tf-Tb complex is detected upon excitation at 295 nm (figure 3.24 c)) by the two transitions at 490 nm at 545 nm in the presence of $TbCl_3$. Transition at 490 nm is split into two minor peaks, as a consequence of metal complexation by the protein [173]. This emission profile matches that previously reported

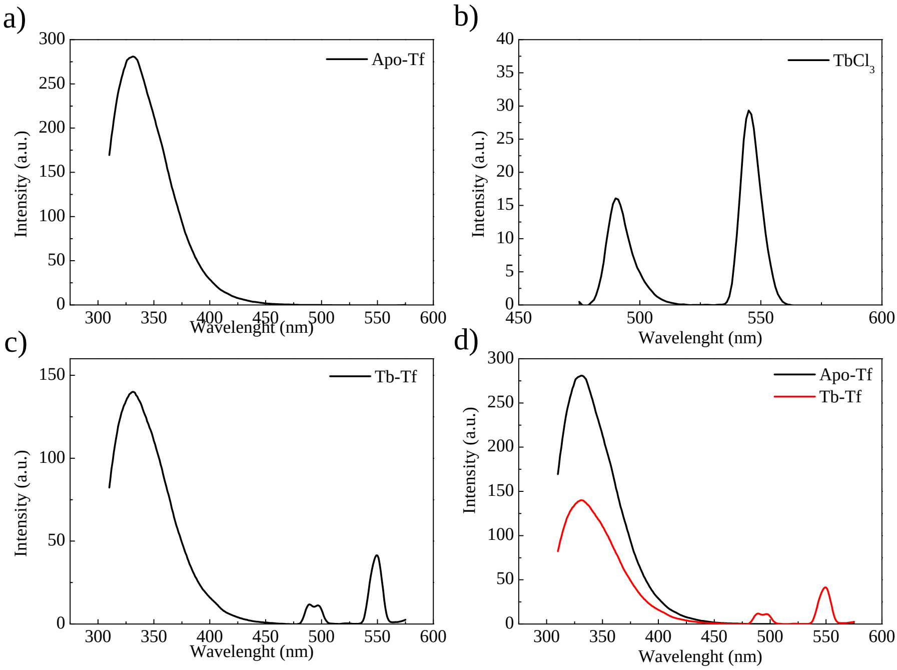

Figure 3.24: *Fluorescence emission spectra of the analysed samples.* a) 25 μM apo-Tf, excitation wavelength 295 nm; b) 10 mM $TbCl_3$ excitation wavelength 350 nm; c) Tb-Tf complex, excitation wavelength 295 nm; d) comparison of apo-Tf in presence and absence of Tb (red and black respectively).

one for Tb^{3+}-Tf complexes [173]. Figure 3.24 d) show the comparison between the apo-Tf and Tb-Tf. The protein fluorescence intensity at 330 nm decreased as Tb^{3+} was added to Tfr. Concluding, it is interesting to note that despite the extremely high concentration of Tb^{3+} in solution, the unbound Tb excess does not generate any signal since the excitation wavelength does not correspond to a maximum in absorption of Tb.

Effects of metal binding on Tf hard corona on SiO_2 NPs

The ability of Apo-Tf to bind Tb inside the hard corona was investigated. For this purpose, the same excess of $TbCl_3$ (3 mM) was added to the already formed Apo-Tf hard corona. The hard corona samples were prepared in AAB buffer and the fluorescence emission after excitation at 295 nm was measured.

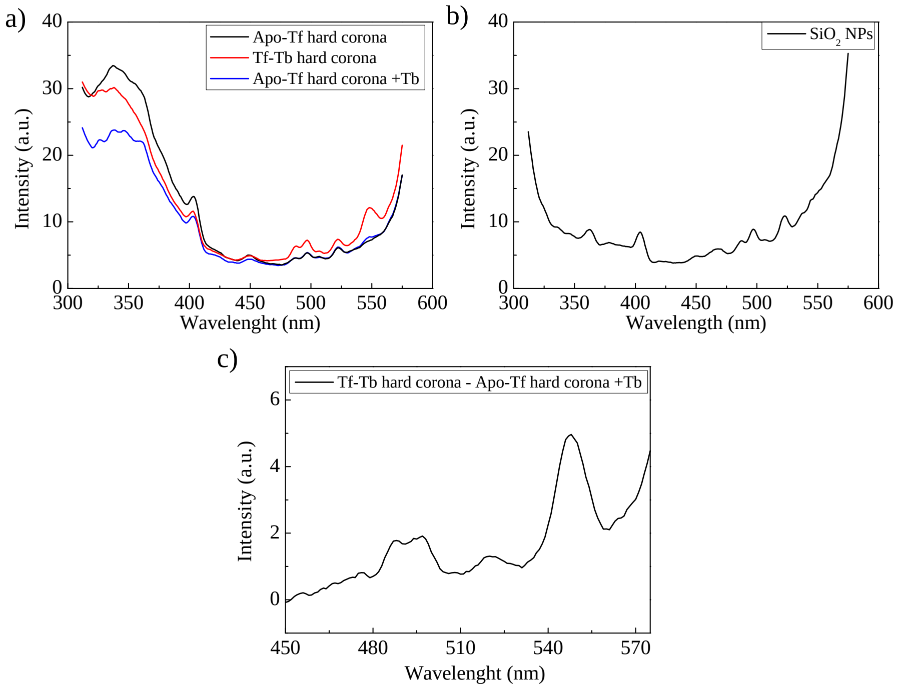

Figure 3.25: *Fluorescent emission spectra of the analysed sample after excitation at 295 nm.* a) Black line: Tb-free Apo-Tf hard corona (Apo-Tf hard corona); red line: hard corona with the already formed Tb-Tf complexes (Tb-Tf hard corona); blue line: Apo-Tf hard corona + Tb(III); b) NPs fluorescent emission spectra; c) Difference spectra between the Tb-Tf hard corona and the Apo-Tf hard corona (red line minus blue line).

The Tb fluorescence emission at 549 nm is clear in the case of the pre-formed Tb-Tf hard corona (red line in Figure 3.25 a)). This peak is absent in negative control of apo-Tf hard corona (black line figure 3.25 a)). To the same Apo-Tf hard corona, $TbCl_3$ (3 mM) was added and the fluorescence emission evaluated (blue line in Figure 3.25 a)). The appearance of a peak at 549 nm indicates that Tb binds to Apo-Tf even when it is already bound to the NPs. However, the intensity of the peak is not comparable to the intensity of the Tb peak in the case of the Tb-Tf hard corona. This difference might be related to the reported conformational rearrangement of the apoprotein inside the hard corona and/or a reduce accessibility to the metal binding sites. The peak at ∼489, which is present in all spectra, origins from NPs, as indicated by the fluorescent emission spectra under the same conditions reported in figure 3.25 b). Thus apo-Tf can still bind Tb after hard corona formation, but with less apparently affinity.

Finally, Figure 3.25 c) reports the difference spectra between the emission spectra of the Tb-Tf hard corona obtained by later addition of Tb and the apo-Tf hard corona. The characteristic Tf-bounded Tb^{3+} peak are clearly visible at the 590 nm and 448 nm. It is interesting to note that, although Tb^{3+} affinity is much lower than Fe^{3+}, the complex is maintained throughout the four washing cycles performed during preparation of the hard corona samples ((red line figure 3.25 a)). Tb^{3+}-bound Tf largely maintain its fluorescent properties also when adsorbed on NP surface. In conclusion, the Tb-Tf complex reconstitution should precede the formation of the hard corona to obtain a native like structure and good fluorescence properties.

Chapter 4

General Conclusion

In the first part of this thesis dissertation it is reported a simple but efficient and reliable protocol to study the formation and the evolution of the NP-protein corona heading towards the formation of the stable hard corona in physiological media. Here, proteins form transient complexes with NPs, which are mediated by competitive binding between proteins and NP surfaces, leading to the formation of the hard protein corona.

- short incubation time leads to absorption of loosely bound proteins, which are easily removed by centrifugation, resulting in NP aggregation. As incubation time get longer, due to the hardening of the protein corona, protein stably attach to the NP surface affecting centrifugation-induced aggregation. Adsorption of HS proteins and HSA results in stabilization, while IgG adsorption onto the NP surface promotes NP aggregation under the same tested experimental conditions.
- The time evolution of the protein corona in the case of the conjugation with only one specific protein, i.e. NPs incubated with only HSA or only IgG, can be understood as a fingerprint of the adsorption of that specific protein. The kinetic evolution of the protein corona deriving from incubation with HS reveals the physicochemical dominance of the HSA, with some minor difference probably

connected to the presence of minor compounds in the HS hard corona. MALDI-TOF confirmed that the resulting HS hard corona is albumin-rich.

- The resulting HS and HSA hard corona are stable entities which maintain their conjugation properties over time, at least up to three days.
- Digestion experiments, by exposing the HS and HSA hard corona samples to strong etching agent NaCN and to the strong acidic condition of the HNO_3, indicate that the protein layer protect the NPs surface, preventing either dissolution of the metal core or NPs aggregation. As a result, both hard corona exhibits enhanced biocompatibility as effect of the presence of the protein layer, although HSA hard corona is found to be more protective against the NaCN etching.
- Limited proteolysis of the hard protein corona indicates altered degradation of protein constituting the hard protein corona with respect to the free protein, probably related to an altered and more static conformation in the adsorbed state
- Different experimental parameters, such as temperature, buffer composition and the related protein stability, affect the time evolution of the protein corona, as well as the resulting hard corona.

The NPs surface effect on protein structure and functionality is discussed in the second part of the thesis . In particular the conformational response of IDPs has been investigated in comparison to lysozyme as a model of globular protein. Additionally, the structural and spectroscopic features of transferrin inside the hard corona as a model globular protein have been further investigated.

- CD and FTIR analyses show that IDPs adsorb onto silica NP preserving their high degree of structural disorder, with a light increase in ordered secondary structure content. On the contrary, lysozyme inside the protein corona tends to loose some secondary structure upon adsorption to NP surfaces, with reduction of helical content and formation of unstructured regions.

- FTIR experiments showed that bound proteins are stabilized against further conformational transitions, such as those induced by dehydration, observed instead in their respective free forms.

- NP enhance α-synuclein aggregation propensity since structure acquired in the hard corona is helical rather than β-type structure. Probably the soft corona plays a role in promoting and modulating amyloid aggregation, by increasing local protein concentration.

- Upon binding to the NP surface, metal-free Tf changes its conformation acquiring β structure. On the contrary, the holo-Tf mainly conserve it structure, suggesting that metal plays an important role in maintaining the secondary protein structure.

- The Tb-Tf complex maintains its fluorescent properties upon adsorption onto NP surface, indicating that the protein keeps the metal bound even during the preparation of the hard corona. On the contrary, a significant loss of Tb binding capacity is observed when Tf is already immobilized on the NPs. This can be attributed to the partial structural loss when the protein is adsorbed in the NPs.

For all the characterized proteins, the development of experimental methodologies to investigate the effect of these reported structural changes on their activity, is needed. In particular, the investigation of the cellular uptake of the NP-Tf complexes through the specific recognition by the Tf receptor, over-expressed in cancer cells, will open attractive approach on the cancer treatment by targeted drug delivery methods.

Summarizing, inorganic NPs surfaces have strong affinity for proteins. This strong affinity can compensate the destabilization forces that colloidal NPs experience in high-ionic-strength media and help to stabilize them. This interaction is immediate but evolves with time. Moreover, this evolution affects the pharmakokinetis and biodistribution of NPs, which ultimately defines their potential therapeutic effect and toxicity. The protein-NP surface interaction leads to protein structure reorganization inside the hard corona.

In this work, I investigated the consequences of NP protein corona formation providing a simple and reliable approach for biochemical, biophysical and physicochemical characterization of the hard corona, including implication for protein structures. Finally, it is worth to note that the interactions of NP and proteins in physiological media offer a unique opportunity to mimic interactions with biological partners. The fast development of biophysical approaches for the investigation of protein-NP interactions will provide crucial information for improved drug delivery by targeting nanoparticle, and resolution of the potential threat of nanotechnological devices to organisms and environment.

Appendix A

Raw data from far-UV CD

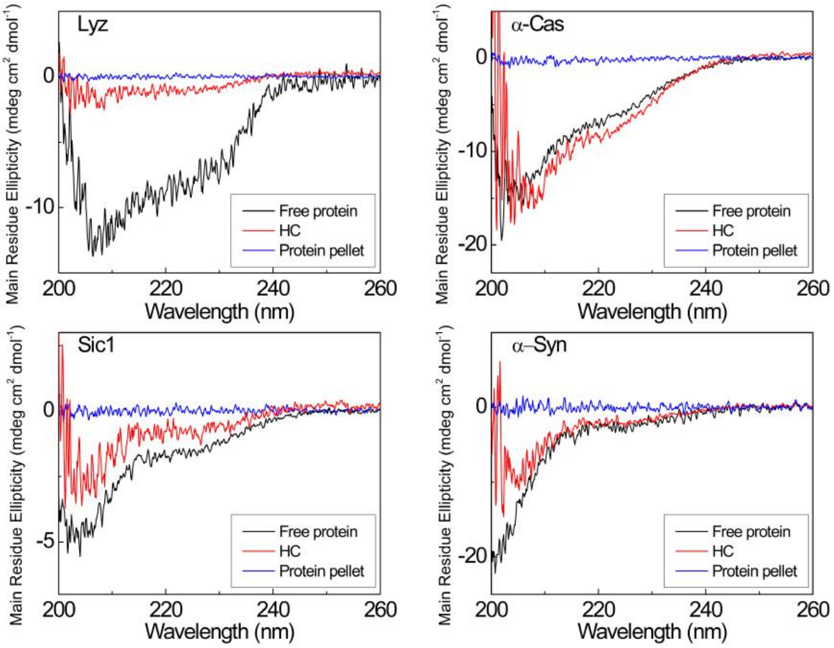

Figure A.1: *Far-UV CD spectra-raw data*. Representative results are reported for each hard corona sample (red), in comparison to the original protein solution (black) and the negative control (blue), in which the protein has been subjected to the same steps as the hard corona sample, in the absence of NPs. The spectra have been normalized by the protein concentration and protein length (mean residue ellipticity). α-Cas, α-casein; α-Syn, α-synuclein; Lyz, lysozyme; Sic1, Sic1$^{\Delta 214}$-His$_6$. Consistent with aggregation and scattering phenomena, the effect of loss of signal intensity is more pronounced for the two proteins that aggregate the most, lysozyme and Sic1$^{\Delta 214}$-His$_6$, based on DLS consideration.

Appendix B

List of publications

1. **Michele Vitali**, Francesco Barbero, Lorenzo Russo, Jordi Piella, Ignacio Salvo, Mireya L. Borrajo, Marti Busquets-Fité, Rita Grandori, Neus G. Bastús, Eudald Casals, Victor Puntes; *Formation of the Protein Corona: The Interface between Nanoparticles and the Immune System*, Seminars in Immunology, Volume 34, 2017, Pages 52-60.
2. **Michele Vitali**, Antonino Natalello, Valentina Rigamonti, Barbara Colzani, Svetlana Avvakumova, Stefania Brocca, Carlo Santambrogio, Joanna Narkiewicz, Giuseppe Legname, Miriam Colombo, Davide Prosperi, Rita Grandori; *Conformational properties of intrinsically disordered proteins bound to the surface of silica nanoparticles*. Submitted to BBA - General Subjects.
3. Valentina Rigamonti, **Michele Vitali**, Antonino Natalello, Carlo Santambrogio, Davide Prosperi and Rita Grandori, *Effects of metal binding on transferrin hard corona on silica nanoparticles*. In preparation

Bibliography

[1] Eudald Casals et al. “Distribution and potential toxicity of engineered inorganic nanoparticles and carbon nanostructures in biological systems”. In: *TrAC - Trends in Analytical Chemistry* 27.8 (2008), pp. 672–683.

[2] Eudald Casals, E Gonzalez, and Victor Franco Puntes. “Reactivity of inorganic nanoparticles in biological environments: insights into nanotoxicity mechanisms”. In: *Journal of Physics D: Applied Physics* 45.44 (2012), p. 443001.

[3] A. Paul Alivisatos. “Less is more in Medicine”. In: *Scientific American* 285.3 (2001), pp. 66–73.

[4] Tian Xia et al. “Decreased Dissolution of ZnO by Iron Doping Yields Nanoparticles with Reduced Toxicity in the Rodent Lung and Zebrafish Embryos”. In: *ACS Nano* 5.2 (2011), pp. 1223–1235.

[5] Renyuan Li, Lianbin Zhang, and Peng Wang. “Rational design of nanomaterials for water treatment”. In: *Nanoscale* 7.41 (2015), pp. 17167–17194.

[6] David E Cliffel, Brian N Turner, and Brian J Huffman. “Nanoparticle-based biologic mimetics.” In: *Wiley interdisciplinary reviews. Nanomedicine and nanobiotechnology* 1.1 (2009), pp. 47–59.

[7] F J Lázaro et al. “Magnetic characterisation of rat muscle tissues after subcutaneous iron dextran injection”. In: *Biochimica et Biophysica Acta - Molecular Basis of Disease* 1740.3 (2005), pp. 434–445.

[8] Ling Yang and Daniel J. Watts. "Particle surface characteristics may play an important role in phytotoxicity of alumina nanoparticles". In: *Toxicology Letters* 158.2 (2005), pp. 122–132.

[9] Christian Kirchner et al. "Cytotoxicity of colloidal CdSe and CdSe/ZnS nanoparticles". In: *Nano Letters* 5.2 (2005), pp. 331–338.

[10] *NSF and EPA Establish Two Centers for Environmental Implications of Nanotechnology | NSF - National Science Foundation*. URL: `https://www.nsf.gov/news/news{\_}summ.jsp?cntn{\_}id=112234`.

[11] Eudald Casals et al. "Cancer resistance to treatment and antiresistance tools offered by multimodal multifunctional nanoparticles". In: *Cancer Nanotechnology* 8.1 (2017).

[12] Beatriz Pelaz et al. "The state of nanoparticle-based nanoscience and biotechnology: Progress, promises, and challenges". In: *ACS Nano* 6.10 (2012), pp. 8468–8483.

[13] Li Shang, Karin Nienhaus, and Gerd Nienhaus. "Engineered nanoparticles interacting with cells: size matters". In: *Journal of Nanobiotechnology* 12.1 (2014), p. 5.

[14] Francesco Barbero et al. "Formation of the Protein Corona : The Interface between Nanoparticles and the Immune System". In: *Seminars in Immunology* September (2017), pp. 0–1.

[15] Iseult Lynch, Anna Salvati, and Kenneth A. Dawson. "Protein-nanoparticle interactions: What does the cell see?" In: *Nature Nanotechnology* 4.9 (2009), pp. 546–547.

[16] Andre Nel. "Toxic Potential of Materials at the Nanolevel". In: *Science* 311.5761 (2006), pp. 622–627.

[17] Jukka Sund et al. "Proteomic Characterization of Engineered Nanomaterial–Protein Interactions in Relation to Surface Reactivity". In: *ACS Nano* 5.6 (2011), pp. 4300–4309.

[18] Gabriele Maiorano et al. “Effects of Cell Culture Media on the Dynamic Formation of Protein-Nanoparticle Complexes and Influence on the Cellular Response”. In: *ACS Nano* 4.12 (2010), pp. 7481–7491.

[19] Martin Lundqvist et al. “Nanoparticle size and surface properties determine the protein corona with possible implications for biological impacts.” In: *Proceedings of the National Academy of Sciences of the United States of America* 105.38 (2008), pp. 14265–70.

[20] Sílvia A. Ferreira et al. “Biocompatibility of mannan nanogel - Safe interaction with plasma proteins”. In: *Biochimica et Biophysica Acta - General Subjects* 1820.7 (2012), pp. 1043–1051.

[21] Marina A. Dobrovolskaia et al. “Interaction of colloidal gold nanoparticles with human blood: effects on particle size and analysis of plasma protein binding profiles”. In: 5.2 (2009), pp. 106–117.

[22] Tommy Cedervall et al. “Understanding the nanoparticle-protein corona using methods to quantify exchange rates and affinities of proteins for nanoparticles”. In: *Proceedings of the National Academy of Sciences* 104.7 (2007), pp. 2050–2055.

[23] Tommy Cedervall et al. “Detailed identification of plasma proteins adsorbed on copolymer nanoparticles”. In: *Angewandte Chemie - International Edition* 46.30 (2007), pp. 5754–5756.

[24] Carl D. Walkey et al. “Nanoparticle size and surface chemistry determine serum protein adsorption and macrophage uptake”. In: *Journal of the American Chemical Society* 134.4 (2012), pp. 2139–2147.

[25] Stefan Tenzer et al. “Nanoparticle size is a critical physicochemical determinant of the human blood plasma corona: A comprehensive quantitative proteomic analysis”. In: 5.9 (2011), pp. 7155–7167.

[26] Marco P. Monopoli et al. "Biomolecular coronas provide the biological identity of nanosized materials." In: *Nature nanotechnology* 7.12 (2012), pp. 779–86.

[27] Andre E. Nel et al. "Understanding biophysicochemical interactions at the nano–bio interface". In: *Nature Materials* 8.7 (2009), pp. 543–557.

[28] Thomas A. Horbett and John L. Brash. *Proteins at Interfaces II, Copyright, 1995 Advisory Board, Foreword*. 1995, pp. 41–51.

[29] William J. Gradishar et al. "Phase III Trial of Nanoparticle Albumin-Bound Paclitaxel Compared With Polyethylated Castor Oil–Based Paclitaxel in Women With Breast Cancer". In: *Journal of Clinical Oncology* 23.31 (2005), pp. 7794–7803.

[30] Bruce Alberts et al. *Molecular biology of the cell*. Garland Science, 2002.

[31] Vladimir N. Uversky, Christopher J. Oldfield, and A. Keith Dunker. "Intrinsically Disordered Proteins in Human Diseases: Introducing the D2 Concept". In: *Annual Review of Biophysics* 37.1 (2008), pp. 215–246.

[32] Vladimir N. Uversky. *Intrinsically disordered proteins and their environment: Effects of strong denaturants, temperature, pH, Counter ions, membranes, binding partners, osmolytes, and macromolecular crowding*. 2009.

[33] Vladimir N Uversky et al. "Length-dependent compaction of intrinsically disordered proteins". In: *FEBS Letters* 586.1 (2011), pp. 70–73.

[34] Pietro Sormanni et al. "Simultaneous quantification of protein order and disorder". In: *Nature Chemical Biology* 13.4 (2017), pp. 339–342.

[35] Stephanie Ghio et al. "Interaction of α-synuclein with biomembranes in Parkinson's disease role of cardiolipin". In: *Progress in Lipid Research* 61 (2016), pp. 73–82.

[36] J Dunbar et al. "The effect of denaturants on protein structure." In: *Protein science : a publication of the Protein Society* 6.8 (1997), pp. 1727–33.

[37] Dorota Walczyk et al. "What the Cell "Sees" in Bionanoscience". In: *Journal of the American Chemical Society* 132.16 (2010), pp. 5761–5768.

[38] Eudald Casals et al. "Time evolution of the nanoparticle protein corona". In: *ACS Nano* 4.7 (2010), pp. 3623–3632.

[39] Parag Aggarwal et al. "Nanoparticle interaction with plasma proteins as it relates to particle biodistribution, biocompatibility and therapeutic efficacy". In: *Advanced Drug Delivery Reviews* 61.6 (2009), pp. 428–437.

[40] Marco P. Monopoli et al. "Physical-Chemical aspects of protein corona: Relevance to in vitro and in vivo biological impacts of nanoparticles". In: *Journal of the American Chemical Society* 133.8 (2011), pp. 2525–2534.

[41] Morteza Mahmoudi et al. *Protein-nanoparticle interactions: Opportunities and challenges*. 2011.

[42] Liwen Li et al. "Analytical strategies for detecting nanoparticle-protein interactions". In: *The Analyst* 135.7 (2010), p. 1519.

[43] Blair D Johnston et al. "Colloidal Stability and Surface Chemistry Are Key Factors for the Composition of the Protein Corona of Inorganic Gold Nanoparticles". In: *Advanced Functional Materials* 27.42 (2017), p. 1701956.

[44] Eudald Casals et al. "Hardening of the nanoparticle-protein corona in metal (Au, Ag) and oxide (Fe 3O 4, CoO, and CeO 2) nanoparticles". In: *Small* 7.24 (2011), pp. 3479–3486.

[45] Peter M Tessier et al. "Self-Interaction Nanoparticle Spectroscopy: A Nanoparticle-Based Protein Interaction Assay". In: *Journal of the American Chemical Society* 130.10 (2008), pp. 3106–3112.

[46] Vincenzo Amendola et al. “Surface plasmon resonance in gold nanoparticles: a review”. In: *Journal of Physics: Condensed Matter* 29.20 (2017), p. 203002.

[47] Qi Xiao et al. “Conformation, thermodynamics and stoichiometry of {HSA} adsorbed to colloidal CdSe/ZnS quantum dots”. In: *Biochimica et Biophysica Acta ({BBA}) - Proteins and Proteomics* 1784.7-8 (2008), pp. 1020–1027.

[48] Willem Norde and Jan Paul Favier. “Structure of adsorbed and desorbed proteins”. In: *Colloids and Surfaces* 64.1 (1992), pp. 87–93.

[49] Norma J Greenfield. “Using circular dichroism spectra to estimate protein secondary structure.” In: *Nature protocols* 1.6 (2006), pp. 2876–90.

[50] Narasimha Sreerama and Robert W. Woody. *Computation and Analysis of Protein Circular Dichroism Spectra*. 2004.

[51] Süleyman Cinar and Claus Czeslik. “Secondary structure and folding stability of proteins adsorbed on silica particles {\textendash} Pressure versus temperature denaturation”. In: *Colloids and Surfaces B: Biointerfaces* 129 (2015), pp. 161–168.

[52] Emanuela Occhipinti et al. “Investigating the structural biofunctionality of antibodies conjugated to magnetic nanoparticles”. In: *Nanoscale* 3.2 (2011), pp. 387–390.

[53] Helen S Beeston et al. “Changes in protein structure monitored by use of gas-phase hydrogen/deuterium exchange”. In: *Proteomics* 15.16 (2015), pp. 2842–2850.

[54] Ossi Turunen et al. “Engineering the thermotolerance and pH optimum of family 11 xylanases by site-directed mutagenesis”. In: *Methods in Enzymology* 388 (2004), pp. 156–167.

[55] Kyle J.M. Bishop and Bartosz A. Grzybowski. “"Nanoions": Fundamental properties and analytical applications of charged nanoparticles”. In: *ChemPhysChem* 8.15 (2007), pp. 2171–2176.

[56] Risto Cukalevski et al. “IgG and fibrinogen driven nanoparticle aggregation”. In: *Nano Research* 8.8 (2015), pp. 2733–2743.

[57] Shyh Dar Li and Leaf Huang. “Pharmacokinetics and biodistribution of nanoparticles”. In: *Molecular Pharmaceutics*. Vol. 5. 4. American Chemical Society, 2008, pp. 496–504.

[58] Lara K. Bogart et al. “Nanoparticles for imaging, sensing, and therapeutic intervention”. In: *ACS Nano* 8.4 (2014), pp. 3107–3122.

[59] Andrew D. Maynard et al. “Safe handling of nanotechnology”. In: *Nature* 444.7117 (2006), pp. 267–269.

[60] Justin M. Zook et al. “Stable nanoparticle aggregates/agglomerates of different sizes and the effect of their size on hemolytic cytotoxicity”. In: *Nanotoxicology* 5.4 (2011), pp. 517–530.

[61] Wen Shang et al. “Unfolding of ribonuclease a on silica nanoparticle surfaces”. In: *Nano Letters* 7.7 (2007), pp. 1991–1995.

[62] Wen Shang et al. “Cytochrome c on silica nanoparticles: Influence of nanoparticle size on protein structure, stability, and activity”. In: *Small* 5.4 (2009), pp. 470–476.

[63] Martin Lundqvist, Ingmar Sethson, and Bengt Harald Jonsson. “Protein adsorption onto silica nanoparticles: Conformational changes depend on the particles’ curvature and the protein stability”. In: *Langmuir* 20.24 (2004), pp. 10639–10647.

[64] Andrzej S. Pitek et al. “Transferrin coated nanoparticles: Study of the bionano interface in human plasma”. In: *PLoS ONE* 7.7 (2012), e40685.

[65] Risto Cukalevski et al. “Structural changes in apolipoproteins bound to nanoparticles”. In: *Langmuir* 27.23 (2011), pp. 14360–14369.

[66] Xiue Jiang et al. “Effect of colloidal gold size on the conformational changes of adsorbed cytochrome c: Probing by circular dichroism, UV-visible, and infrared spectroscopy”. In: *Biomacromolecules* 6.1 (2005), pp. 46–53.

[67] Sonia Goy-López et al. “Physicochemical characteristics of protein-NP bioconjugates: The role of particle curvature and solution

conditions on human serum albumin conformation and fibrillogenesis inhibition". In: *Langmuir* 28.24 (2012), pp. 9113–9126.

[68] Sergio Dominguez-Medina et al. "In situ measurement of bovine serum albumin interaction with gold nanospheres". In: *Langmuir* 28.24 (2012), pp. 9131–9139.

[69] Wilhelm R. Glomm et al. "Adsorption behavior of acidic and basic proteins onto citrate-coated Au surfaces correlated to their native fold, stability, and pI". In: *Journal of Physical Chemistry B* 111.51 (2007), pp. 14329–14345.

[70] Dongmao Zhang et al. "Gold nanoparticles can induce the formation of protein-based aggregates at physiological pH". In: *Nano Letters* 9.2 (2009), pp. 666–671.

[71] Sugam Kumar, Vinod K. Aswal, and Joachim Kohlbrecher. "SANS and UV-vis spectroscopy studies of resultant structure from lysozyme adsorption on silica nanoparticles". In: *Langmuir* 27.16 (2011), pp. 10167–10173.

[72] Jennifer E. Gagner et al. "Effect of gold nanoparticle morphology on adsorbed protein structure and function". In: *Biomaterials* 32.29 (2011), pp. 7241–7252.

[73] Bhuvnesh Bharti, Jens Meissner, and Gerhard H. Findenegg. "Aggregation of silica nanoparticles directed by adsorption of lysozyme". In: *Langmuir* 27.16 (2011), pp. 9823–9833.

[74] Michaela Kendall, Ping Ding, and Kevin Kendall. "Particle and nanoparticle interactions with fibrinogen: the importance of aggregation in nanotoxicology". In: *Nanotoxicology* 5.1 (2011), pp. 55–65.

[75] Zhou J. Deng et al. "Molecular interaction of poly(acrylic acid) gold nanoparticles with human fibrinogen". In: *ACS Nano* 6.10 (2012), pp. 8962–8969.

[76] Mark A. Wells et al. "Serum proteins prevent aggregation of Fe 2 O 3 and ZnO nanoparticles". In: *Nanotoxicology* 6.8 (2012), pp. 837–846.

[77] Hilda T. R. Wiogo et al. "Stabilization of magnetic iron oxide nanoparticles in biological media by fetal bovine serum (FBS)". In: *Langmuir* 27.2 (2011), pp. 843–850.

[78] Hilda T. R. Wiogo et al. "Insight into serum protein interactions with functionalized magnetic nanoparticles in biological media". In: *Langmuir* 28.9 (2012), pp. 4346–4356.

[79] L. VROMAN. "Effect of Adsorbed Proteins on the Wettability of Hydrophilic and Hydrophobic Solids". In: *Nature* 196.4853 (1962), pp. 476–477.

[80] Masoud. Rahman et al. *Protein-Nanoparticle Interactions The Bio-Nano Interface*. Springer, 2013.

[81] Iseult Lynch and Kenneth A. Dawson. "Protein-nanoparticle interactions". In: *Nano Today* 3.1-2 (2008), pp. 40–47.

[82] Jordi Piella, Neus G. Bastús, and Víctor Puntes. "Size-Dependent Protein-Nanoparticle Interactions in Citrate-Stabilized Gold Nanoparticles: The Emergence of the Protein Corona". In: *Bioconjugate chemistry* 28.1 (2017), pp. 88–97.

[83] Natalia Feiner-Gracia et al. "Super-Resolution Microscopy Unveils Dynamic Heterogeneities in Nanoparticle Protein Corona". In: *Small* 13.41 (2017), p. 1701631.

[84] Priya Prakash Karmali and Dmitri Simberg. "Interactions of nanoparticles with plasma proteins: implication on clearance and toxicity of drug delivery systems". In: *Expert Opinion on Drug Delivery* 8.3 (2011), pp. 343–357.

[85] A Gessner et al. "Nanoparticles with decreasing surface hydrophobicities: influence on plasma protein adsorption". In: *International Journal of Pharmaceutics* 196.2 (2000), pp. 245–249.

[86] D. Docter et al. "The nanoparticle biomolecule corona: lessons learned ? challenge accepted?" In: *Chem. Soc. Rev.* 44.17 (2015), pp. 6094–6121.

[87] T. M. Göppert and R. H. Müller. "Adsorption kinetics of plasma proteins on solid lipid nanoparticles for drug targeting". In: *International Journal of Pharmaceutics* 302.1-2 (2005), pp. 172–186.

[88] Ana Lilia Barrán-Berdón et al. "Time evolution of nanoparticle-protein corona in human plasma: Relevance for targeted drug delivery". In: *Langmuir* 29.21 (2013), pp. 6485–6494.

[89] Harald F. Krug. "Nanosafety Research?Are We on the Right Track?" In: *Angewandte Chemie International Edition* 53.46 (2014), pp. 12304–12319.

[90] Julian A. J. Jaros et al. "Affinity Depletion of Plasma and Serum for Mass Spectrometry-Based Proteome Analysis". In: Humana Press, Totowa, NJ, 2013, pp. 1–11.

[91] Bing C. Mei et al. "Effects of ligand coordination number and surface curvature on the stability of gold nanoparticles in aqueous solutions". In: *Langmuir* 25.18 (2009), pp. 10604–10611.

[92] Sarit S. Agasti et al. "Structural control of the monolayer stability of water-soluble gold nanoparticles". In: *J. Mater. Chem.* 18.1 (2008), pp. 70–73.

[93] Carl S. Weisbecker, Margaret V. Merritt, and George M. Whitesides. "Molecular Self-Assembly of Aliphatic Thiols on Gold Colloids". In: *Langmuir* 12.16 (1996), pp. 3763–3772.

[94] Cuicui Ge et al. "Towards understanding of nanoparticle–protein corona". In: *Archives of Toxicology* 89.4 (2015), pp. 519–539.

[95] Angelo Fontana et al. "Probing protein structure by limited proteolysis". In: *Acta Biochimica Polonica*. Vol. 51. 2. 2004, pp. 299–321.

[96] Min Hu et al. "Gold nanostructures: engineering their plasmonic properties for biomedical applications". In: *Chemical Society Reviews* 35.11 (2006), p. 1084.

[97] Daniel Huang et al. "Plastic-Compatible Low Resistance Printable Gold Nanoparticle Conductors for Flexible Electronics". In: *Journal of The Electrochemical Society* 150.7 (2003), G412.

[98] Tanya Stuchinskaya et al. "Targeted photodynamic therapy of breast cancer cells using antibody–phthalocyanine–gold nanoparticle conjugates". In: *Photochemical & Photobiological Sciences* 10.5 (2011), p. 822.

[99] Sarah D Brown et al. "Gold Nanoparticles for the Improved Anticancer Drug Delivery of the Active Component of Oxaliplatin". In: *Journal of the American Chemical Society* 132.13 (2010), pp. 4678–4684.

[100] M E Ali et al. "Gold nanoparticle sensor for the visual detection of pork adulteration in meatball formulation". In: *Journal of Nanomaterials* 2012 (2012).

[101] Steven D Perrault and Warren C W Chan. "In vivo assembly of nanoparticle components to improve targeted cancer imaging". In: *Proceedings of the National Academy of Sciences* 107.25 (2010), pp. 11194–11199.

[102] Gang Peng et al. "Diagnosing lung cancer in exhaled breath using gold nanoparticles". In: *Nature Nanotechnology* 4.10 (2009), pp. 669–673.

[103] David T. Thompson. "Using gold nanoparticles for catalysis". In: *Nano Today* 2.4 (2007), pp. 40–43.

[104] Nikolai Khlebtsov and Lev Dykman. "Biodistribution and toxicity of engineered gold nanoparticles: a review of in vitro and in vivo studies". In: *Chem. Soc. Rev.* 40.3 (2011), pp. 1647–1671.

[105] Tao Zhang et al. "A new strategy improves assembly efficiency of DNA mono-modified gold nanoparticles". In: *Chemical Communications* 47.20 (2011), p. 5774.

[106] Shutao Guo et al. "Enhanced gene delivery and siRNA silencing by gold nanoparticles coated with charge-reversal polyelectrolyte". In: *ACS Nano* 4.9 (2010), pp. 5505–5511.

[107] Sunho Park and Kimberly Hamad-Schifferli. "Enhancement of in vitro translation by gold nanoparticle-DNA conjugates". In: *ACS Nano* 4.5 (2010), pp. 2555–2560.

[108] Wolfgang Eck et al. “PEGylated gold nanoparticles conjugated to monoclonal F19 antibodies as targeted labeling agents for human pancreatic carcinoma tissue”. In: *ACS Nano* 2.11 (2008), pp. 2263–2272.

[109] Ivan H. El-Sayed, Xiaohua Huang, and Mostafa A. El-Sayed. “Surface plasmon resonance scattering and absorption of anti-EGFR antibody conjugated gold nanoparticles in cancer diagnostics: Applications in oral cancer”. In: *Nano Letters* 5.5 (2005), pp. 829–834.

[110] Luigi Calzolai et al. “Protein-nanoparticle interaction: Identification of the ubiquitin-gold nanoparticle interaction site”. In: *Nano Letters* 10.8 (2010), pp. 3101–3105.

[111] Marie Eve Aubin-Tam and Kimberly Hamad-Schifferli. “Gold nanoparticle-cytochrome c complexes: The effect of nanoparticle ligand charge on protein structure”. In: *Langmuir* 21.26 (2005), pp. 12080–12084.

[112] Daniel F. Moyano and Vincent M. Rotello. “Nano meets biology: Structure and function at the nanoparticle interface”. In: *Langmuir* 27.17 (2011), pp. 10376–10385.

[113] Prashant K. Jain et al. “Calculated absorption and scattering properties of gold nanoparticles of different size, shape, and composition: Applications in biological imaging and biomedicine”. In: *Journal of Physical Chemistry B* 110.14 (2006), pp. 7238–7248.

[114] Yi-Cheun Yeh, Brian Creran, and Vincent M. Rotello. “Gold nanoparticles: preparation, properties, and applications in bionanotechnology”. In: *Nanoscale* 4.6 (2012), pp. 1871–1880.

[115] S.H. Radwan and H.M.E. Azzazy. “Gold nanoparticles for molecular diagnostics”. In: *Expert Review of Molecular Diagnostics* 9.5 (2009), pp. 511–524.

[116] Pedro Baptista et al. “Gold nanoparticles for the development of clinical diagnosis methods”. In: *Analytical and Bioanalytical Chemistry* 391.3 (2008), pp. 943–950.

[117] K. H. Su et al. "Interparticle coupling effects on plasmon resonances of nanogold particles". In: *Nano Letters* 3.8 (2003), pp. 1087–1090. eprint: `1106.1690`.

[118] Neus G. Bastús, Joan Comenge, and Víctor Puntes. "Kinetically controlled seeded growth synthesis of citrate-stabilized gold nanoparticles of up to 200 nm: Size focusing versus ostwald ripening". In: *Langmuir* 27.17 (2011), pp. 11098–11105.

[119] John Turkevich, Peter Cooper Stevenson, and James Hillier. "A study of the nucleation and growth processes in the synthesis of colloidal gold". In: *Discuss. Faraday Soc.* 11 (0 1951), pp. 55–75.

[120] Vashti Irani et al. "Molecular properties of human IgG subclasses and their implications for designing therapeutic monoclonal antibodies against infectious diseases". In: *Molecular Immunology* 67.2, Part A (2015). Therapeutic Antibodies: Discovery, Design and Deployment, pp. 171 –182.

[121] Nikolaos Psychogios et al. "The Human Serum Metabolome". In: *PLOS ONE* 6.2 (2011), pp. 1–23.

[122] Pengxiang Zhao, Na Li, and Didier Astruc. "State of the art in gold nanoparticle synthesis". In: *Coordination Chemistry Reviews* 257.3 (2013), pp. 638 –665.

[123] Ahmet Bekdemir and Francesco Stellacci. "A centrifugation-based physicochemical characterization method for the interaction between proteins and nanoparticles". In: *Nature Communications* 7 (2016), p. 13121.

[124] Adam M. Davidson et al. "Sensitive Analysis of Protein Adsorption to Colloidal Gold by Differential Centrifugal Sedimentation". In: *Analytical Chemistry* 89.12 (2017), pp. 6807–6814.

[125] Carlheinz Röcker et al. "A quantitative fluorescence study of protein monolayer formation on colloidal nanoparticles". In: *Nature Nanotechnology* 4.9 (2009), pp. 577–580.

[126] Hannes Fischer, Igor Polikarpov, and Aldo F. Craievich. “Average protein density is a molecular-weight-dependent function”. In: *Protein Science* 13.10 (2009), pp. 2825–2828.

[127] “Protein size calculator”. In: (). URL: `http://www.calctool.org/CALC/prof/bio/protein_size`.

[128] Hans. Neurath. *The Proteins Composition, Structure, and Function. Volume III*. Elsevier Science, 1965, p. 601.

[129] U. K. LAEMMLI. “Cleavage of Structural Proteins during the Assembly of the Head of Bacteriophage T4”. In: *Nature* 227.5259 (1970), pp. 680–685.

[130] R. C. (Robert Carter) Allen and Bruce Budowle. *Gel electrophoresis of proteins and nucleic acids : selected techniques*. W. de Gruyter, 1994, p. 352.

[131] T Sorlie et al. “National Academy of Sciences | Proceedings of the National Academy of Sciences of the United States of America”. In: *Proc Natl Acad Sci USA* 98.19 (2001), pp. 10869–74.

[132] Tibor Sipos and Joseph R. Merkel. “An Effect of Calcium Ions on the Activity, Heat Stability, and Structure”. In: *Biochemistry* 9.14 (1970), pp. 2766–2775.

[133] Simon J Hubbard. “The structural aspects of limited proteolysis of native proteins”. In: *Biochimica et Biophysica Acta - Protein Structure and Molecular Enzymology* 1382.2 (1998), pp. 191–206.

[134] Angelo Fontana et al. “Probing the partly folded states of proteins by limited proteolysis”. In: *Folding and Design* 2.2 (1997), R17–R26.

[135] Sophie Quevillon-Cheruel et al. “Cloning, production, and purification of proteins for a medium-scale structural genomics project”. In: *Methods in molecular biology* 363 (2007), pp. 21–37.

[136] Tudor Moldoveanu et al. “Ca2+-induced structural changes in rat m-calpain revealed by partial proteolysis”. In: *Biochimica et Biophysica Acta - Protein Structure and Molecular Enzymology* 1545.1-2 (2001), pp. 245–254.

[137] Dengming Ming and Michael E. Wall. "Interactions in native binding sites cause a large change in protein dynamics". In: *Journal of Molecular Biology* 358.1 (2006), pp. 213–223.

[138] Martin Lundqvist et al. "Proteolytic cleavage reveals interaction patterns between silica nanoparticles and two variants of human carbonic anhydrase". In: *Langmuir* 21.25 (2005), pp. 11903–11906.

[139] Angelo Fontana et al. "Correlation between Sites of Limited Proteolysis and Segmental Mobility in Thermolysin". In: *Biochemistry* 25.8 (1986), pp. 1847–1851.

[140] Patrizia Polverino D E Laureto et al. "Limited proteolysis of bovine a-lactalbumin : Isolation and characterization of protein domains". In: *Protein Science* 8.11 (1999), pp. 2290–2303.

[141] Martin Lundqvist et al. "The evolution of the protein corona around nanoparticles: A test study". In: *ACS Nano* 5.9 (2011), pp. 7503–7509.

[142] Sylvia Kiese et al. "Shaken, not stirred: Mechanical stress testing of an IgG1 antibody". In: *Journal of Pharmaceutical Sciences* 97.10 (2008), pp. 4347–4366.

[143] Helena de Puig et al. "Effect of the Protein Corona on Antibody Antigen Binding in Nanoparticle Sandwich Immunoassays". In: *Bioconjugate Chemistry* 28.1 (2017), pp. 230–238.

[144] Maria Sánchez-Purrà et al. "Surface-Enhanced Raman Spectroscopy-Based Sandwich Immunoassays for Multiplexed Detection of Zika and Dengue Viral Biomarkers". In: *ACS Infectious Diseases* 3.10 (2017), pp. 767–776.

[145] Maria Sánchez-Purrà et al. "Design of SERS nanotags for multiplexed lateral flow immunoassays". In: *Mol. Syst. Des. Eng.* 2.4 (2017), pp. 401–409.

[146] Silvia Milani et al. "Reversible versus Irreversible Binding of Transferrin to Polystyrene Nanoparticles: Soft and Hard Corona". In: *ACS Nano* 3 (), pp. 2532–2541.

[147] Alexey A. Vertegel, Richard W. Siegel, and Jonathan S. Dordick. "Silica nanoparticle size influences the structure and enzymatic activity of adsorbed lysozyme". In: *Langmuir* 20.16 (2004), pp. 6800–6807.

[148] Siddhartha Shrivastava et al. "Position-Specific Chemical Modification and Quantitative Proteomics Disclose Protein Orientation Adsorbed on Silica Nanoparticles". In: *Nano Letters* 12.3 (2012), pp. 1583–1587.

[149] Francesca Pederzoli et al. "Protein corona and nanoparticles: how can we investigate on?" In: *Wiley Interdisciplinary Reviews: Nanomedicine and Nanobiotechnology* 9.6 (2017), p. 1467.

[150] Jennifer E Gagner et al. "Effect of gold nanoparticle structure on the conformation and function of adsorbed proteins." In: *Biomaterials* 33.33 (2012), pp. 8503–16.

[151] Ailin Wang et al. "Using Hydrogen/Deuterium Exchange to Monitor Protein Structure in the Presence of Gold Nanoparticles". In: *The Journal of Physical Chemistry B* 118.49 (2014), pp. 14148–14156.

[152] Shanghao Li, Zhili Peng, and Roger M Leblanc. "Method To Determine Protein Concentration in the Protein-Nanoparticle Conjugates Aqueous Solution Using Circular Dichroism Spectroscopy". In: *Analytical Chemistry* 87.13 (2015), pp. 6455–6459.

[153] Michael Assfalg et al. In: *Biochimica et Biophysica Acta BBA - Proteins and Proteomics* 1 (), pp. 102–114.

[154] Jos Buijs et al. "Localized changes in the structural stability of myoglobin upon adsorption onto silica particles, as studied with hydrogen/deuterium exchange mass spectrometry". In: *Journal of Colloid and Interface Science* 263.2 (2003), pp. 441–448.

[155] Christine Vauthier, Peter Lindner, and Bernard Cabane. "Configuration of bovine serum albumin adsorbed on polymer particles with grafted dextran corona". In: *Colloids and Surfaces B: Biointerfaces* 69.2 (2009), pp. 207–215.

[156] Helén Larsericsdotter, Sven Oscarsson, and Jos Buijs. “Structure, stability, and orientation of BSA adsorbed to silica”. In: *Journal of Colloid and Interface Science* 289.1 (2005), pp. 26–35.

[157] Jorge Escorihuela et al. “Dual-Polarization Interferometry: A Novel Technique To Light up the Nanomolecular World”. In: *Chemical Reviews* 115.1 (2014), pp. 265–294.

[158] Yanxiong Pan et al. “Probing the structural basis and adsorption mechanism of an enzyme on nano-sized protein carriers”. In: *Nanoscale* 9.10 (2017), pp. 3512–3523.

[159] Xiaoyu Wu and Ganesan Narsimhan. “Effect of surface concentration on secondary and tertiary conformational changes of lysozyme adsorbed on silica nanoparticles”. In: *Biochimica et Biophysica Acta ({BBA}) - Proteins and Proteomics* 1784.11 (2008), pp. 1694–1701.

[160] Necla Mine Eren, Ganesan Narsimhan, and Osvaldo H Campanella. “Protein adsorption induced bridging flocculation: the dominant entropic pathway for nano-bio complexation”. In: *Nanoscale* 8.6 (2016), pp. 3326–3336.

[161] Flora Felsovalyi et al. “Reversibility of the Adsorption of Lysozyme on Silica”. In: *Langmuir* 27.19 (2011), pp. 11873–11882.

[162] Candace C Fleischer and Christine K Payne. “Nanoparticle-Cell Interactions: Molecular Structure of the Protein Corona and Cellular Outcomes”. In: *Accounts of Chemical Research* 47.8 (2014), pp. 2651–2659.

[163] Nima Soltani and Mohammad Reza Gholami. “Increase in the β-Sheet Character of an Amyloidogenic Peptide upon Adsorption onto Gold and Silver Surfaces”. In: *ChemPhysChem* 18.5 (2017), pp. 526–536.

[164] Jie An Yang et al. “Study of Wild-Type α-Synuclein Binding and Orientation on Gold Nanoparticles”. In: *Langmuir* 29.14 (2013), pp. 4603–4615.

[165] Jie An Yang et al. "α-Synuclein's Adsorption, Conformation, and Orientation on Cationic Gold Nanoparticle Surfaces Seeds Global Conformation Change". In: *The Journal of Physical Chemistry B* 13 (), pp. 3559–3571.

[166] Robert Vacha, Sara Linse, and Mikael Lund. "Surface Effects on Aggregation Kinetics of Amyloidogenic Peptides". In: *Journal of the American Chemical Society* 136.33 (2014), pp. 11776–11782.

[167] Guangyan Qing et al. "Chiral Effect at Protein/Graphene Interface: A Bioinspired Perspective To Understand Amyloid Formation". In: *Journal of the American Chemical Society* 136.30 (2014), pp. 10736–10742.

[168] M. Ramazzotti et al. "Mechanisms for the inhibition of amyloid aggregation by small ligands". In: *Bioscience Reports* 36.5 (2016), p. 00385.

[169] Romana Parveen, Tooba Naz Shamsi, and Sadaf Fatima. "Nanoparticles-protein interaction: Role in protein aggregation and clinical implications". In: *International Journal of Biological Macromolecules* 94 (2017), pp. 386–395.

[170] Gaobo Yu and Jian Zhou. "Understanding the curvature effect of silica nanoparticles on lysozyme adsorption orientation and conformation: a mesoscopic coarse-grained simulation study". In: *Phys. Chem. Chem. Phys.* 18.34 (2016), pp. 23500–23507.

[171] Xiaotian Sun et al. "The Selective Interaction between Silica Nanoparticles and Enzymes from Molecular Dynamics Simulations". In: *PLoS ONE* 9.9 (2014). Ed. by Pratul K Agarwal, e107696.

[172] Thomas Benedict Bartnikas. "Known and potential roles of transferrin in iron biology". In: *BioMetals* 25.4 (2012), pp. 677–686.

[173] Gaye F White et al. "Multiphoton-excited luminescence of a lanthanide ion in a protein complex: Tb(3+) bound to transferrin." In: *Photochemical & photobiological sciences : Official journal of the European Photochemistry Association and the European Society for Photobiology* 3.1 (2004), pp. 47–55.

[174] Lin Wang, Wenjun Zhao, and Weihong Tan. "Bioconjugated silica nanoparticles: Development and applications". In: *Nano Research* 1.2 (2008), pp. 99–115.

[175] Sugam Kumar, Vinod K Aswal, and P Callow. "pH-Dependent Interaction and Resultant Structures of Silica Nanoparticles and Lysozyme Protein". In: *Langmuir* 30.6 (2014), pp. 1588–1598.

[176] Kurosch Rezwan, Lorenz P Meier, and Ludwig J Gauckler. "Lysozyme and bovine serum albumin adsorption on uncoated silica and AlOOH-coated silica particles: the influence of positively and negatively charged oxide surface coatings". In: *Biomaterials* 26.21 (2005), pp. 4351–4357.

[177] Werner Stober, Arthur Fink, and Ernst Bohn. "Controlled growth of monodisperse silica spheres in the micron size range". In: *Journal of Colloid and Interface Science* 26.1 (1968), pp. 62–69.

[178] Jean Christophe Rochet and Peter T. Lansbury. "Amyloid fibrillogenesis: Themes and variations". In: *Current Opinion in Structural Biology* 10.1 (2000), pp. 60–68.

[179] Jean D. Sipe and Alan S. Cohen. "Review: History of the Amyloid Fibril". In: *Journal of Structural Biology* 130.2-3 (2000), pp. 88–98.

[180] Roma N. Rambaran and Louise C. Serpell. "Amyloid fibrils". In: *Prion* 2.3 (2008), pp. 112–117.

[181] Joseph T. Jarrett and Peter T. Lansbury. "Seeding "one-dimensional crystallization" of amyloid: A pathogenic mechanism in Alzheimer's disease and scrapie?" In: *Cell* 73.6 (1993), pp. 1055–1058.

[182] James D. Harper and Peter T. Lansbury. "MODELS OF AMYLOID SEEDING IN ALZHEIMER'S DISEASE AND SCRAPIE:Mechanistic Truths and Physiological Consequences of the Time-Dependent Solubility of Amyloid Proteins". In: *Annual Review of Biochemistry* 66.1 (1997), pp. 385–407.

[183] Joseph T. Jarrett, Elizabeth P. Berger, and Peter T. Lansbury. "The Carboxy Terminus of the β Amyloid Protein Is Critical for the Seeding of Amyloid Formation: Implications for the Pathogenesis

of Alzheimer's Disease". In: *Biochemistry* 32.18 (1993), pp. 4693–4697.

[184] Hogyu Han, Paul H. Weinreb, and Peter T. Lansbury. "The core Alzheimer's peptide NAC forms amyloid fibrils which seed and are seeded by β-amyloid: is NAC a common trigger or target in neurodegenerative disease?" In: *Chemistry and Biology* 2.3 (1995), pp. 163–169.

[185] Songming Chen et al. "Amyloid-like features of polyglutamine aggregates and their assembly kinetics". In: *Biochemistry* 41.23 (2002), pp. 7391–7399.

[186] J. Hofrichter, P. D. Ross, and W. A. Eaton. "Kinetics and Mechanism of Deoxyhemoglobin S Gelation: A New Approach to Understanding Sickle Cell Disease". In: *Proceedings of the National Academy of Sciences* 71.12 (1974), pp. 4864–4868.

[187] Tudor Arvinte, Amelia Cudd, and Alex F. Drake. "Studies of human calcitonin secondary structure and of the fibrillation phenomena". In: *Peptides 1992*. Springer Netherlands, 1993, pp. 503–504.

[188] E. Scherzinger et al. "Self-assembly of polyglutamine-containing huntingtin fragments into amyloid-like fibrils: Implications for Huntington's disease pathology". In: *Proceedings of the National Academy of Sciences* 96.8 (1999), pp. 4604–4609.

[189] Liza Nielsen et al. "Effect of environmental factors on the kinetics of insulin fibril formation: Elucidation of the molecular mechanism". In: *Biochemistry* 40.20 (2001), pp. 6036–6046.

[190] N Ferguson et al. "Rapid amyloid fiber formation from the fast-folding WW domain FBP28". In: *Proceedings of the National Academy of Sciences of the United States of America* 100.17 (2003), pp. 9814–9819.

[191] Li Zhu et al. "Relationship between stability of folding intermediates and amyloid formation for the yeast prion Ure2p: A

quantitative analysis of the effects of pH and buffer system". In: *Journal of Molecular Biology* 328.1 (2003), pp. 235–254.

[192] Peter Hortschansky et al. "The aggregation kinetics of Alzheimer ′ s b-amyloid peptide is controlled by stochastic nucleation". In: *Protein Science* 14.7 (2005), pp. 1753–1759.

[193] Sathish Kumar and Jochen Walter. "Phosphorylation of amyloid beta (A?) peptides ? A trigger for formation of toxic aggregates in Alzheimer′s disease". In: *Aging* 3.8 (2011), pp. 803–812.

[194] Michel Goedert. "Alpha-synuclein and neurodegenerative diseases". In: *Nature Reviews Neuroscience* 2.7 (2001), pp. 492–501.

[195] Julie Lotharius and Patrik Brundin. "Pathogenesis of parkinson′s disease: Dopamine, vesicles and α-synuclein". In: *Nature Reviews Neuroscience* 3.12 (2002), pp. 932–942.

[196] John Q. Trojanowski and Virginia M.-Y. Lee. "Aggregation of Neurofilament and α-Synuclein Proteins in Lewy Bodies". In: *Archives of Neurology* 55.2 (1998), pp. 151–152.

[197] Christopher D. Syme et al. "A Raman optical activity study of rheomorphism in caseins, synucleins and tau: New insight into the structure and behaviour of natively unfolded proteins". In: *European Journal of Biochemistry* 269.1 (2002), pp. 148–156.

[198] David C. Thorn et al. "Amyloid Fibril Formation by Bovine Milk kappa-Casein and Its Inhibition by the Molecular Chaperones alphaS- and beta- Casein". In: *Biochemistry* 44.51 (2005), pp. 17027–17036.

[199] Matteo BARBERIS et al. "The yeast cyclin-dependent kinase inhibitor Sic1 and mammalian p27 Kip1 are functional homologues with a structurally conserved inhibitory domain". In: *Biochemical Journal* 387.3 (2005), pp. 639–647.

[200] Stefania Brocca et al. "Defining Structural Domains of an Intrinsically Disordered Protein: Sic1, the Cyclin-Dependent Kinase Inhibitor of Saccharomyces cerevisiae". In: *Molecular Biotechnology* 47.1 (2010), pp. 34–42.

[201] Stefania Brocca et al. “Compaction Properties of an Intrinsically Disordered Protein: Sic1 and Its Kinase-Inhibitor Domain”. In: *Biophysical Journal* 100.9 (2011), pp. 2243–2252.

[202] Ichiro Matsumura and Jack F. Kirsch. “Is aspartate 52 essential for catalysis by chicken egg white lysozyme? The role of natural substrate-assisted hydrolysis”. In: *Biochemistry* 35.6 (1996), pp. 1881–1889.

[203] Hassane S. Mchaourab et al. “Motion of spin-labeled side chains in T4 lysozyme. Correlation with protein structure and dynamics”. In: *Biochemistry* 35.24 (1996), pp. 7692–7704.

[204] Peter T. Gomme and Karl B. McCann. “Transferrin: Structure, function and potential therapeutic actions”. In: *Drug Discovery Today* 10.4 (2005), pp. 267–273.

[205] Konstantinos Gkouvatsos, George Papanikolaou, and Kostas Pantopoulos. *Regulation of iron transport and the role of transferrin*. 2012.

[206] M Hirose. “The structural mechanism for iron uptake and release by transferrins”. In: *Bioscience Biotechnology and Biochemistry* 64.7 (2000), pp. 1328–1336.

[207] Nazanin Abbaspour, Richard Hurrell, and Roya Kelishadi. *Review on iron and its importance for human health*. 2014.

[208] Minghuang Hong et al. “Efficient tumor targeting of hydroxycamptothecin loaded PEGylated niosomes modified with transferrin”. In: *Journal of Controlled Release* 133.2 (2009), pp. 96–102.

[209] Eugene Mahon, Delyan R. Hristov, and Kenneth A. Dawson. “Stabilising fluorescent silica nanoparticles against dissolution effects for biological studies”. In: *Chemical Communications* 48.64 (2012), p. 7970.

[210] Diane Latawiec et al. “Modulation of ?-Synuclein Aggregation by Dopamine Analogs”. In: *PLoS ONE* 5.2 (2010). Ed. by Mel B Feany, e9234.

[211] R C Davies, A Neuberger, and B M Wilson. "The dependence of lysozyme activity on pH and ionic strength". In: *Biochimica et Biophysica Acta BBA - Enzymology* 178.2 (1969), pp. 294–305.

[212] *ExPASy - ProtParam tool*. URL: `https://web.expasy.org/protparam/`.

[213] Christina R Bodner, Christopher M Dobson, and Ad Bax. "Multiple Tight Phospholipid-Binding Modes of α-Synuclein Revealed by Solution {NMR} Spectroscopy". In: *Journal of Molecular Biology* 390.4 (2009), pp. 775–790.

[214] Diletta Ami, Antonino Natalello, and Silvia Maria Doglia. "Fourier Transform Infrared Microspectroscopy of Complex Biological Systems: From Intact Cells to Whole Organisms". In: *Methods in Molecular Biology*. Humana Press, 2012, pp. 85–100.

[215] Olivia Cano-Garrido et al. "Functional protein-based nanomaterial produced in microorganisms recognized as safe: A new platform for biotechnology". In: *Acta Biomaterialia* 43 (2016), pp. 230–239.

[216] Antonino Natalello et al. "Compact conformations of α-synuclein induced by alcohols and copper". In: *Proteins: Structure, Function, and Bioinformatics* 79.2 (2010), pp. 611–621.

[217] Antonino Natalello, Diletta Ami, and Silvia Maria Doglia. "Fourier Transform Infrared Spectroscopy of Intrinsically Disordered Proteins: Measurement Procedures and Data Analyses". In: *Methods in Molecular Biology*. Humana Press, 2012, pp. 229–244.

[218] Amanda R Wilmsmeyer et al. "Infrared Spectra and Binding Energies of Chemical Warfare Nerve Agent Simulants on the Surface of Amorphous Silica". In: *The Journal of Physical Chemistry C* 117.30 (2013), pp. 15685–15697.

[219] Heino Susi and D.Michael Byler. "[13] Resolution-enhanced fourier transform infrared spectroscopy of enzymes". In: *Methods in Enzymology*. Elsevier, 1986, pp. 290–311.

[220] Peter Tompa. “Intrinsically unstructured proteins”. In: *Trends Biochem. Sci.* 27.10 (2002), pp. 527–533.

[221] A J Miles and B A Wallace. “Circular dichroism spectroscopy of membrane proteins”. In: *Chem. Soc. Rev.* 45.18 (2016), pp. 4859–4872.

[222] Mengmeng Wang et al. “Probing the mechanism of plasma protein adsorption on Au and Ag nanoparticles with {FT}-{IR} spectroscopy”. In: *Nanoscale* 7.37 (2015), pp. 15191–15196.

[223] Himadri S Mandal and Heinz-Bernhard Kraatz. “Effect of the Surface Curvature on the Secondary Structure of Peptides Adsorbed on Nanoparticles”. In: *Journal of the American Chemical Society* 129.20 (2007), pp. 6356–6357.

[224] Juan C Cruz et al. “Conformational changes and catalytic competency of hydrolases adsorbing on fumed silica nanoparticles: {II}. Secondary structure”. In: *Colloids and Surfaces B: Biointerfaces* 81.1 (2010), pp. 1–10.

[225] Andreas Barth. “Infrared spectroscopy of proteins”. In: *Biochimica et Biophysica Acta ({BBA}) - Bioenergetics* 1767.9 (2007), pp. 1073–1101.

[226] C Bustamante, I Tinoco, and M F Maestre. “Circular differential scattering can be an important part of the circular dichroism of macromolecules.” In: *Proceedings of the National Academy of Sciences* 80.12 (1983), pp. 3568–3572.

[227] Ángela I López-Lorente and Boris Mizaikoff. “Recent advances on the characterization of nanoparticles using infrared spectroscopy”. In: *{TrAC} Trends in Analytical Chemistry* 84 (2016), pp. 97–106.

[228] Marco van de Weert et al. “Fourier Transform Infrared Spectrometric Analysis of Protein Conformation: Effect of Sampling Method and Stress Factors”. In: *Analytical Biochemistry* 297.2 (2001), pp. 160–169.

[229] Michael Jackson and Henry H Mantsch. "Beware of proteins in {DMSO}". In: *Biochimica et Biophysica Acta ({BBA}) - Protein Structure and Molecular Enzymology* 1078.2 (1991), pp. 231–235.

[230] S T R Walsh. "The hydration of amides in helices a comprehensive picture from molecular dynamics, IR, and NMR". In: *Protein Science* 12.3 (2003), pp. 520–531.

[231] Yanina D Alvarez et al. "Influence of Gold Nanoparticles on the Kinetics of α-Synuclein Aggregation". In: *Nano Letters* 13.12 (2013), pp. 6156–6163.

[232] Hongjun Xie and Jie Wu. "Silica nanoparticles induce α-synuclein induction and aggregation in {PC}12-cells". In: *Chemico-Biological Interactions* 258 (2016), pp. 197–204.

[233] Jie Wu and Hongjun Xie. "Effects of titanium dioxide nanoparticles on α-synuclein aggregation and the ubiquitin-proteasome system in dopaminergic neurons". In: *Artificial Cells, Nanomedicine, and Biotechnology* 44.2 (2014), pp. 690–694.

[234] Katarzyna Milowska, Marta Malachowska, and Teresa Gabryelak. "PAMAM G4 dendrimers affect the aggregation of α-synuclein". In: *International Journal of Biological Macromolecules* 48.5 (2011), pp. 742–746.

[235] Agata Rekas et al. "PAMAM Dendrimers as Potential Agents against Fibrillation of α-Synuclein, a Parkinson's Disease-Related Protein". In: *Macromolecular Bioscience* 3 (), pp. 230–238.

[236] Rizwan Khan et al. "Nanoparticles in relation to peptide and protein aggregation". In: *International Journal of Nanomedicine* (2014), p. 899.